

Miocene core complex development and coeval supradetachment basin evolution of  
Paros, Greece

by

Evan Anthony Bargnesi  
B.S., Union College, 2007

Submitted to the Department of Geology and the  
Faculty of the Graduate School of the University of  
Kansas in partial fulfillment of the requirements for the  
Degree of Master of Science

---

Dr. Daniel F. Stockli (Chairman)

---

Dr. Andreas Moeller

---

Dr. George Tsoflias

Date Defended: May 2, 2011

The Thesis Committee for Evan Bargnesi certifies  
that this is the approved version of the following thesis:

Miocene core complex development and coeval supradetachment basin evolution of  
Paros, Greece

Advisory Committee:

---

Dr. Daniel F. Stockli (Chairman)

---

Dr. Andreas Moeller

---

Dr. George Tsoflias

Date Approved: \_\_\_\_\_



## **ABSTRACT**

Miocene core complex development and coeval supradetachment basin evolution of Paros, Greece

By

Evan A. Bargnesi  
Department of Geology, May 2011  
University of Kansas

This study evaluates the tectonosedimentary evolution of Paros, Greece using apatite and zircon (U-Th)/He dating to assess the currently accepted kinematic history and resolve controversy about the formation of and sources to the Paros supradetachment basin. Overdispersed and improbable results in the footwall suite of zircons are examined using laser ablation depth-profiling to address the inherent assumption of homogeneous parent nuclide distribution in the zircon (U-Th)/He technique. Results from footwall zircon (U-Th)/He analyses indicate rapid cooling  $\geq 100^{\circ}\text{C}/\text{km}$  from 11 – 7 Ma, which confirms rapid core complex exhumation along the Naxos-Paros low-angle extensional detachment. The suite of detrital zircons preserves the multi-stage Mesozoic-Cenozoic tectonometamorphic history of the central Aegean Sea and was deposited synchronously with progressive core complex development. Laser ablation data suggest that parent nuclide zonation in zircon poses a significant challenge to the reliability of (U-Th)/He dating which can be corrected by forward modeling unique alpha-ejection corrections.

## **ACKNOWLEDGEMENTS**

Funding for this project was provided by laboratory funds from Dr. Daniel Stockli. Additional funding was provided through a GSA student research grant, an AAPG grant-in-aid of student research, a Sigma Xi student award, and University of Kansas Department of Geology graduate summer research support.

Without the help of Edgardo Josué Pujols-Vasquez, Laura Alford, Konstantinos Soukis and Kyle Gorynski, this work would not be possible. They have kept me on track during my years here. These are the people who have caught me when I stumbled and I hope that someday I may return the favor. I must also mention John Garver, Roman Kislitsyn, Doug Walker and Bad'r Ghorbal, who have patiently assisted and educated me in many respects. I surely would have struggled without their help. Neil Mancktelow, Konstantinos Soukis and Joe Miller gave tremendous effort during field work. I also appreciate useful discussions and help in the laboratory from Andreas Moeller, Eugene Szymanski, Chris Hager, Travis Glauser, Jordan-Leigh Taylor and Josh Burrus. Tandis Bidgoli and Sarah Evans also provided assistance in the lab.

I would also like to acknowledge those who have helped me along the way. Heather Shinogle assisted with SEM-CL imagery. Wayne Dickerson created thin sections used in this study. Andreas Moeller and Jeff Oalman provided help collecting U-Pb data. Ian Rowell assisted with running machines and poster printing. Paula Conlin, Gwethalyn Williams, Jenna Coker and Yolanda Davis created a backbone which sustains the department – thank you for all your help and patience.

I thank my committee members and co-authors for their time and support. My thoughts go out to Andreas Moeller, you have endured unimaginable hardship and I respect your strength and endurance. I also appreciate the constructive reviews and discussion from Konstantinos Soukis, Neil Mancktelow, Chris Hager and Jeremy Hourigan. Finally, I thank my advisor and committee chairman, Dan Stockli, for tolerating me and guiding me toward my degree. I will not soon forget my experience here in Kansas. Best of luck in Austin and perhaps our paths will cross again.

<b>TABLE OF CONTENTS</b>	<b>PAGE</b>
<b>TITLE AND SIGNATURE PAGE</b>	<b>ii</b>
<b>ABSTRACT</b>	<b>iii</b>
<b>ACKNOWLEDGEMENTS</b>	<b>iv</b>
<b>TABLE OF CONTENTS</b>	<b>vi</b>
<b>LIST OF TABLES AND FIGURES</b>	<b>ix</b>
<b>CHAPTER 1: INTRODUCTION</b>	<b>12</b>
<b>CHAPTER 1: REFERENCES</b>	<b>16</b>
<b>CHAPTER 2: Miocene Core Complex Development and Coeval Supradetachment Basin Evolution of Paros, Greece</b>	<b>18</b>
<b>ABSTRACT</b>	<b>18</b>
<b>INTRODUCTION</b>	<b>19</b>
<b>TECTONIC EVOLUTION AND CENOZOIC KINEMATICS IN THE CENTRAL AEGEAN REGION</b>	<b>21</b>
<b>GEOLOGY OF PAROS</b>	<b>26</b>
<b>METHODS</b>	<b>28</b>
<i>Apatite and Zircon (U-Th)/He Analysis</i>	<b>28</b>
<b>RESULTS</b>	<b>30</b>
<i>Paros Footwall Structure</i>	<b>30</b>
<i>Paros Footwall Geo- and Thermochronometry</i>	<b>32</b>
<i>Hanging Wall Sedimentology, Stratigraphy and Thermochronometry</i>	<b>33</b>

<b>DISCUSSION</b>	<b>38</b>
<i>Miocene Development of the Paros Metamorphic Core Complex</i>	38
<i>Supradetachment Basin Evolution at Molos and Alyki Bay</i>	43
<i>Stratigraphic Correlations in the Paros Supradetachment Basin</i>	49
<b>CONCLUSIONS</b>	<b>52</b>
<b>CHAPTER 2: REFERENCES</b>	<b>55</b>
<b>APPENDIX A: KU-IGL U-Pb Data</b>	<b>121</b>
<b>CHAPTER 3: Improved accuracy of zircon (U-Th)/He ages by rectifying parent nuclide zonation with practical methods</b>	<b>127</b>
<b>ABSTRACT</b>	<b>127</b>
<b>INTRODUCTION</b>	<b>128</b>
<b>THE ALPHA-EJECTION CORRECTION</b>	<b>130</b>
<b>PROCEDURES AND METHODS</b>	<b>133</b>
<i>Cathodoluminescence imaging of apatite and zircon</i>	133
<i>Mechanical abrasion of zircon</i>	133
<i>Laser ablation depth-profiling</i>	134
<i>Unique alpha-ejection corrections</i>	135
<b>RESULTS</b>	<b>137</b>
<i>SEM-CL analyses</i>	137
<i>Abraded zircon (U-Th)/He analyses</i>	138
<i>LA-ICP-MS depth-profiled (U-Th)/He analyses</i>	139
<b>DISCUSSION</b>	<b>142</b>

<i>Grain morphology and parent nuclide distribution</i>	<i>142</i>
<i>Mechanically abraded zircon (U-Th)/He data</i>	<i>143</i>
<i>Depth-profile controlled alpha-ejection corrections</i>	<i>144</i>
<b>CONCLUSIONS</b>	<b>146</b>
<b>CHAPTER 3: REFERENCES CITED</b>	<b>149</b>

## **LIST OF TABLES AND FIGURES**

### **PAGE**

### **CHAPTER 2: FIGURES**

Figure 1. Simplified regional structure map of the greater Aegean region	67
Figure 2. Simplified geologic map of Paros	69
Figure 3. Generalized thermal history of Paros	71
Figure 4. Results from structural characterization of the Paros footwall	73
Figure 5. (U-Th)/He results from footwall orthogneisses and igneous intrusives	75
Figure 6. Stratigraphic analysis of the Molos Bay sedimentary section	77
Figure 7. Stratigraphic analysis of the Alyki Bay sedimentary section	79
Figure 8. Stratigraphic analysis of the Santa Maria sedimentary section	81
Figure 9. Stacked probability density plots showing (U-Th)/He results	83
Figure 10. Results of detrital thermochronometry at Molos and Alyki Bay	85
Figure 11. Stratigraphic correlation for sedimentary outcrops on Paros	87
Figure 12. Tectonosedimentary evolution of the Paros supradetachment basin	89
Figure 13. Current structural configuration of Paros and Naxos	91

### **CHAPTER 2: TABLES**

Table 1. Footwall zircon U-Pb data	93
Table 2. Footwall zircon (U-Th)/He data	97
Table 3. Footwall apatite (U-Th)/He data	104
Table 4. Hanging wall zircon (U-Th)/He data	107
Table 5. Hanging wall apatite (U-Th)/He data	117

### **CHAPTER 3: FIGURES**

Figure 1. Comparison of age bias with rim position and concentration	154
Figure 2. Simplified regional tectonic map for the greater Aegean region	156
Figure 3. Age inverted results from (U-Th)/He analyses of the Paros footwall	158
Figure 4. Possible parent nuclide zonation scenarios	160
Figure 5. SEM-CL imagery from sample 08PA01	162
Figure 6. SEM-CL imagery from sample 08PA71	164
Figure 7. Schematic diagram of a stainless steel air abrasion vessel	166
Figure 8. Progressive U, Th, and He abrasion and effect on (U-Th)/He age	168
Figure 9. Photographic abrasion history of 08PA01	170
Figure 10. Results of mechanically abraded zircon (U-Th)/He ages	172
Figure 11. Analysis of aliquot 08PA01-13	174
Figure 12. Analysis of aliquot 08PA71-16	176
Figure 13. Analysis of aliquot 08PA71-20	178
Figure 14. Results of uniquely corrected (U-Th)/He ages for 08PA01	180
Figure 15. Results of uniquely corrected (U-Th)/He ages for 08PA71	182
Figure 16. Potential complications of LA-ICP-MS depth-profiling	184

### **CHAPTER 3: TABLES**

Table 1. Results from mechanically abraded zircon (U-Th)/He ages	186
Table 2. Results from unique alpha-ejection corrected (U-Th)/He ages	188
Table 3. Results from varying model parameters for sample 08PA01	191



Page intentionally left blank

## CHAPTER 1: INTRODUCTION

The research presented herein critically evaluates the development of the Paros metamorphic core complex coeval with supradetachment basin evolution using detrital and bedrock (U-Th)/He thermochronometry (Chapter 2) and develops a methodology for correcting inverted apatite and zircon (U-Th)/He ages observed in bedrock suites of the Paros footwall (Chapter 3). The primary funding for this project was provided by Dr. Daniel F. Stockli; additional funding was obtained by GSA, AAPG, and Sigma Xi grants-in-aid of student research (to Bargnesi) as well as University of Kansas Department of Geology graduate summer support (to Bargnesi).

Early work on the island of Paros identified the juxtaposition of sedimentary rocks against high-grade metamorphic rocks (Papanikolaou, 1977; Papanikolaou, 1980). It was soon after realized that the island hosts a cordilleran-type metamorphic core complex (Lister et al., 1984). Subsequent study has yielded the crystallization age of the footwall rocks (Engel and Reischmann, 1998), slip rates along the low-angle, extensional detachment fault (Brichau et al., 2006), detrital ages of the hanging wall rocks (Sanchez-Gomez et al., 2002) and new lithologic and structural mapping (Papp, 2007). This study builds on the foundation laid by these authors and contributes to the growing body of science on understanding extensional tectonics in the Aegean Sea, Greece.

The second chapter of this thesis is entitled *Miocene core complex development coeval with supradetachment basin evolution of Paros, Greece*. Detrital thermochronometric studies attempt to reconstruct local and regional structural and

tectonic histories by utilizing thermal signatures from sedimentary rocks (Bernet and Spiegel, 2004 and references therein). These types of studies are most effective in well-exposed basins with dominantly clastic input, which increases the abundance of useful mineral phases, such as apatite and zircon. The Aegean region is not an ideal location to perform such studies since sedimentary rocks outcrop sparsely and much of the sedimentary record is submerged. The island of Paros, Greece exposes a nearly complete syn-extensional, clastic sedimentary section and is thus suited to perform a detrital analysis to evaluate local and regional kinematics. We have measured this section in detail and taken systematic bedding measurements and clast counts together with short sampling intervals for (U-Th)/He analyses. Extensive regional sampling of exposed bedrock for (U-Th)/He and U-Pb analyses allows characterization of a potential sedimentary source and reveals the background thermal signature of the last major tectonometamorphic episode. This chapter is a journal manuscript that will be submitted to a special volume of *Tectonophysics* and the co-authors are Dr. Daniel F. Stockli, Dr. Neil Mancktelow, and Dr. Konstantinos Soukis.

The third and final chapter of this thesis, entitled *Improved accuracy of zircon (U-Th)/He ages by rectifying parent nuclide zonation with practical methods* examines the relationship between age inversion and parent nuclide zonation in zircon. Well-behaved mineral phases in a given rock should exhibit an age relationship in which apatite (U-Th)/He ages are younger than zircon (U-Th)/He ages based on the nominal closure temperature of each thermochronometer (~70°C in apatite from Wolf et al., 1996 and ~180°C in zircon from Reiners, 2005). The

amphibolite-facies rocks associated with the Paros metamorphic core complex demonstrate the inverse case, where apatite (U-Th)/He ages are older than zircon (U-Th)/He ages. This study explores novel approaches to correct this age inversion and restore proper age relationships in given samples which illustrate the problem. Cathodoluminescence scanning electron microscopy (SEM-CL) imagery reveals potential issues in zircon grains related to parent nuclide zonation. Zonation affects the alpha-ejection correction, which directly affects the final (U-Th)/He age (Hourigan et al., 2005). Mechanical air abrasion of zircon removes areas of parent nuclide inhomogeneity (Krogh, 1982), while laser-ablation inductively coupled mass spectrometry (LA-ICP-MS) depth-profiling allows for direct modification of the alpha-ejection correction by modeling the measured one-dimensional concentration array as three-dimensional (Hourigan et al., 2005). This chapter is a journal manuscript that will be submitted to *Chemical Geology* and the co-authors are Dr. Daniel F. Stockli and Dr. Jeremy Hourigan.

All apatite and zircon (U-Th)/He analyses were performed at the University of Kansas Isotope Geochemistry Laboratory (KU-IGL). All zircon abrasion was conducted at KU-IGL. Thermal and alpha-ejection modeling code was performed using HeMP (Hager and Stockli, 2009). Samples from Paros, Antiparos and Naxos were collected over two field seasons to the Aegean region (2008, 2009) by Bargnesi, Stockli, Mancktelow and Soukis. Stratigraphic section was measured and bedrock geology was characterized over the same time period by Bargnesi. Several LA-ICP-MS U-Pb analyses were performed at University of Arizona and KU-IGL.

SEM-CL imagery was obtained using a LEO Field scanning electron microscope at the University of Kansas Microscopy and Imaging Laboratory. U-Th-Pb depth-profiling was conducted at the University of California Santa Cruz by Bargnesi and Hourigan.

## CHAPTER 1: REFERENCES

- Bernet, M., Spiegel, C., 2004. Introduction: Detrital Thermochronology, in: Bernet, M., Spiegel, C. (Eds.), Detrital Thermochronology – Provenance analysis, exhumation, and landscape evolution of mountain belts. Geological Society of America Special Paper. 378, 1–6.
- Brichau, S., Ring, U., Ketcham, R.A., Carter, A., Stockli, D., Brunel, M., 2006. Constraining the long-term evolution of the slip rate for a major extensional fault system in the central Aegean, Greece, using thermochronology. Earth and Planetary Science Letters. 241, 293–306.
- Engel, M., Reischmann, T., 1998. Single zircon geochronology of orthogneisses from Paros, Greece. Bulletin of the Geological Society of Greece. 32, 91–99.
- Hager, C., Stockli, D.F., 2009. A new Matlab©-based Helium Modeling Package (“HeMP”) for thermal history recovery from single and multi-thermochronometer (U–Th)/He data and data arrays. Geological Society of America Abstracts with Programs. 41, 487.
- Hourigan, J.K., Reiners, P.W., Brandon, M.T., 2005. U-Th zonation-dependent alpha-ejection in (U–Th)/He chronometry. Geochimica et Cosmochimica Acta. 69, 3349–3365.
- Krogh, T.E., 1982. Improved accuracy of U–Pb zircon ages by the creation of more concordant systems using an air abrasion technique. Geochimica et Cosmochimica Acta. 46, 637–649.

- Lister, G.S., Banga, G., Feenstra, A., 1984. Metamorphic core complexes of Cordilleran type in the Cyclades, Aegean Sea, Greece. *Geology*. 12, 221–225.
- Papanikolaou, D., 1977. On the Structural Geology and Tectonics of Paros Island, Aegean Sea: *Annales Géologiques Des Pays Helléniques*. 28, 450–464.
- Papanikolaou, D., 1980. Contribution of the geology of the Aegean Sea: The Island of Paros: *Annales Géologiques Des Pays Helléniques*. 29, 477–533.
- Papp, M., 2007. Geology and kinematics of detachment faulting on NE Paros, Greece. Unpublished diploma thesis. ETH Zurich.
- Reiners, P.W., 2005. Zircon (U-Th)/He Thermochronometry, in: Reiners, P.W., Ehlers, T.A. (Eds.), *Low-Temperature Thermochronology: Techniques, Interpretations, and Applications. Reviews in Mineralogy and Geochemistry*, 58, 441–448.
- Sanchez-Gomez, M., Avigad, D., Heimann, A., 2002. Geochronology of clasts in allochthonous Miocene sedimentary sequence on Mykonos and Paros Islands: implications for backarc extension in the Aegean Sea. *Journal of the Geological Society London*. 159, 45–60.
- Wolf, R.A., Farley, K.A., Silver, L.T., 1996. Helium diffusion and low temperature thermochronometry of apatite. *Geochimica et Cosmochimica Acta*. 60, 4231–4240.

## **CHAPTER 2: Miocene Core Complex Development and Coeval Supradetachment Basin Evolution of Paros, Greece**

### **ABSTRACT**

The Aegean Sea hosts an extensional detachment system that has accommodated crustal-scale backarc extension due to the collapsing Alpine orogen and rollback of the subducting African slab beneath the Eurasian plate. Extension has reorganized the Alpine nappe pile and exhumed Cordilleran-type metamorphic core complexes via low-angle normal faulting. This study refines the tectonic and kinematic history of the Aegean Sea and presents new geo- and thermochronometric data from both lower-plate metamorphic rocks and upper-plate sedimentary rocks. On the island of Paros, Greece high-grade metamorphic rocks of the lower-plate are juxtaposed against an unmetamorphosed sedimentary stack of the upper-plate by a low-angle extensional detachment fault. Sedimentary rocks outcrop sparsely in the Aegean Sea as a result of heavy cultivation and tectonic burial, yet Paros exposes a nearly complete succession. The sedimentary rocks of Paros can be subdivided into three units: a lower marine unit, an upper fanglomerate unit, and recent cover closely allied with the locally exposed lower-plate. The lower marine unit unconformably overlies the detachment and yields detrital apatite (U-Th)/He (DAHe) ages from 7 - 13 Ma, while detrital zircon (U-Th)/He (DZHe) ages range from 8 to 121 Ma. The overlying fanglomerate DAHe ages are uniformly reset to ages that range from 7 – 10 Ma. Fanglomerate DZHe data have a primary thermal signature of 7 – 12 Ma, but produce ages up to 113 Ma. The DAHe and DZHe ages from the stratigraphically highest units are almost completely reset to ages that range from 8 – 15 Ma. These



detrital signatures are correlative to the major regional tectonometamorphic events in the Aegean Region: [1] Cretaceous Pelagonian-type metamorphism; [2] Eocene peak HP metamorphism; and [3] Miocene Barrovian overprinting of these earlier events. The reset DAHe signals throughout the succession indicate early exposure of rapidly exhumed footwall rocks. Unreset DZHe ages exhibit thermal signatures attributable to all three major Mesozoic-Tertiary tectonic events, indicating long-term upper-plate recycling followed by syn-extensional deposition. Detrital thermochronometric data indicate a classic unroofing sequence deposited in a supradetachment basin related to progressive core complex exhumation during the Middle to Late Miocene.

## **INTRODUCTION**

Extensional tectonic settings are manifested by two primary structural styles: 1) high-angle normal fault bound, half-graben block rifting (e.g., the Red Sea); and 2) low-angle normal fault bound core complex-style exhumation (e.g., Basin and Range). Both styles of extension are well-studied and well-understood in many respects. Low-temperature thermochronometry can be a useful tool for quantifying the timing and magnitude of normal faulting in these respective regimes by measuring the time of cooling during the extension and, progressive exhumation of, the continental lithosphere (Stockli, 2005 and references therein). Data suites from bedrock can also provide insight into the duration and rates of local and regional tectonometamorphic events during crustal-scale extension if fault geometries are constrained, while detrital suites may reveal the syn- and pre-extensional history.

Sedimentation in extensional regimes is recorded in basinal deposits created by differential uplift and erosion syn- and post-extension. The deposits record the tectonic and erosional history of extensional terranes and can possess a multitude of architectures and depositional styles, often controlled locally by far-field tectonic forces. Rapid sedimentation associated with lithospheric rifting typically creates thick sedimentary packages in half-graben basins bounded by high-angle normal faults (e.g., Gawthorpe and Leeder, 2000), while sedimentation associated with metamorphic core complex (MCC) development typically occurs in supradetachment basins (e.g., Friedmann and Burbank, 1995), which host thin sedimentary sections bounded by the low-angle normal fault that exhumed the high-grade rocks from relatively deep structural levels. Supradetachment basins are characterized by the resulting juxtaposition of high-grade metamorphic rocks associated with the core complex against weakly to unmetamorphosed sedimentary rocks allied with the eroded overburden.

Low- to mid-temperature thermochronology is a proven tool for constraining thermal histories in extensional tectonic settings (summary in Stockli, 2005) and to reconstruct detrital source thermal histories (e.g., Bernet and Spiegel, 2004; Carrapa et al., 2004; Harrison et al., 2005; Reiners, 2005). This study utilizes thermochronometry of the rocks of Paros, Greece to thermally and temporally characterize the development of the Paros metamorphic core complex and resultant sedimentation of the corresponding supradetachment basin. Specifically, we use apatite and zircon (U-Th)/He thermochronometers (AHe and ZHe, respectively) to

determine the thermal history of both lower-plate metamorphic rocks and the preserved upper-plate sedimentary strata exposed in northeast Paros. We then attempt to correlate the sedimentary units of Paros in a tectonostratigraphic context.

The central Aegean Sea is a commonly chosen area to study extensional and contractional tectonics (Dewey and Sengor, 1979; Lister et al., 1984; Taymaz et al., 1991; Jackson, 1994; Jolivet and Brun, 2010 and references therein) and is thus well understood in many respects. The island of Paros has been the focus of geologic studies on structure (Papanikolaou 1977, 1980; Robert, 1982; Gautier et al., 1993), biostratigraphy (Papageorgakis 1968a, 1968b; Dermitzakis and Papanikolaou, 1980; Böger, 1983) and geo- and thermochronology (Altherr et al., 1982; Engel and Reischmann, 1998; Sanchez-Gomez et al., 2002; Hejl et al., 2003; Brichau et al., 2006) which have provided a foundation on which to build this work. With AHe and ZHe analyses of both detrital and bedrock sample suites, we seek to create a dataset capable of resolving controversy associated with the origin of the Paros supradetachment basin and the source of the sediments therein and to assess the preexisting regional tectonometamorphic framework of the central Aegean region, which is largely based on the aforementioned biostratigraphy and thermochronometry.

## **TECTONIC EVOLUTION AND CENOZOIC KINEMATICS IN THE CENTRAL AEGEAN REGION**

Following the Late Paleozoic collapse of the Variscan orogeny, the central Aegean has experienced nearly continuous deformation in a variety of strain regimes.

During the Early Mesozoic, the Paleotethys Ocean closed, triggering sedimentation in the deep marine Pindos basin (Katzir et al., 2007; Papanikolaou, 2009) and depositing the shallow marine volcanosedimentary protoliths to the Cycladic Blueschist Unit (CBU) (Dürr et al., 1978). During the early Tertiary, Alpine contractional deformation obducted Pindos-derived ophiolites onto the Pelagonian passive margin (Katzir et al., 2007) and subsequently affected regional high-pressure metamorphism by subducting volcanoclastic sediments along the downgoing African Slab. Tertiary development and southward retreat of the Hellenic subduction zone (Royden, 1993; Brun and Faccenna, 2008), along with the collapse of the Alpine Orogeny, resulted in back-arc extension (e.g., Papanikolaou, 1993; Jolivet and Brun, 2010). Extensional deformation reworked the Alpine nappe stack and overprinted earlier metamorphic signatures of the basement gneisses and the CBU during exhumation of lower crustal metamorphic core complexes (e.g., Lister et al., 1984). Extension was also accompanied by widespread plutonism and volcanic activity, which followed the migrating arc southward (Papanikolaou, 1993; Pe-Piper and Piper, 2002).

The current configuration of tectonostratigraphic units in the central Aegean has been largely controlled by extensional reorganization of the Early Tertiary Alpine nappe pile. The basement rocks are Variscan gneisses and schists with variable degrees of deformation, intruded by abundant Miocene plutons and exposed on several islands as metamorphic core complexes (e.g., Paros, Naxos) (Dürr et al., 1978; Altherr et al., 1982; Lister et al., 1984; Papanikolaou, 1989; Gautier et al., 1999). Basement rocks are overlain by the Cycladic Blueschist Unit (CBU),

comprising metamorphosed Mesozoic shelf sequences intercalated with metavolcanic rocks (Dürr et al., 1978). The CBU experienced at least two distinct metamorphic episodes during the Late Mesozoic – Tertiary including HP deformation during the Late Cretaceous – Early Tertiary (Bröcker and Enders, 1999; Tomaschek et al., 2003; Putlitz et al., 2005; Bröcker and Keasling, 2006) and greenschist to amphibolite facies extensional overprinting in the Miocene (e.g., Brichau et al., 2006; Ring et al., 2010). The CBU is locally overlain by compositionally variable HP schists and HT granites of the Pelagonian Units, as well as ophiolitic rocks of the Pindos Units (Avigad and Garfunkel, 1991; Papanikolaou, 2009). In the central Aegean, these tectonometamorphic units are often exposed as heavily denuded footwall rocks in extensional fault systems and are tectonically juxtaposed against unmetamorphosed sedimentary rocks of the corresponding hanging walls which may be of pre- or syn-extensional origin.

The late Paleozoic to Mesozoic tectonic history of the central Aegean region is the subject of some debate. Zircon U-Pb dating of ortho- and paragneissic basement rocks on Paros (Altherr et al., 1982; Robert, 1982) produces igneous crystallization ages that are typically 300 – 315 Ma (Engel and Reischmann, 1998; this study) (Table 1), which suggests synchronous magmatism and metamorphism. The Permian and Triassic epochs were characterized by passive-margin shelf sedimentation in a shallow to deep ocean basin; Triassic algae have been recovered from marbles on Naxos (Negris, 1915-1919; Dürr et al., 1978). Widespread rifting is recorded by Triassic zircon U-Pb ages from volcanic sequences on the islands of Andros, Sifnos

and Ios (Bröcker and Pidgeon, 2007) and Triassic zircon U-Pb ages on gneissic clasts (Bröcker and Keasling, 2006). Some Jurassic magmatic activity is also recorded from zircon U-Pb ages on *mélange* blocks from Andros (Bröcker and Pidgeon, 2007). Cretaceous limestone outcrops on Paros (Papageorgakis 1968a; Papanikolaou, 1977; Papanikolaou, 1980; Dermitzakis and Papanikolaou, 1980) and similar aged clasts on Naxos (Jansen, 1977; Kuhleemann et al., 2004) indicate widespread carbonate sedimentation occurred during this time, although only tectonic slivers without meaningful stratigraphic context are exposed on Paros. Late Cretaceous – Early Paleocene zircon U-Pb ages from eclogite-facies rocks indicate either that African slab subduction may have initiated much earlier than the Eocene (Bröcker and Enders, 1999; Bröcker and Keasling, 2006) or the protolith emplacement ages for Eocene HP rocks (Keay, 1998; Tomaschek et al., 2003). Similarly, muscovite  $^{40}\text{Ar}/^{39}\text{Ar}$  ages from deformational structures in the Pelagonian Zone of the NW Aegean (mainland Greece) indicate Late Cretaceous metamorphism from 85 – 100 Ma (Lips et al., 1998). Some authors believe that African slab subduction began in the Late Cretaceous (Ring and Layer, 2003; Jolivet and Brun, 2010) or Early Paleocene (Ring et al., 2010) and has probably remained continuous since.

The commonly accepted age of peak HP metamorphism in the central Aegean is Middle Eocene (Wijbrans and McDougall, 1986; Bröcker and Enders, 1999; Tomaschek et al., 2003; Putlitz et al., 2005) although some authors distinguish several HP events occurring episodically from Eocene to Oligocene (Forster and Lister, 2005). The best exposures of HP rocks outcrop on the islands of Sifnos and Syros,

among many others in the region. The mechanism for the exhumation of blueschist and eclogite facies rocks is not well-understood. Some authors indicate that lithospheric decoupling during slab retreat is sufficient (Brun and Faccenna, 2008), while other authors suggest that exhumation of HP rocks was driven by syn-contractional extension (Ring et al., 2010).

The central Aegean has experienced approximately N-S backarc spreading since the Oligo-Miocene (Gautier and Brun, 1994; John and Howard, 1995; Gautier et al., 1999; Jolivet, 2001; Keay et al., 2001; Katzir et al., 2007; Brun and Faccenna, 2008; Jolivet and Brun 2010; Ring et al., 2010), extensively reworking the preexisting Alpine nappe stack through low-angle normal faulting (Lister et al., 1984; Lee and Lister, 1992; Gautier et al., 1993; Bricau et al., 2007; Jolivet et al., 2010). Extension has most likely been episodic and has resulted in crustal thinning from orogenic (>50 km) to attenuated lithospheric thickness of ~26 km in the central Aegean (Moho depth from Papanikolaou et al., 2004). The area has experienced up to ~580 km total extension (Brun and Faccenna, 2008). Regional, Holocene extension persists at a geologic rate of between 12 – 60 mm/yr (Taymaz et al., 1991; Brun and Faccenna, 2008), although up to 2 – 3 cm/yr of geodetic movement has been reported between the Aegean region and stable Eurasia (Jolivet, 2001). The central Aegean block is currently geodetically rigid – perhaps due to microplate locking from rotation (McClusky et al., 2000; Taymaz et al., 2001) – and thus, is largely aseismic (Figure 1). Modern strain is partitioned through seismically active normal faults and strike-slip systems in the Northern Aegean and surrounding areas (Taymaz et al., 1991).

## **GEOLOGY OF PAROS**

Paros is one of few Aegean islands that expose a nearly complete succession of footwall rocks and hanging wall sediments (Figure 2), which were laterally juxtaposed during core complex exhumation. The footwall rocks of Paros consist of highly deformed, quartz-rich, Carboniferous orthogneisses (Engel and Reischmann, 1998) intruded by abundant aplitic, pegmatitic, and rhyolitic dikes, as well as granites. The basement is overlain by intercalated amphibolite-facies marbles, micaschists, and amphibolites of the Cycladic Blueschist Unit (CBU) that have been retrograded by either isothermal decompression during exhumation or Barrovian overprinting (Jansen and Schuiling, 1976). Miocene metamorphism pervasively overprinted the earlier high-pressure signature (Gautier and Brun, 1994), although relict blueschist assemblages have been identified from correlative units on Naxos (Avigad, 1998). For a generalized t-T history of Paros, see Figure 3.

Paros has a complex deformational history involving at least three discrete deformational events. Based on kinematic indicators in the field (i.e. folded lineations, crosscutting relationships, superposed deformational fabrics, etc.), the island has undergone at least three episodes of deformation, possibly including extension and shortening in parallel directions (Papanikolaou, 1977; Gautier et al., 1993; Papp, 2007). A low-angle detachment separates the amphibolite-grade footwall core complex from the hanging wall (Figure 2), which comprises sedimentary rocks with questionable age and provenance. Early work interprets the basin fill as a transgressive backarc molasse deposit and biostratigraphically constrains deposition



of some sediment to the Early to Middle Miocene (Papageorgakis, 1968b; Papanikolaou 1977, 1980; Dermitzakis and Papanikolaou, 1980; Robert, 1982) and some to the Middle to Late Miocene (Böger, 1983). However, some authors acknowledge that interpretation of biostratigraphic data can be problematic when extensive sedimentary recycling occurs (Dermitzakis and Papanikolaou, 1980), as fossils can be reworked and redeposited. More recent studies have interpreted the sedimentary package as syn-extensional basin fill (Gautier and Brun, 1994; Sanchez-Gomez et al., 2002).

The hanging wall is dominated by clastic marine to continental sedimentary sequences of varying composition and is localized in a basin in northeast Paros (Figure 2). The stratigraphically lowest unit is a folded, incomplete marine sequence of uncertain provenance and tectonic origin. The marine units are overlain by compositionally variable conglomerates interbedded with sandstones of varying grain size, color, and bedding thickness. The sequence appears to be capped by Pliocene(?) limestone and travertine deposits (Dermitzakis and Papanikolaou, 1980). The depositional environments and sediment dispersal mechanisms of the hanging wall are largely unknown.

Though significant focus has been placed on the neighboring island of Naxos, several workers have performed geo- and thermochronometric analyses on Paros to help understand its tectonic evolution. Early  $^{40}\text{K}/^{39}\text{Ar}$  determinations indicate Miocene heating (Altherr et al., 1982) and a thermal history similar to that of Naxos, as described by Wijbrans and McDougall (1986, 1988) (Figure 3). A later apatite

fission-track (AFT) study of the Paros gneisses suggests rapid cooling during the Late Miocene (~8 – 12 Ma) on the order of  $70\text{ }^{\circ}\text{C}/\text{Ma}^{+60}_{-20}$  and a corresponding Miocene erosion rate of ~0.3 km/Ma (Hejl et al., 2003). Slip rates of 6 – 7 km/Ma have been calculated for Paros (Brichau et al., 2006) based on fission-track and (U-Th)/He dating of bedrock. Slip rates of ~5 km/Ma on Naxos (John and Howard, 1995) were calculated using hornblende  $^{40}\text{Ar}/^{39}\text{Ar}$  and biotite, white mica, and amphibole  $^{40}\text{K}/^{39}\text{Ar}$  thermochronometry. A detrital thermochronometric study of the sedimentary sections on Paros and Mykonos reveals two distinct age populations: 1) Miocene clasts between 9 – 16 Ma and 2) Eocene to Late Cretaceous clasts between 40 – 100 Ma (Sanchez-Gomez et al., 2002). These data indicate a complex structural and erosional history for Paros and the central Cyclades, which includes multiple episodes of deformation and deposition from several source terranes, possibly including a completely eroded overburden (Sanchez-Gomez et al., 2002). Detrital studies of the sedimentary deposits on Naxos corroborate a complex pre-extensional lithostratigraphy overlying present units on Paros and Naxos (Kuhlemann et al., 2004; Seward et al., 2009). These sediments may be genetically linked to those on Paros, since it is inferred that they share the same detachment fault (see Jolivet et al., 2010).

## **METHODS**

### *Apatite and Zircon (U-Th)/He Analysis*

All AHe and ZHe analyses were performed at the University of Kansas Isotope Geochemistry Laboratory (KU-IGL). Samples were separated using standard gravimetric, magnetic and heavy liquid techniques. Grains were hand-selected based

on crystal texture, color and size. Grains were excluded if anhedral, cracked, metamict (as indicated by brown coloration) or smaller than about 65  $\mu\text{m}$  (zircon) – 70  $\mu\text{m}$  (apatite). Some discretion was required to limit inherent sample bias toward magmatic grains in detrital suites. Individual grains were photographed and measured (height and width for apatite; height and one or two widths for zircon) for alpha-ejection correction (equations from Farley et al., 1996; Farley, 2002; Hourigan et al., 2005) and then sealed in Pt foil jackets for outgassing. For bedrock-derived samples, three single-grain (zircon) or multi-grain (apatite) aliquots were analyzed. For detrital samples, the number of aliquots varied, but were always single-grain.

Helium was extracted on either a Nd:YAG or a CO<sub>2</sub> diode laser (see review of apatite procedure in House et al., 2000). Multiple re-extracts were conducted to ensure that >99% of the <sup>4</sup>He gas was liberated. Extracted gas was spiked with <sup>3</sup>He, cryogenically purified, and measured under ultra-high vacuum ( $\geq 10^{-7}$  torr). Apatite aliquots were then spiked with a <sup>235</sup>U – <sup>230</sup>Th – <sup>149</sup>Sm enriched HNO<sub>3</sub> solution, dissolved in the Pt jackets by heating, and diluted with 500  $\mu\text{l}$  of deionized H<sub>2</sub>O. Zircon aliquots were similarly spiked, digested with HF, HNO<sub>3</sub> and HCl in Parr pressure digestion vessels, and diluted with 1000  $\mu\text{l}$  of deionized H<sub>2</sub>O. U-Th-Sm concentrations were measured on a VG Plasmaquad II ICP-MS or an Element 2 ICP-MS. Analytical errors are reported as 6% (2 $\sigma$ ) for apatite and 8% (2 $\sigma$ ) for zircon based on the long-term reproducibility of standards using the aforementioned techniques.

Laser ablation inductively coupled plasma mass spectrometry (LA-ICP-MS) U-Pb dating was performed at University of Arizona. At Arizona, about 50 euhedral grains with minimal inclusions from samples 08PA42 and 08PA43 were mounted in epoxy and polished to half-widths. After imaging with cathodoluminescent scanning electron microscopy (SEM-CL), about 20 grains from each sample were analyzed with a single 30  $\mu\text{m}$  diameter spot by an excimer laser. Crystallization ages were calculated from the weighted mean of the  $^{238}\text{U}/^{206}\text{Pb}$  ages. Errors are reported as  $2\sigma$ .

## RESULTS

### *Paros Footwall Structure*

Paros forms a NE-SW trending dome bounded to the east by a low-angle normal fault (Figure 2). The overall sense of slip is top to the north-northeast (Figure 4). The footwall of Paros is composed of gneisses, marbles and amphibolite schists intercalated with mica schists and amphibolites. The rocks were extensively sheared in a ductile regime, evidenced by the formation of tectonic fabrics, macro- and meso-scale folding and boudinage. The amphibolite-grade ortho- and paragneisses demonstrate penetrative tectonic fabrics, exhibiting classic mylonitic textures and  $\sigma$ -type stair stepping porphyroclasts. Stair stepping porphyroclasts ( $\sigma$ -type) indicating top to the northeast shear are nearly ubiquitous in the gneisses and occasionally observed in the marble (photo in Figure 5). Poorly developed shear bands occur rarely in the gneiss but are consistent with a NNE dipping shear. In many locations the lineation and foliation are crenulated or folded, making determinations of syn-kinematic orientation difficult. Additionally, there is a curvature to the lineation that

eventually becomes roughly orthogonal to the overall trend (Figure 4). The strain continuum is disrupted more so than on the neighboring islands of Tinos (Mehl et al., 2005) and Naxos. However, the broad trends of ductile and brittle deformation are consistent with a top to the NNE sense of shear.

Due to the localized changes in lineation and foliation orientation, the measurements have been subdivided into four domains (Figure 4). A total of 103 lineation measurements were taken with variable trend and plunge azimuth. The mean lineation dips  $18^{\circ}$  SE. A total of 104 foliation planes were measured with variable dip and dip azimuth. Considering the amount of spatial variation of the vectors, mean measurements are meaningless so considering means within arbitrary zones is more conducive to interpretation.

Footwall rocks also display late brittle deformation overprinting and crosscutting ductile fabrics. A total of 43 brittle fracture dips were measured including faults, mineralized fractures and Riedel shears in both the upper- and lower-plates of Paros. Fault planes have a wide range of dips between  $10^{\circ}$  -  $78^{\circ}$  and have dip directions from  $9^{\circ}$  to  $340^{\circ}$  (Figure 4), though they often occur in conjugate sets. The detachment fault zone is visible in few areas on Paros; it is mostly inferred by topography and where sedimentary rocks onlap the core complex. Only one exposure was able to be measured and gave a dip of  $10^{\circ}$  towards  $077^{\circ}$ . The lineation on the fault plane dips  $14^{\circ}$  towards  $060^{\circ}$ , indicating some component of oblique movement in the current orientation. The mean ductile extension direction is NNE, determined by synthesizing available lineation, foliation and fold measurements.

*Paros Footwall Geo- and Thermochronometry*

LA-ICP-MS zircon U-Pb ages were obtained for a rhyolitic dike (08PA42) and a nearby orthogneiss into which the dike intruded (08PA43) by LA-ICP-MS at the University of Arizona. The rhyolitic dike yields a  $^{238}\text{U}/^{206}\text{Pb}$  age of  $7.6^{+0.3}_{-0.2}$  Ma and a ZHe age of  $7.8 \pm 0.6$  Ma (mean age) (Tables 1, 2). The orthogneiss yields a zircon  $^{238}\text{U}/^{206}\text{Pb}$  age of  $311.5^{+1.5}_{-2.1}$  Ma and a ZHe age of  $8.1 \pm 0.6$  Ma (mean age) (Tables 1, 2). Chilled margins on the dike suggest that the footwall gneisses were already quite cool and quenched the rhyolite on intrusion.

A total of 112 ZHe aliquots were successfully analyzed from footwall orthogneisses and yield reproducible ages between  $6.4 \pm 0.5$  Ma and  $20.9 \pm 1.7$  Ma with an average age of  $9.2 \pm 0.7$  Ma (Table 2). To examine exhumation rate, ZHe data are plotted against latitude (a useful approximation for distance from the detachment) in Figure 5. Importantly, the (U-Th)/He ages exhibit no discernable spatial relationships, in contrast to the results of Brichau and others (2006). The age invariance indicates rapid cooling of sample through the  $200^\circ\text{C}$  isotherm during the Miocene. The AHe and ZHe ages are nominally the same within error (Tables 2, 3), suggesting that cooling from  $200^\circ\text{C}$  to  $60^\circ\text{C}$  took less than  $\sim 1$  Ma.

A total of 12 ZHe aliquots were analyzed from intrusive igneous rocks on Paros and range from  $6.6 \pm 0.5$  to  $10.7 \pm 0.9$  Ma (Figure 5). Oddly, the 5 AHe are all considerably older, from  $12.3 \pm 1.0$  to  $15.5 \pm 1.2$  Ma. The inconsistency aside, these results indicate a syn-kinematic thermal history for intrusives on Paros.

### *Hanging Wall Sedimentology, Stratigraphy and Thermochronometry*

The sedimentary rocks of Paros are localized in a basin on the northeast part of the island (Figure 2). The rocks outcrop sparsely and are generally isolated by brittle faulting and heavily weathered by erosion. Age relationships between outcrops are also difficult to determine due to the absence of marker beds. However, several outcrops contain information crucial to understanding the tectonic evolution of Paros and were evaluated in detail. This study focuses primarily on creating a stratigraphic framework around the coherent sections at Molos Bay and Alyki Bay, which contain the most continuous and useful stratigraphic successions and then attempts to fit other units into this framework.

A total of ~1 km of section was measured on Molos Peninsula (Figure 6). Three distinct units were identified. Stratigraphic descriptions were performed with high frequency to maximize understanding of the section. Bedding measurements were taken and clast counts were performed upsection, systematically where possible, (Figure 6) to complement thermochronometric sampling intervals. Clast counts were not performed on other units. Detrital thermochronometric data are presented in Tables 4 and 5.

The basal unit 1 unconformably overlies the Paros detachment fault. This 240 m thick unit is a tan, immature, fine- to medium-grained lithic arenite with gravel lenses and lobes interbedded with black, fine-grained shale. Bedding dips variably to opposing directions, as the unit is folded with axis trending NW-SE; overall bedding dips E (Figure 6). Small-scale faults are present and dip steeply to ENE. The faults

appear to be mostly of tectonic origin, but the unit has sustained extensive amounts of synsedimentary slumping and folding. Dewatering structures are present in the shale layers. Channel scours up to 0.5 m thick are present and quartz veins and barite overgrowths on fault planes were observed. Conglomeratic layers are often localized in channel scours and as lenses interrupting bedding and were counted to assess detrital lithologies (Figure 6). Clast and matrix supported conglomeratic lenses and layers in unit 1 are composed of quartz pebbles, reworked sandstones and metamorphic clasts (see clast petrology in Sanchez-Gomez et al., 2002) (Figure 6). The metamorphic clasts are generally quartz-rich and mylonitized, but varieties exist throughout the section. 60 ZHe analyses from Unit 1 range from  $18.5 \pm 1.5 - 121.4 \pm 9.7$  Ma. One ZHe age of  $13.3 \pm 1.1$  Ma was rejected due to intense metamictization (see discussion of metamictization in Nasdala et al., 2001). 5 AHe analyses from unit 1 yield ages from  $7.2 \pm 0.4 - 38.1 \pm 2.3$  Ma (Table 5). Ten AHe ages were rejected based on low He and/or low U. This unit is also exposed on Antikefalos peninsula (opposite Molos Peninsula, Figure 5), where part of the unit is biostratigraphically constrained to Early Miocene (Dermitzakis and Papanikolaou, 1980) which is in agreement with the ZHe maximum depositional age at Molos Bay.

A gradational contact separates the basal unit 1 from the overlying gray, immature, very fine to fine-grained lithic arenite with diffuse paraconglomeratic gravel lobes. Unit 2 is silty and field HCl tests indicate the presence of marl. Bedding dips are often obscured by extensive syn-sedimentary faulting and slumping, but generally dip eastward (Figure 6). Bedding size increases upsection from



laminations to ~0.5 m. The frequency of conglomeratic lenses also increases upsection. Barite mineralizations and channel scours are present. Clast counts were performed on gravel lobes and yield results indistinguishable from unit 1 (Figure 6). 12 ZHe analyses from unit 2 range from  $8.2 \pm 0.7$  to  $84.7 \pm 6.8$  Ma. Of note is a tan horizon that is present near the top of unit 2 containing granitic pebbles not previously observed in the section. The horizon is approximately 2 m thick (photo in Figure 6). Clast counts from the granitic horizon reveal the first igneous clasts observed in the sedimentary section. 13 ZHe analyses from the granitic horizon of unit 2 range from  $8.3 \pm 0.7$  to  $14.0 \pm 0.8$  Ma (Table 4). 7 AHe analyses from the granitic horizon of unit 2 range from  $8.9 \pm 0.5$  to  $40.1 \pm 2.4$  Ma (Table 5).

A sharp contact separates unit 2 from unit 3 and may be an unconformity, although the change in bedding dip azimuth is not pronounced. Unit 3 consists of yellow and red, medium- to coarse-grained lithic arenites interbedded with clast-supported conglomeratic layers. Beds still dip consistently eastward, although the dip angle shallows upsection. Igneous clast types introduced in the upper portion of unit 2 are also present in the lower portion of unit 3. The upper portion of unit 3 is dominated by large volcanic and plutonic clasts; the maximum clast size increases rapidly upsection and reach diameters in excess of ~1 m. Beds exhibit varying degrees of silicification. 56 ZHe ages from unit 3 range from  $6.6 \pm 0.5$  to  $113.3 \pm 9.1$  Ma. 10 AHe ages from unit 3 range from  $6.8 \pm 0.4$  to  $108.4 \pm 8.7$  Ma. 6 ZHe analyses from a rhyolite clast yield ages from  $6.4 \pm 0.5$  to  $8.3 \pm 0.7$  Ma. This clast

may be equivalent to the dacite clasts observed in this section by Sanchez-Gomez and others (2002).

A second section of ~0.2 km was measured near Alyki Bay (Figure 7) using the same methodology as was used at Molos Bay. Stratigraphic characterizations accompanied by bedding measurements and clast counts allow for a comprehensive understanding of the section. Unfortunately, the upper and lower bounds of the section are either not preserved or not exposed, so the complete stratigraphic context is unknown, although it presumably overlies, or is equivalent to unit 3 at Molos Bay based on the large percentage of marbles in the conglomerate which resemble those exposed in the footwall of Paros. The section from Alyki Bay is grouped together as unit 4.

Unit 4 comprises carbonaceous conglomerates which incorporate footwall-derived marble clasts and are folded with the axis of the anticline trending west. The average bedding dip is toward the WNW (Figure 7). Faults are difficult to characterize due to extensive syn-sedimentary slumping and faulting and appear to occur in conjugate sets that dip to the NE or SW (see brittle fractures in Figure 4). Closely spaced clast counts were performed to resolve any changes in detrital source, but reveal homogeneity throughout unit 4 (Figure 7). 9 ZHe ages from a SS lens within unit 4 range from  $8.4 \pm 0.7$  to  $104.0 \pm 8.3$  Ma (Table 4), while 7 AHe ages from unit 4 range from  $9.2 \pm 0.6$  to  $15.1 \pm 0.9$  Ma (Table 5).

There are several other outcrops of sedimentary rocks in NE Paros, but their correlation is difficult because the exposures are generally small and do not provide

adequate stratigraphic context. The northeastern tip of the island near the settlement of Santa Maria hosts an important outcrop with four distinct sedimentary units (Figure 8). Unit A is a sandy green-gray siltstone with paraconglomeratic lenses. Sandy layers from unit A yield 10 ZHe ages ranging from  $18.3 \pm 1.5$  to  $94.7 \pm 7.6$  Ma and 8 AHe ages ranging from  $8.5 \pm 0.5$  to  $13.8 \pm 0.8$  Ma. Overlying unit A is unit B, a heavily brecciated red orthoconglomerate; 10 ZHe ages from unit B range from  $18.3 \pm 1.5$  to  $105.3 \pm 8.4$  Ma. A rhyolitic clast was recovered from unit B and yields an average ZHe age of  $64.3 \pm 5.2$  Ma. The exposure is capped by unit C, a serpentinite block and unit D, a limestone interpreted as Pliocene by Dermitzakis and Papanikolaou (1980). None of these units appear visually correlative to those exposed at Molos or Alyki Bay, although maximum ZHe depositional ages indicate that the unit 1 and units A and B may have been deposited synchronously.

Other uncorrelated units include unit E, near Naoussa, a highly fossiliferous sandstone with 9 ZHe ages ranging from  $31.8 \pm 2.5$  to  $223.9 \pm 17.9$  Ma and 7 AHe ages ranging from  $8.0 \pm 0.5$  to  $17.2 \pm 1.0$  Ma (Figure 9). The depositional age for unit E was determined to be Late Oligocene – Early Miocene from biostratigraphy (Dermitzakis and Papanikolaou, 1980) and is in agreement with the maximum ZHe depositional age.

In central eastern Paros, unit F, purple conglomeratic layers and purple SS layers with 10 ZHe ages ranging from  $23.3 \pm 1.9$  to  $109.7 \pm 8.8$  Ma (Figure 9). Unit F is locally overlain by Unit G, a limestone biostratigraphically dated as Early Cretaceous (Papageorgakis 1968a). The limestone has been interpreted as part of a

transgression on the Paros footwall (Papanikolaou, 1977; Papanikolaou, 1980), but the ZHe maximum depositional age for the underlying conglomerate is Early Miocene, suggesting that this interpretation should be revised.

Unit Z comprises a lithic arenite collected near the village of Moutsouna on the neighboring island of Naxos and yields 12 ZHe ages that range from  $20.7 \pm 1.7$  to  $270.0 \pm 21.6$  Ma (Figure 9). No stratigraphic analyses were conducted at Moutsouna; the sample was collected and analyzed simply for the purpose of detrital thermochronometric age comparison.

## **DISCUSSION**

### *Miocene Development of the Paros Metamorphic Core Complex*

The crystallization age of the footwall gneiss of Paros is well-constrained to Carboniferous (Engel and Reischmann, 1999; this study) and probably corresponds to the intrusion age of Variscan granites. The later thermal history is not fully understood, but includes compression during Alpine orogenesis and Barrovian overprinting during extensional collapse and slab rollback (Figure 3). A Late Oligocene-Early Miocene onset of extension in the central Aegean has been suggested by many authors (e.g., John and Howard, 1995; Keay et al., 2001; Seward et al., 2009; Ring et al., 2010). Footwall AHe and ZHe ages were uniformly reset from 7 – 11 Ma during this extensional event (Figure 5) and yield the timing that the lower-plate rocks were rapidly cooled from 180 °C to 60 °C. The scatter in ages within any given sample is likely related to the mineralogy, as detailed study of these grains reveals heterogeneous parent nuclide distribution (Bargnesi, Chapter 3).

Structural characterization of the footwall rocks reveals deformation patterns associated with top to the NNE extensional Miocene tectonism (Figure 4) and is compatible with previous structural work (Lister et al., 1984; Gautier et al., 1993; Papp, 2007). The shear sense indicators were formed in a ductile regime during unroofing of the metamorphic core complex. Kinematic indicators from Alpine deformation have been overprinted by non-coaxial shear during crustal stretching, evidenced by asymmetric porphyroclasts (photo in Figure 5). Although the strain continuum is not completely preserved, the transition to upper crustal brittle deformation on Paros is not marked by an obvious change in the overall stress regime, which may have remained nearly uniform since the onset of extension (Ring et al., 2010). The absence of exposed chloritized zones, cataclastic fabrics and pseudotachylytes may only indicate their relative preservation potential and not a dynamic deformation rate. A curious phenomenon that eludes satisfactory explanation is that the mineral lineation on the island curves from parallel to the overall extension direction to orthogonal to it (Figure 4).

ZHe ages demonstrate rapid cooling rates and it is likely that they are linked to rapid exhumation during core complex unroofing and minimally affected by syn-extensional magmatism (Brichau et al., 2006). Therefore, the oldest footwall ZHe age is the earliest that the footwall rocks could have passed through the 180 °C crustal isotherm on their ascent to the surface. The ZHe data for the Paros orthogneisses yield ages invariant with distance from the detachment (Figure 5), indicating that exhumation driven cooling was exceptionally rapid and uniform. Since AHe data are

nominally the same age as the ZHe data, we know that the rate of cooling exceeds the difference between the two closure temperatures. A cooling rate of this magnitude may have significantly minimized the downdip younging relationship typically observed in metamorphic core complexes (e.g., Stockli et al., 2005). Samples with age scatter are close to the detachment and may be influenced by fluid advection-enhanced cooling or structural complexities (i.e., slivering).

An important question is whether the ZHe data can constrain the onset of extensionally driven exhumation of the Paros metamorphic core complex. The spatially invariant data show only the deepest structural paleodepths, where the thermochronometric data are uniformly reset by progressive core complex development. A more ideal dataset would encompass samples from shallower paleodepths, which often preserve the transition from completely to partially reset ages that can directly constrain the onset of extension and may preserve even earlier post-magmatic cooling signals related to background lithospheric uplift (Stockli, 2005). Since these thermochronometric signatures from shallow structural levels are absent, the ZHe ages do not truly constrain the initiation of extension, but rather define a period of rapid footwall exhumation and contribute to the understanding of the regional thermal history (Figure 3).

The footwall gneisses and overprinted CBU are heavily sheared and tectonically dismembered, but the intruded igneous rocks are only slightly deformed, exhibiting weakly developed shear bands and mineral lineations (Figure 5). ZHe and zircon U-Pb ages from an S-type pluton and an aplite dike indicate that these bodies

intruded into the basement syn-extensionally and were emplaced at  $15.5 \pm 0.3$  Ma (Appendix A). Based on these data, it is unlikely that the plutonic bodies predate extensional kinematics and act as a trigger for extension as has been postulated for core complex development in the past (Lister and Baldwin, 1993). A completely undeformed rhyolite dike from NW Paros yields slightly younger zircon U-Pb and ZHe ages of  $\sim 7.5$  Ma (Tables 1 and 2) and therefore provide a constraint on the timing of the ductile-brittle transition. Chilled margins on the dike indicate that the orthogneisses were already cool at the time of intrusion. It appears that the dike has been rotated, meaning that brittle deformation persisted at least into the latest Miocene.

Zircon U-Pb ages from the rhyolitic dikes of NW Paros confirm that ZHe ages from the same sample are crystallization ages. Based on the timing, it is possible that subduction-related arc volcanism was active locally in the Late Miocene ( $\sim 7$  Ma). Pliocene volcanism of similar composition is present to the southwest on the island of Antiparos (4 - 5 Ma from Innocenti et al., 1982) and may record the southern retreat of the volcanic arc. Felsic arc volcanism is typically associated with heating of the continental crust, which often produces bimodal volcanism in extensional settings. However, mafic-type volcanic rocks are present only as enclaves in the Paros rhyolites (Hannapel and Reischmann, 2005) and are not present on surrounding islands. It appears that “capping basalts” common in extensional footwalls of the Basin and Range province of the Western USA (Anderson et al., 1983) are absent.

To approximate slip rate, exhumation rate, paleodepth and erosion rate, we assume a geothermal gradient of  $50 \pm 20$  °C/km (a common synextensional, upper crustal thermal gradient during core complex development from Ketcham, 1996). Since the range of ZHe and AHe ages overlap within error, we know that the cooling rate for the footwall is  $>100$  °C/Ma ( $70$  °C/Ma  $^{+60}_{-20}$  from Hejl and others (2003),  $\sim 120$  °C from this study) and can use this data to obtain a closure temperature of  $180$  °C for helium in zircon (Reiners, 2005). Therefore, ZHe data from orthogneisses suggests that the core complex was at relatively shallow structural levels ( $3.5^{+2.5}_{-1.0}$  km) around  $9$  Ma. Using a slip rate of  $7 \pm 2$  mm/yr (minimum from Naxos slip rates from John and Howard, 1995 and maximum from common slip rates in core complexes from Ketcham, 1996) and having constrained the current dip of the fault to  $10 \pm 2^\circ$ , the footwall should have  $\sim 1 - 2$  km of vertical throw per Ma. This means that the currently exposed footwall rocks were exhumed to the surface by  $5.5 \pm 2$  Ma. Given the large uncertainty and amount of assumptions, this is not a well-constrained approximation, but can establish that this interpretation is reasonable.

A final point is that AHe data are somewhat problematic for kinematic interpretations because they produce apparent ages older than ZHe data. With rapid, exhumation-driven cooling, the AHe and ZHe ages should be identical within error. Since the ZHe ages are uniformly reset by temperatures  $\geq 180$  °C, we can rule out the presence of an apatite paleo-PRZ recorded in the footwall ages to explain the scatter in AHe data. The resulting explanation for the inverted ages is not tectonic, but



results from the presence of highly U-enriched rims on zircon grains (Bargnesi, Chapter 3).

#### *Supradetachment Basin Evolution at Molos and Alyki Bay*

The detailed stratigraphic evaluation provides the context in which to place the clast counts and detrital thermochronometric data. The ~1 km thick stratigraphic section measured at Molos Bay contains the most vital information regarding sedimentation on Paros because it is nearly complete and the detachment is visible at the base. The ~0.2 km stratigraphic section at Alyki Bay is also important because it provides insight into late-stage sedimentation on Paros. The following section attempts to correlate the sections at Molos and Alyki Bay with other sedimentary outcrops on Paros (Figure 11) and to synthesize the tectonosedimentary evolution of the island (Figures 12 - 13).

In order to properly extract useful information from detrital AHe and ZHe data, it must be first assessed if ages were reset by burial following deposition. Using the same variables assumed during calculation of the footwall geothermal gradient and paleodepth, we can estimate the rate at which the eroded overburden was removed and assess the plausibility of post-depositional resetting of AHe ages. If we assume slip on the Paros-Naxos detachment ceased by ~5 Ma and subtract the present-day topography, there has been at least 1 km of erosion. This gives an erosion rate of ~0.2 km/Ma, which is in agreement with the modeled Miocene erosion rate of ~0.3 km/Ma (Hejl et al., 2003). Since structural quiescence was reached around 5 Ma, sedimentation may have slowed, or even ceased around this time.

Using the estimated erosion rates, we obtain ~1 – 1.5 km of missing section that was present in the Late Miocene (~5 Ma). Adding the removed thickness to the current estimate of the minimum stratigraphic thickness, and assuming a normal upper-plate geothermal gradient of 25 °C/km, the basal units of the sedimentary succession would have easily exceeded the nominal closure temperature for helium in apatite (~70 °C, from Wolf et al., 1996). It is also possible that the succession was even thicker during the Middle Miocene, although low lag times expected during rapid core complex exhumation suggest this may not be the case. This useful approximation establishes that during the Late Miocene, the sedimentary stack was probably thick enough to partially reset AHe ages, but certainly not thick enough to reset ZHe ages.

Detailed structural measurements provide additional evidence about the development of the basin. The beds of unit 1 dip almost uniformly eastward (Figure 6). This probably does not indicate any type of paleocurrent or depositional trend, but rather tilting from progressive core complex development as the unit accommodates footwall uplift. The average bedding dip angle is ~45°. Tilting of this magnitude has clearly contributed to the destruction of sedimentary outcrops on Paros. In addition, the dewatering structures in the shaley layers suggest that deposition was rapid, so relatively thick sedimentary layers may correspond to comparatively short timespans and the preservation potential for sedimentary structures is low. The clast composition of this unit includes both metamorphic and sedimentary rocks, indicating active cannibalism of previously deposited sediments. Individual metamorphic clast types were identified by Sanchez-Gomez and others (2002), but here are lumped

together as schists and are attributed to the tectonically overlying, undifferentiated Pelagonian-type units. A possible source of the sedimentary clasts is recycled Paleocene and Eocene syn-orogenic flysch, as suggested for outcrops on Naxos by Kuhleemann and others (2004). Basins containing Early Tertiary Alpine sediments are common in continental Greece and may have been present throughout the Cyclades prior to extension (Figure 12).

The detrital ZHe signatures from unit 1 show several overlapping age populations from 16 – 40 Ma, 40 – 60 Ma, 60 – 80 Ma and some ages > 100 Ma (Figures 9 and 10), which are consistent with a published detrital white mica  $^{40}\text{Ar}/^{39}\text{Ar}$  age of  $94 \pm 1$  Ma from equivalent strata on Paros (Sanchez-Gomez et al., 2002) and appear to record discrete tectonometamorphic events of the central Aegean Sea (events shown in Figure 8). The ages suggest continuous deformation and deposition from the Cretaceous to the Miocene, which means that large quantities of upper-plate sedimentary rocks escaped complete thermal resetting of helium in zircon by remaining in unmetamorphosed hanging walls during Alpine tectonism, although partial resetting may explain some of the overlap in populations.

The youngest detrital ZHe age (~13 Ma) from unit 1 appears to have been affected by severe metamictization and is considered unreliable (discussion in Nasdala et al., 2001). We therefore interpret the next youngest age from the stratigraphically lowest sample to represent the maximum depositional age of ~19 Ma, compatible with the biostratigraphic analyses of Dermitzakis and Papanikolaou

(1980). Marine deposition at this time is related to rapid deepening of the basin by the onset of extensional tectonics (Figure 12).

AHe ages from unit 1 appear to be reset to 7 – 13 Ma, similar to other sedimentary units on Paros. These Miocene ages must be related to either pre- or post-depositional resetting. Pre-depositional resetting would suggest that rocks that had passed through the AHe closure isotherm (~70 °C) were already exposed at the surface and actively eroding by ~7 Ma, which would become the effective depositional age of the unit. Another possibility is that the detrital source is structurally shallow footwall rocks which retain the ZHe PRZ, while the apatites are completely reset. However, cooling rates in the exposed section of the footwall indicate that rocks crossed the AHe PRZ and the ZHe PRZ within 1 Ma. Under these conditions, retention of a ZHe PRZ would be unlikely, as it takes significant timespans to develop partially reset ages. In contrast, post-depositional resetting would mean that at least 2 km of overburden were present at ~7 Ma (assuming a normal upper-plate geothermal gradient) to elevate the temperature of unit 1 to >50 °C and has since been eroded, a hypothesis validated above. A lone ~38 Ma AHe age may reflect sedimentary recycling or deposition of unreset apatites from the structurally highest unit in the pre-existing Alpine nappe stack (Figure 12). The simplest explanation is that resetting occurred post-depositionally, which also agrees with the biostratigraphic constraints on unit 1 (Dermitzakis and Papanikolaou, 1980).

The beds of unit 2 have a very similar structural character to unit 1 (Figure 5). Since the clast compositions between the two units are also indistinguishable, it

appears that the detrital sources are genetically related, although the depositional style has changed to reflect lower energy. The similarities are further reflected in the detrital ZHe age signals. The grain populations from unit 2 have similar populations to unit 1, although the proportion of zircon grains <20 Ma is higher (Figure 12), and the maximum deposition is much younger (~8 Ma). This upsection-developing younging signature is indicative of a progressive unroofing sequence eroding into the basin. The granitic horizon probably represents the first pulse of locally footwall-derived detritus into the basin. AHe and ZHe ages from the granitic horizon are uniformly reset between 8 – 14 Ma, which could correspond to several different plutons exposed regionally (Pe-Piper and Piper, 2002), including the granitic rocks of Paros. These ages were reset prior to deposition, since it is clear that any overburden was not significant enough to reset ZHe ages from underlying sedimentary units.

The beds of unit 3 also dip uniformly to the east, although a shallowing dip angle ~25° indicates about 20° of differential vertical tilt when compared to unit 1 and 2. This is a consequence of progressive exhumation during deposition leading to decreased tilt downdip from the detachment. Unit 3 contains similar clast types to units 1 and 2, which we interpret as the background sedimentation or the continual recycling and reworking of unreset and/or partial reset rocks in longitudinal and transverse drainages. The increasing percentage of igneous clast types upsection in unit 3 (Figure 6) is related to the progressive unroofing of these rocks from emplacement depths to the surface and may be sourced directly from Paros. Detrital AHe and ZHe from unit 3 are almost uniformly reset to 6 – 13 Ma, a signal

indistinguishable from the locally exposed Paros footwall. This observation indicates the continued evolution of an unroofing sequence whereby rocks from increasingly deeper structural depths are eroded and deposited (Figures 12 - 13). Additionally, ZHe ages from a rhyolitic clast yield ages identical to those from the rhyolitic dike of Paros, strongly suggesting that these rocks were exposed and eroding by 6 Ma and further supporting detrital input from currently exposed rocks or their equivalents. Work by Sanchez-Gomez and others (2002) indicated that these were dacite clasts of unknown origin. However, locally derived rhyolitic detritus is a more plausible explanation.

The bedding for unit 4 is angularly discordant to those at Molos Bay, with an average dip direction of WNW (Figure 7). The unit is folded into an anticline and heavily brecciated along fault zones (Figure 7). Clast compositions have are fundamentally different than those at Molos Bay. The dominant clast types from units 1 - 3 are no longer present and are replaced by marble, amphibolite, limestone and silicified clasts (silex) (Figure 7). These clast types strongly resemble rocks currently exposed in the Paros footwall, which is the primary detrital source to unit 4. The AHe and ZHe detrital ages for unit 4 are almost uniformly reset, similarly to unit 3 (Figures 8 - 9). It is possible units 3 and 4 were deposited simultaneously based on the ZHe minimum depositional ages and the lack of stratigraphic context for unit 4; however, based on the dominance of clast-types from shallow structural levels (i.e. marbles, undeformed limestones), it is also possible that unit 4 is considerably younger than unit 3 (Figure 11).

### *Stratigraphic Correlations in the Paros Supradetachment Basin*

The stratigraphic evaluation of exposed section at Molos Bay and Alyki Bay provides an understanding of basin creation and progressive evolution in the Miocene. Depositional timing and style are tectonically controlled by the structural and erosional unroofing of the Paros metamorphic core complex. The integrated approach of sedimentology and thermochronology shows that the supradetachment basin hosts a classic unroofing sequence, whereby thermal signatures from increasingly deeper structural levels are recorded in detrital age signals (Figure 12). The analysis of previous sections has created a framework with which to interpret other important outcrops of sedimentary rocks on Paros.

Detrital ZHe ages from unit A and unit B constrain the maximum deposition ages to ~19 and ~18 Ma, respectively. The grain populations have indistinguishable age signatures and may share detrital sources, even though depositional style has changed. There are two distinct ZHe age populations that appear to reflect major episodes of regional tectonic activity: 1) Late Cretaceous onset of subduction and 2) Late Oligocene to Early Miocene onset of large magnitude extension. Curiously absent are Eocene sources related to peak HP metamorphism (Figure 3). An interesting rhyolitic clast (z08PA14) was removed from unit B and yielded reproducible ages of ~64 Ma (n = 2, Table 4). Regional volcanism of this age is undocumented, so it is not likely that the ZHe ages are 1<sup>st</sup> cycle crystallization ages. It is important to note that the clasts are not Miocene and cannot be correlated to clasts of similar composition in unit 3. The depositional timing of units A and B are

correlative to unit 1 at Molos Bay. It is conceivable that the variation in clast lithology was produced by lateral variation in source. The AHe ages for unit A are uniformly reset to 8 – 14 Ma (Table 5). This introduces a similar problem to that outlined during discussion of unit 1 at Molos Bay. Since this unit is correlative with unit 1, it is likely that the apatites were partially or completely reset during peak sedimentary succession thickness in the Middle Miocene.

The relationship between unit B and the overlying unit C is not clear. The contact is intensely brecciated and appears unconformable. The geometry and contact with unit B indicate that the serpentinite block may be an olistolith related to erosion of Pindos units or to recycling of an ophiolitic *mélange* block. The contact between unit C and D was not observed, but it is implied that the limestones of D are younger because they are flat-lying and undeformed. Some authors have suggested a Pliocene age (Dermitzakis and Papanikolaou, 1980) for these units. Although compelling evidence is lacking, stratigraphic relationships do support this hypothesis (Figure 11). Units C and D have no equivalent strata in Molos and Alyki Bay, although unit D is almost certainly the youngest unit mentioned thus far.

No significant stratigraphic analyses were performed on the outcrop near Naoussa. ZHe ages from unit E constrain deposition to Early Oligocene and exhibit wide scatter between 32 and 224 Ma (Figure 8). The AHe ages for unit E are post-depositionally reset from 8 – 17 Ma (Table 5). Based on the ZHe maximum depositional age, this may be the oldest sedimentary unit on Paros (Figure 11). The oldest grain (z08PA54-7, Table 4) is interesting because it has survived multiple



tectonic episodes without being fully reset. Provenance of this age may correspond to Triassic volcanism reported by Brocker and Keasling (2006). Since only 9 ZHe ages were obtained, it is a statistical likelihood that some detrital populations are not adequately represented or even missing (Vermeesch, 2005).

Upper-plate detrital (U-Th)/He data from unit F show that limestone blocks of unit G are olistoliths and not part of an Early Cretaceous transgressive sequence on Paros as was previously interpreted (Papanikolaou, 1977; Dermitzakis and Papanikolaou, 1980). ZHe ages range from 23 to 110 Ma, constraining the maximum age of deposition to Early Miocene. In fact, every grain gives an age younger than the proposed Barremian age (125 – 130 Ma) (Papageorgakis, 1968a). Neither the limestone blocks nor the underlying sediments appear to have experienced any metamorphism, indicating that post-depositional reheating to the zircon PRZ is very unlikely. Based on the ZHe maximum depositional age, we interpret that this unit is near the base of the sedimentary sequence and is either coeval with or slightly older than unit 1. The spread in ages is similar to units A and B, but contains two grains of Eocene age. This may indicate: 1) coeval deposition by different sources; 2) a difference in stratigraphic age; or 3) failure to capture all statistically significant detrital signals using ZHe dating (Vermeesch, 2005). A possible source for the limestone olistolith is Late Cretaceous ophiolitic *mélange* breakup, similar to the source for the serpentinitic olistolith. If this is true, the presence of these blocks could indicate coeval deposition of unit C and unit G.

One sample was collected from Moutsouna on the eastern flank of the island of Naxos. Since it is inferred that Paros and Naxos share the same detachment (Figure 13) and detrital thermochronometric ages in the Aegean are scarce, we may be able to use detrital ages from Naxos of Kuhlemann and others (2004) and Seward and others (2009) to aid in interpretation. ZHe ages from Moutsouna agree nicely with the data from lower strata in Paros (Figure 8). ZHe ages constrain deposition of the basal SS to 21 Ma (Figure 11), although a younger age is possible. ZHe ages exhibit similar detrital signals to those revealed by similar analyses on rocks from Paros.

## CONCLUSIONS

Sedimentary rocks from Paros contain crucial information pertaining to the tectonic evolution and syn-kinematic history of the Central Aegean. Unfortunately, it is impossible to determine if, or how much, of the pre- and syn-kinematic sedimentary section may have been structurally excised by the detachment; the apparent absence of pre-rift sediments indicates that at least some of the section has been structurally removed or eroded and recycled. We show that sedimentary rocks have been continuously recycled perhaps since the Permian and have escaped thermal resetting from subsequent tectonometamorphic events. A modern analog for this process may exist in Crete, where upper-plate sediments have not been affected by recent metamorphic activity (Thomson et al., 1999). By analyzing the AHe and ZHe age and correlating to a growing database of thermochronometry in the Aegean Sea, as well as using stratigraphy and sedimentology, we can unravel the source and

transportation of these grains from the surrounding area into the Paros supradetachment basin.

Since the AHe and ZHe ages are nominally identical, footwall rocks of Paros have undergone rapid cooling at rates  $>100$  °C/Ma from 7 – 16 Ma. The new U-Pb zircon ages suggest that the rhyolitic dikes of Paros identified recently by Hannapel and Reischmann (2005) are  $7.8 \pm 0.2$  Ma old. Crosscutting relationships between the dikes, which contain chilled margins, and the gneisses of the MCC indicate that ductile deformation ceased at  $\sim 7$  Ma; brittle faulting indicates that deformation continued.

Paros exposes conglomerates with variable source lithologies, which reflects footwall and hanging wall input into the basin during regional tectonic deformation and local interleaving of strata through low angle normal faults and possibly reverse faults. The detrital ZHe ages from the sedimentary sequence contain a strong Miocene signal indistinguishable from lower-plate cooling ages, which confirms a Miocene supradetachment basin environment and input of footwall material into the basin. The use of (U-Th)/He thermochronometry reveals the thermal evolution of the source rocks to the supradetachment basin.

Eocene to Miocene detrital ZHe in underlying strata indicate that large limestone blocks near the base of the sedimentary sequence are not part of an Early Cretaceous transgressive sequence as interpreted by Dermitzakis and Papanikolaou (1980), but rather olistoliths shed into the basin during progressive basin formation in the Miocene.

At least three distinct thermochronometric age populations can be identified from the (U-Th)/He ages in the Paros supradetachment basin and correlated to major regional tectonometamorphic events: Cretaceous Pelagonian-type metamorphism (85 – 100 Ma from Lips et al., 1998), Eocene HP metamorphism (35 – 50 Ma from Bröcker and Enders, 1999; Tomaschek et al., 2003; Putlitz et al., 2005), and extension induced lithospheric heating during the Miocene (7 – 25 Ma from Seward et al., 2009; this study). Uniformly reset detrital AHe ages in the basal sedimentary unit indicate post-depositional resetting; detrital ZHe ages record thermal signals from all three major regional events and Miocene deposition of multiple cycle sedimentary grains. The age signatures of the overlying units suggest progressive exhumation and erosion of the Paros core complex into a supradetachment basin. Thermochronometric data confirm the rapid cooling of the Paros MCC and deposition of progressively unroofed overlying units into the Paros supradetachment basin during the Miocene.

## CHAPTER 2: REFERENCES

- Allmendinger, R.W., 1986. Stereonet for Windows. Cornell University, NY.
- Altherr, R., Kreuzer, H., Wendt, I., Lenz, H., Wagner, G.A., Keller, J., Harre, W., Hohndorf, A., 1982. A late Oligocene/early Miocene high temperature belt in the Attic-Cycladic crystalline Complex (S.E. Pelagonian, Greece). *Geol. Jb.* E23, 97–164.
- Anderson, R.E., Zoback, M.L., Thompson, G.A., 1983. Implications of selected subsurface data on the structural form and evolution of some basins in the northern Basin and Range province, Nevada and Utah. *GSA Bulletin*. 94, 1055–1072.
- Avigad, D., Garfunkel, Z., 1991. Uplift and exhumation of high-pressure metamorphic terrains: the example of the Cycladic blueschist belt (Aegean Sea). *Tectonophysics*. 188, 357–372.
- Avigad, D., 1998. High-pressure metamorphism and cooling on SE Naxos (Cyclades, Greece), *European Journal of Mineralogy*. 10, 1309–1319.
- Bernet, M., Spiegel, C., 2004. Introduction: Detrital Thermochronology, in: Bernet, M., Spiegel, C. (Eds.), *Detrital Thermochronology – Provenance analysis, exhumation, and landscape evolution of mountain belts*. Geological Society of America Special Paper. 378, 1–6.
- Böger, V.H., 1983. Stratigraphische und tektonische Verknüpfungenkontinentaler Sedimente des Neogens im Ägäis-Raum. *Geol.Rundschau*. 72, 771–814.

- Brichau, S., Ring, U., Ketcham, R.A., Carter, A., Stockli, D., Brunel, M., 2006. Constraining the long-term evolution of the slip rate for a major extensional fault system in the central Aegean, Greece, using thermochronology. *Earth and Planetary Science Letters*. 241, 293 – 306.
- Brichau, S., Ring, U., Carter, A., Monié, P., Bolhar, R., Stockli, D., Brunel, M., 2007. Extensional faulting on Tinos Island, Aegean Sea, Greece: How many detachments?. *Tectonics*. 26, TC4009.
- Bröcker, M., Enders, M., 1999. U-Pb zircon geochronology of unusual eclogite-facies rocks from Syros and Tinos (Cyclades, Greece). *Geol. Mag.* 136, 111–118.
- Bröcker, M., Keasling, A., 2006. Ionprobe U-Pb Zircon ages from the high-pressure/low-temperature mélange of Syros, Greece: age diversity and the importance of pre-Eocene subduction. *Journal of Metamorphic Geology*. 24, 615–631.
- Bröcker, M., Pidgeon, R.T., 2007. Protolith ages of meta-igneous and metatuffaceous rocks from the Cycladic blueschist unit, Greece: results of a reconnaissance U-Pb zircon study. *Journal of Geology*. 115, 83–98.
- Brun, J.-P., Faccenna, C., 2008. Exhumation of high-pressure rocks driven by slab rollback. *Earth and Planetary Science Letters*. 272, 1–7.
- Buick, I.S., Holland, T.J.B., 1989. The P-T-t path associated with crustal extension, Naxos, Cyclades, Greece. *Geological Society of London Special Publication*. 43, 365–369.

- Carrapa, B., Wijbrans, J., Bertotti, G., 2004. Detecting provenance variations and cooling patterns within the western Alpine orogen through  $^{40}\text{Ar}/^{39}\text{Ar}$  geochronology on detrital sediments: The Tertiary Piedmont Basin, northwest Italy, in: Bernet, M., Spiegel, C. (Eds.), Detrital Thermochronology – Provenance analysis, exhumation, and landscape evolution of mountain belts. Geological Society of America Special Paper. 378, 67–103.
- Dermitzakis, M., Papanikolaou, D., 1980. The molasse of Paros Island, Aegean Sea. Ann. Naturhist. Mus. Wien. 83, 59–71.
- Dewey, J.F., Sengor, A.M.C., 1979. Aegean and surrounding regions: Complex multiplate and continuum tectonics in a convergent zone. GSA Bulletin, Part I. 90, 84–92.
- Dürr, S., Altherr, R., Keller, J., Okrusch, M., Seidel, E., 1978. The Median Aegean Crystalline Belt: Stratigraphy, structure, metamorphism, magmatism, in: Closs, H. et al. (Eds.), Alps, Apennines, Hellenides. IUCG Sci. Rep. 38, 455–477.
- Engel, M., Reischmann, T., 1998. Single zircon geochronology of orthogneisses from Paros, Greece. Bulletin of the Geological Society of Greece. 32, 91–99.
- Farley, K.A., Wolf, R., Silver, L., 1996. The effects of long alpha-stopping distances on (U-Th)/He ages. Geochimica et Cosmochimica Acta. 60, 4223–4229.
- Farley, K.A., 2002. (U-Th)/He dating: Techniques, calibrations, and applications, in: Porcelli, D., Ballentine, C.J., Wieler, R. (Eds.), Noble Gases in Geochemistry

- and Cosmochemistry. *Reviews in Mineralogy and Geochemistry*. 47, 559–577.
- Forster, M.A., Lister, G.S., 2005. Several distinct tectono-metamorphic slices in the Cycladic eclogite-blueschist belt, Greece. *Contributions to Mineralogy and Petrology*. 150, 523–545.
- Friedmann, S.J., Burbank, D.W., 1995. Rift basins and supradetachment basins: intracontinental extensional end-members. *Basin Research*. 7, 109–127.
- Gautier, P., Brun, J.-P., Jolivet, L., 1993. Structure and kinematics of Upper Cenozoic extensional detachment on Naxos and Paros (Cyclades Islands, Greece). *Tectonics*. 12, 1180–1194.
- Gautier, P., Brun, J.-P., 1994. Crustal-scale geometry and kinematics of late-orogenic extension in the central Aegean (Cyclades and Evvia Island). *Tectonophysics*. 238, 399–424.
- Gautier, P., Brun, J.-P., Moriceau, R., Sokoutis, D., Martinod, J., Jolivet, L., 1999. Timing, kinematics and cause of Aegean extension: a scenario based on a comparison with simple analogue experiments. *Tectonophysics*. 315, 31–72.
- Gawthorpe, R.L., Leeder, M.R., 2000. Tectono-sedimentary evolution of active extensional basins. *Basin Research*. 12, 195–218.
- Hannappel, A., Reischmann, T., 2005. Rhyolitic dykes of Paros Island, Cyclades, in: Fytikas, M., Vougioukalakis, G.E. (Eds.), *The South Aegean Active Arc: Present knowledge and future perspectives*, Elsevier, pp. 305–328.



- Harrison, M.T., Grove, M., Lovera, O., Zeitler, P., 2005. Continuous Thermal Histories from Inversion of Closure Profiles, in: Reiners, P.W., Ehlers, T.A. (Eds.), *Low-Temperature Thermochronology: Techniques, Interpretations, and Applications. Reviews in Mineralogy and Geochemistry*. 58, p. 389–409.
- Hejl, E., Riedl, H., Soulakellis, N., Van Den Haute, P., Weingartner, H., 2003. Young Neogene tectonics and relief development on the Aegean islands of Naxos, Paros and Ios (Cyclades, Greece). *Mitt. Osterr. Geol. Ges.* 93, 105–127.
- Hourigan, J.K., Reiners, P.W., Brandon, M.T., 2005. U-Th zonation-dependent alpha-ejection in (U-Th)/He chronometry. *Geochimica et Cosmochimica Acta*. 60, 3349–3365.
- House, M.A., Farley, K.A., Stockli, D.F., 2000. Helium chronometry of apatite and titanite using Nd:YAG laser heating. *Earth and Planetary Science Letters*. 183, 365–368.
- Innocenti, F., Kolios, N., Manetti, P., Rita, F., Villarei, L., 1982. Acid and basic late Neogene volcanism in Central Aegean Sea: its nature and geotectonic significance. *Bulletin of Volcanology*. 45, 87–97.
- Jackson, J., 1994. Active Tectonics of the Aegean Region. *Annu. Rev. Earth Planet. Sci.* 22, 239–271.
- Jansen, J.B.H., 1977. The Geology of Naxos, Greece. *Geological and Geophysical Research*. 19, 1–100.
- Jansen, J. B. H., Schuiling, R. D., 1976. Metamorphism on Naxos; petrology and geothermal gradients. *American Journal of Science*. 276, 1225–1253.

- John, B.E., Howard, K.A., 1995. Rapid extension recorded by cooling-age patterns and brittle deformation, Naxos, Greece. *Journal of Geophysical Research*. 100, 9969–9979.
- Jolivet, L., 2001. A comparison of geodetic and finite strain pattern in the Aegean, geodynamic implications. *Earth and Planetary Science Letters*. 187, 95–104.
- Jolivet, L., Brun, J.-P., 2010. Cenozoic geodynamic evolution of the Aegean. *International Journal of Earth Sciences*. 99, 109–138.
- Katzir, Y., Garfunkel, Z., Avigad, D., Matthews, A., 2007. The geodynamic evolution of the Alpine orogen in the Cyclades (Aegean Sea, Greece): insights from diverse origins and modes of emplacement of ultramafic rocks, in: Taymaz, T., Yilmaz, Y., Dilek, Y. (Eds.), *The Geodynamics of the Aegean and Anatolia*, Geological Society of London Special Publication. 291, 17–40.
- Keay, S., 1998. The geological evolution of the Cyclades, Greece: constraints from SHRIMP U–Pb geochronology. Ph.D thesis. Australian National University.
- Keay, S., Lister, G.S., Buick, I.S., 2001. The timing of partial melting, Barrovian metamorphism and granite intrusion in the Naxos metamorphic core complex, Cyclades, Aegean Sea, Greece. *Tectonophysics*. 342, 275–312.
- Ketcham, R.A., 1996. Thermal models of core-complex evolution in Arizona and New Guinea: Implications for ancient cooling paths and present-day heat flow. *Tectonics*. 15, 933–951.

- Kuhlemann, J., Frisch, W., Dunkl, I., Kázmér, M., Schmiedl, G., 2004. Miocene siliciclastic deposits of Naxos Island: Geodynamic and environmental implications for the evolution of the southern Aegean Sea (Greece), in: Bernet, M., Spiegel, C. (Eds.), Detrital Thermochronology – Provenance analysis, exhumation, and landscape evolution of mountain belts. Geological Society of America Special Paper. 378, 51–65.
- Lee, J., Lister, G.S., 1992. Late Miocene ductile extension and detachment faulting, Mykonos, Greece. *Geology*. 20, 121–124.
- Lister, G.S., Baldwin, S.L., 1993. Plutonism and the origin of metamorphic core complexes. *Geology*. 21, 607–610.
- Lister, G.S., Banga, G., Feenstra, A., 1984. Metamorphic core complexes of Cordilleran type in the Cyclades, Aegean Sea, Greece. *Geology*. 12, 221–225.
- Lips, A.L.W., White, S.H., Wijbrans, J.R., 1998.  $^{40}\text{Ar}/^{39}\text{Ar}$  laserprobe direct dating of discrete deformational events: a continuous record of early Alpine tectonics in the Pelagonian Zone, NW Aegean area, Greece. *Tectonophysics*. 298, 133–153.
- McClusky, S., Balassanian, S., Barka, A., Demir, C., Ergintav, S., Georgiev, I., Gurkan, O., Hamburger, M., Hurst, K., Kahle, H., Kastens, K., Keklidze, G., King, R., Kotzev, V., Lenk, O., Mahmoud, S., Mishin, A., Nadariya, M., Ouzonis, A., Paradissis, D., Peter, Y., Prilepin, M., Reilinger, R., Sanli, I., Seeger, H., Tealeb, A., Toksoz, M.N., Veis, G., 2000. Global positioning system constraints on plate kinematics and dynamics in the eastern

- Mediterranean and Caucasus. *Journal of Geophysical Research*. 105, 5695–5720.
- Mehl, C., Jolivet, L., Lacombe, O., 2005. From ductile to brittle: Evolution and localization of deformation below a crustal detachment (Tinos, Cyclades, Greece). *Tectonics*. 24, TC4017.
- Nasdala, L., Wenzel, M., Vavra, G., Irmer, G., Wenzel, T., Kober, B., 2001. Metamictisation of natural zircon: accumulation versus thermal annealing of radioactivity-induced damage. *Contributions to Mineralogy and Petrology*. 141, 125–144.
- Negris, P.H., 1915-1919. *Roches cristallophylliennes et Tectonique de la Grèce*, Athènes.
- Papageorgakis, J., 1968a. A Cretaceous outcrop on the island of Paros. *Prakt. Acad. Athens*. 43, 162–174.
- Papageorgakis, J., 1968b. The presence of marine Miocene on the island of Paros. *Prakt. Acad. Athens*. 43, 368–376.
- Papanikolaou, D., 1977. On the Structural Geology and Tectonics of Paros Island, Aegean Sea. *Annales Géologiques Des Pays Helléniques*. 28, 450–464.
- Papanikolaou, D., 1980. Contribution of the geology of the Aegean Sea. *Annales Géologiques Des Pays Helléniques*. 29, 477–533.

- Papanikolaou, D., 1989. Are the medial crystalline massifs of the eastern Mediterranean drifted Gondwanan fragments?. Geological Society of Greece Special Publication. 1, 63–90.
- Papanikolaou, D., 1993. Geotectonic evolution of the Aegean. Bulletin of the Geological Society of Greece. 28, 33–48.
- Papanikolaou, D., 1996. Geological Map of Paros. IGME.
- Papanikolaou, D., 2009. Timing of tectonic emplacement of the ophiolites and terrane paleogeography in the Hellenides. 104, 262–280.
- Papanikolaou, D., Barghathi, H., Dabovski, C., Dimitriu, T., El-Hawat, A., Ioane, D., Kranis, H., Obeidi, A., Oaie, C., Seghedi, A., Zagorchev, I., 2004. TRANSMED Transect VII: East European Craton - Scythian Platform – Dobrogea – Balkanides – Rhodope Massif – Hellenides – East Mediterranean – Cyrenaica, in: Cavazza, W., Roure, F., Spakman, W., Stampfli, G., Ziegler, P. (Eds.), The TRANSMED Atlas: The Mediterranean Region from Crust to Mantle. Springer–Verlag, Berlin.
- Papp, M., 2007. Geology and kinematics of detachment faulting on NE Paros Island in Greece. Unpublished diploma thesis. ETH Zurich.
- Pe-Piper, G., Piper, D.J.W., 2002. The igneous rocks of Greece: The anatomy of an orogen, Gebrüder Borntraeger, Berlin, Germany.
- Putlitz, B., Cosca, M.A., Schumacher, J.C., 2005. Prograde mica  $^{40}\text{Ar}/^{39}\text{Ar}$  growth ages recorded in high pressure rocks (Syros, Cyclades, Greece). Chemical Geology. 214, 79–98.

- Robert, E., 1982. Contribution a l'étude géologique des Cyclades (Grèce): L'Ile de Paros. Unpublished thesis. Université de Paris-Sud.
- Royden, L.H., 1993. Evolution of retreating subduction boundaries formed during continental collision. *Tectonics*. 12, 629–638.
- Sanchez-Gomez, M., Avigad, D., Heimann, A., 2002. Geochronology of clasts in allochthonous Miocene sedimentary sequence on Mykonos and Paros Islands: implications for backarc extension in the Aegean Sea. *Journal of the Geological Society London*. 159, 45–60.
- Seward, D., Vanderhaeghe, O., Siebenaller, L., Thomson, S., Hibsich, C., Zingg, A., Holzner, P., Ring, U., Duchêne, S., 2009. Cenozoic tectonic evolution of Naxos Island through a multi-faceted approach of fission-track analysis. *Geological Society of London Special Publications*. 321, 179–196.
- Stockli, D.F., 2005. Application of low-temperature thermochronometry to extensional tectonic settings, in: Reiners, P.W., Ehlers, T.A. (Eds.), *Low-Temperature Thermochronology: Techniques, Interpretations, and Applications*. *Reviews in Mineralogy and Geochemistry*. 58, 441–448.
- Reiners, P.W., 2005. Zircon (U-Th)/He Thermochronometry, in: Reiners, P.W., Ehlers, T.A. (Eds.), *Low-Temperature Thermochronology: Techniques, Interpretations, and Applications*. *Reviews in Mineralogy and Geochemistry*. 58, 441–448.

- Ring, U., Layer, P.W., 2003. High-pressure metamorphism in the Aegean, eastern Mediterranean: underplating and exhumation from the Late Cretaceous until the Miocene to Recent above the retreating Hellenic subduction zone. *Tectonics*. 22, doi:10.1029/2001TC001350.
- Ring, U., Glodny, J., Will, T., Thomson, S., 2010. The Hellenic subduction system: high-pressure metamorphism, exhumation, normal faulting, and large-scale extension. *Annual Review of Earth and Planetary Sciences*. 38, 45–76.
- Taymaz, T., Jackson, J., McKenzie, D., 1991. Active tectonics of the north and central Aegean Sea. *Geophys. J. Int.* 106, 433–490.
- Thomson, S.N., Stöckhert, B., Brix, M.R., 1999. Miocene high-pressure metamorphic rocks of Crete, Greece: rapid exhumation by buoyant escape. *Geological Society of London Special Publications*. 154, 87–107.
- Tomaschek, F., Kennedy, A.K., Villa, I.M., Lagos, M., Ballhaus C., 2003. Zircons from Syros, Cyclades, Greece: recrystallization and mobilization of zircon during high-pressure metamorphism. *Journal of Petrology*. 44, 1977–2002.
- Veermesch, P., 2005. How many grains are needed for a provenance study?. *Earth and Planetary Science Letters*. 224, 441–451.
- Wijbrans, J.R., McDougall, I., 1986.  $^{40}\text{Ar}/^{39}\text{Ar}$  dating of white micas from an Alpine high-pressure metamorphic belt on Naxos (Greece): the resetting of the argon isotopic system. *Contributions to Mineralogy and Petrology*. 93, 187–194.

Wijbrans, J.R., McDougall, I., 1988. Metamorphic evolution of the Attic Cycladic metamorphic belt on Naxos (Cyclades, Greece) utilizing  $^{40}\text{Ar}/^{39}\text{Ar}$  age spectrum measurements. *Journal of Metamorphic Geology*. 6, 571–594.



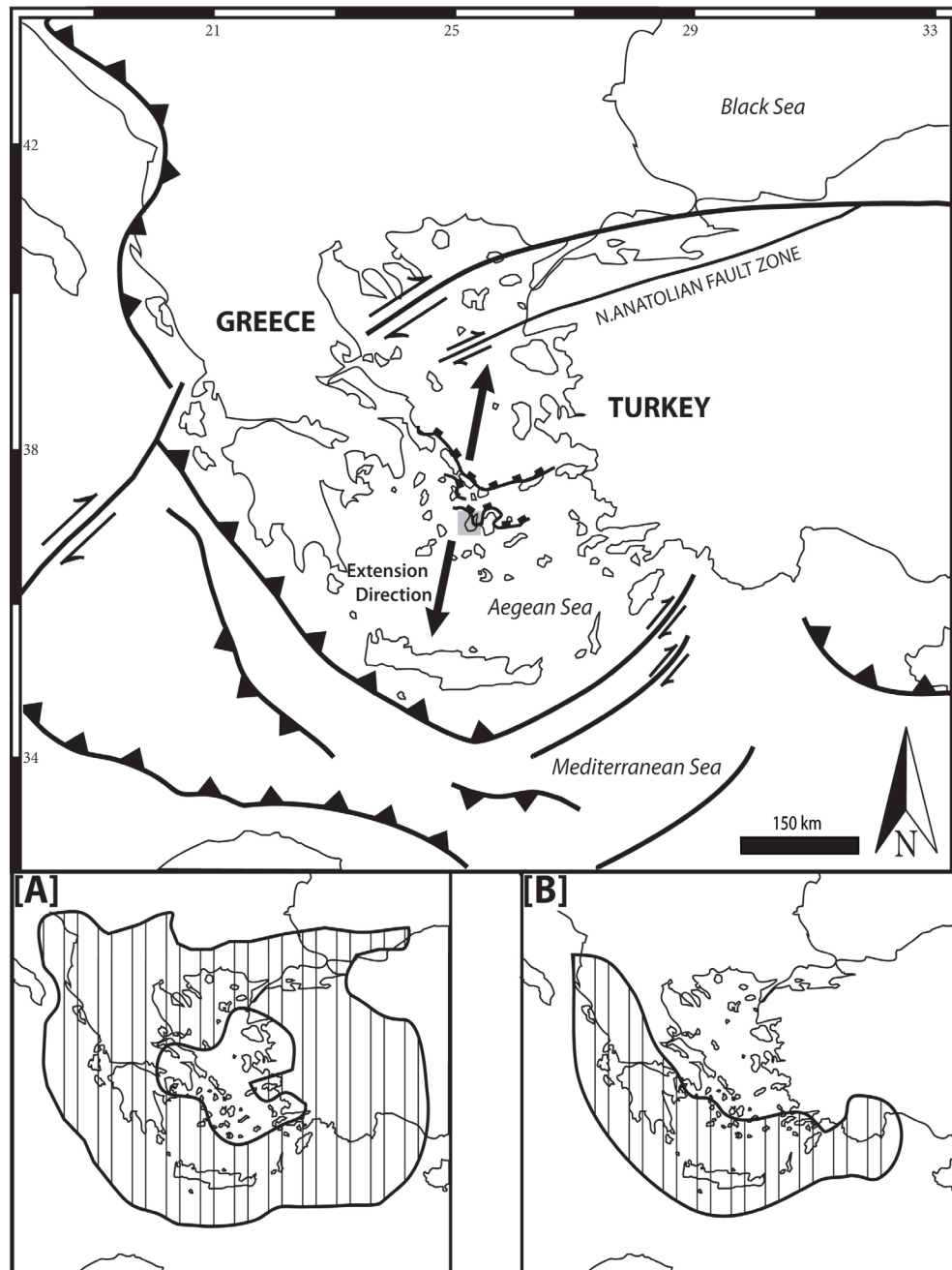


**Figure 1.** Simplified regional structure map for the greater Aegean region. Structures after Jolivet and others (2010). The dominant regional feature is the Hellenic subduction zone, which comprises several trenches separated by the Mediterranean Accretionary Complex. The current tectonic configuration has resulted from the long-term southward retreat of the subduction zone. This retreat caused widespread backarc extension manifested by the low-angle extensional detachment systems in the central Aegean. The North Anatolian Fault zone is a more recent structure related to Arabian plate indentation to the east. Black arrows indicate the average regional extension direction. The island of Paros is highlighted by the shaded box. [A] Hatched area shows the distribution of active earthquakes in the greater Aegean region occurring from 0 -35 km depth and  $\geq$  magnitude 4. Note that the central Aegean is currently aseismic (see discussion in text). [B] Hatched area shows the distribution of active earthquakes in the greater Aegean region occurring from 35 - 300 km depth and  $\geq$  magnitude 4. Earthquakes deepen northward toward the limit of seismicity related to the downgoing African slab. (All earthquake data from USGS).

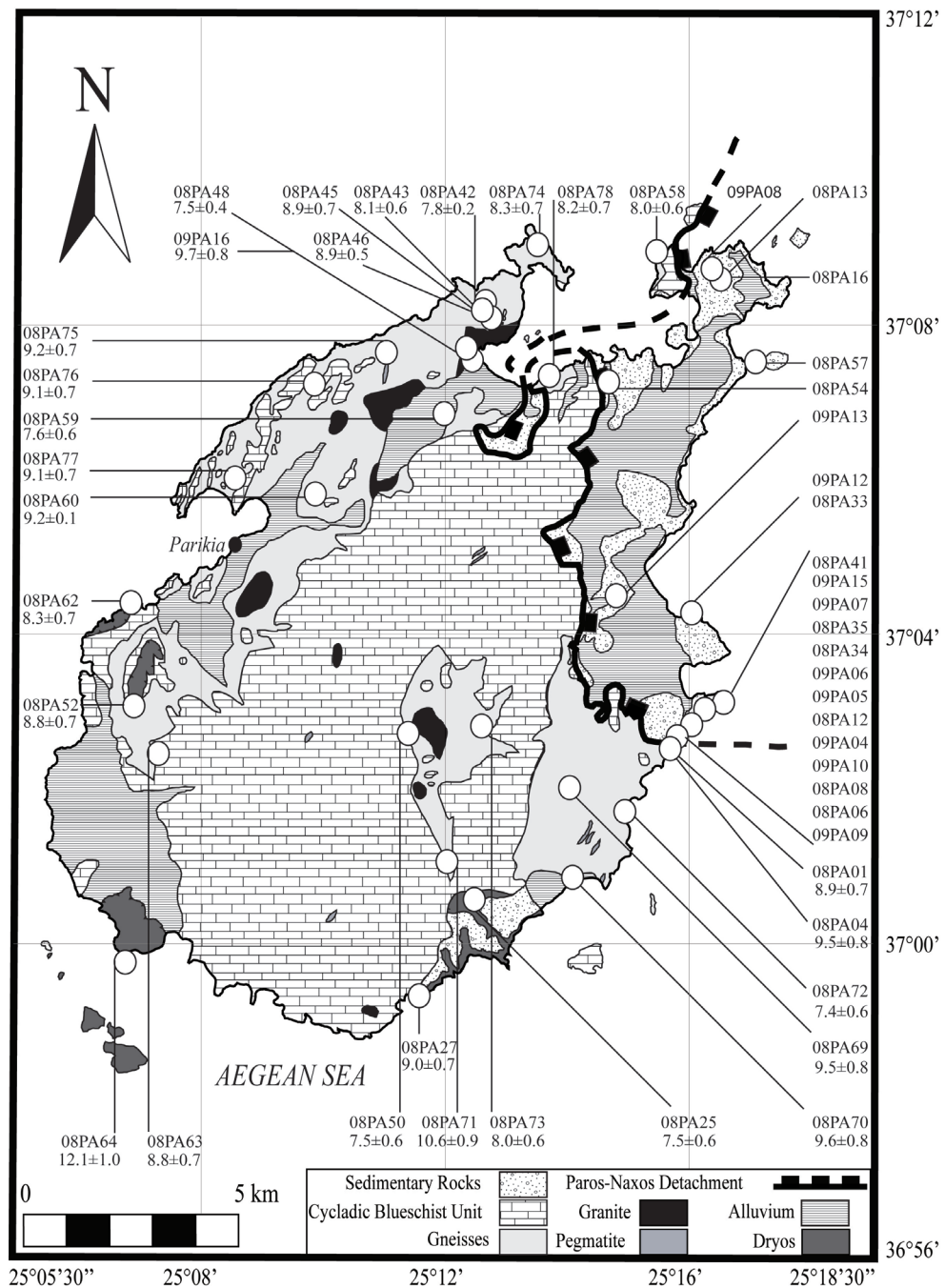


**Figure 2.** Simplified geologic map of Paros (after Papanikolaou, 1996). The dominant structural feature is the Paros-Naxos low-angle extensional detachment fault which separates the supradetachment basin from the metamorphic core complex. (U-Th)/He sample locations are shown by white circles, which may encompass more than one sample location. Sample names are connected to their corresponding locations with lines. Ages beneath sample names are mean zircon (U-Th)/He ages with mean  $2\sigma$  error. See text for unit descriptions and tables for apatite (U-Th)/He and zircon U-Pb results.

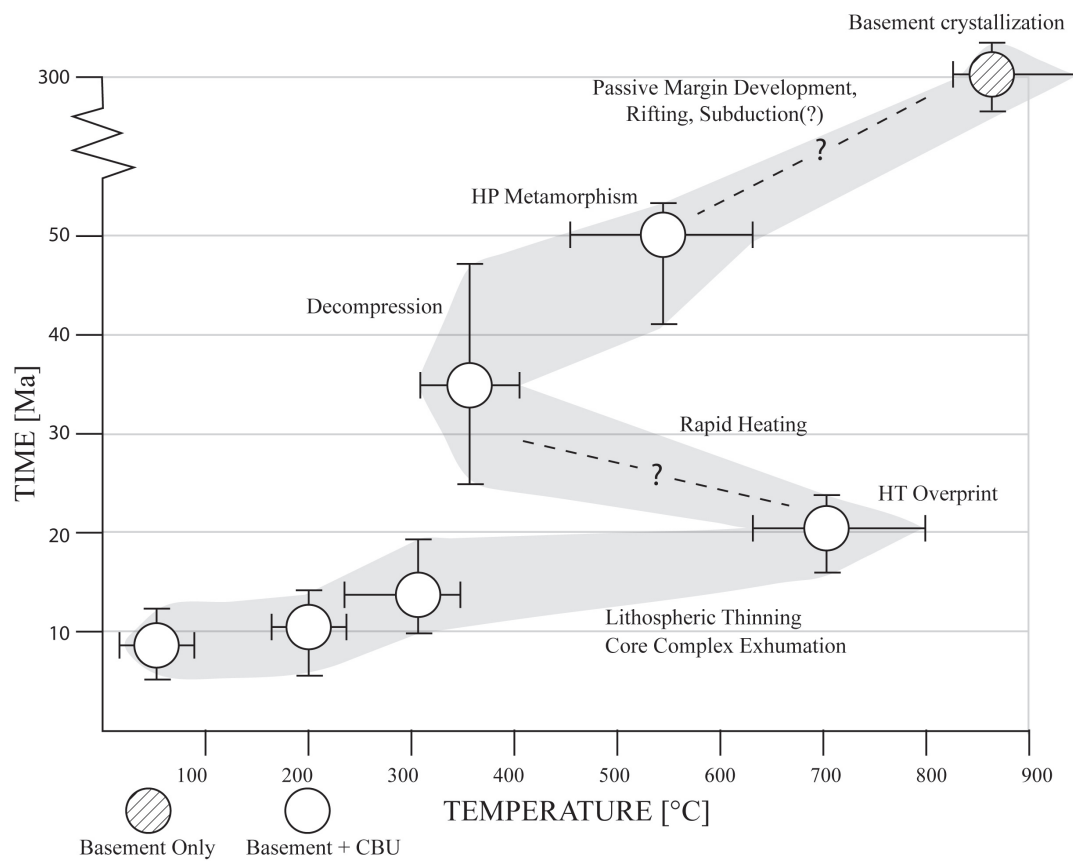


**Figure 3.** Generalized thermal history for Paros based on geo- and thermochronometry and petrographic studies from Paros and Naxos. The time-temperature path is outlined in gray using error bars to obtain magnitudes. Note that error bars themselves are estimates based on the studies from which the time and temperature derived. Carboniferous basement crystallization from zircon U-Pb ages on the footwall gneisses (Engel and Reischmann, 1998; this study). Little work has been done on the Late Paleozoic to Early Tertiary, so a break in the y-axis reflects the lack of conclusive evidence about the thermal history during this time period. Peak HP metamorphism from petrography (Avigad, 1998) and geo- and thermochronometry (Wijbrans and McDougall, 1986; Bröcker and Enders, 1999; Tomaschek et al., 2003; Putlitz et al., 2005). Decompression from petrography (Avigad, 1998). High-temperature overprint from ion microprobe U-Pb ages on zircon rims (Keay et al., 2001) and petrography (Buick and Holland, 1989). Final cooling path based on thermochronometry of footwall rocks (Altherr et al., 1982; Brichau et al., 2006; this study) and geochronometry of volcanic rocks (this study). See full discussion of events in text.

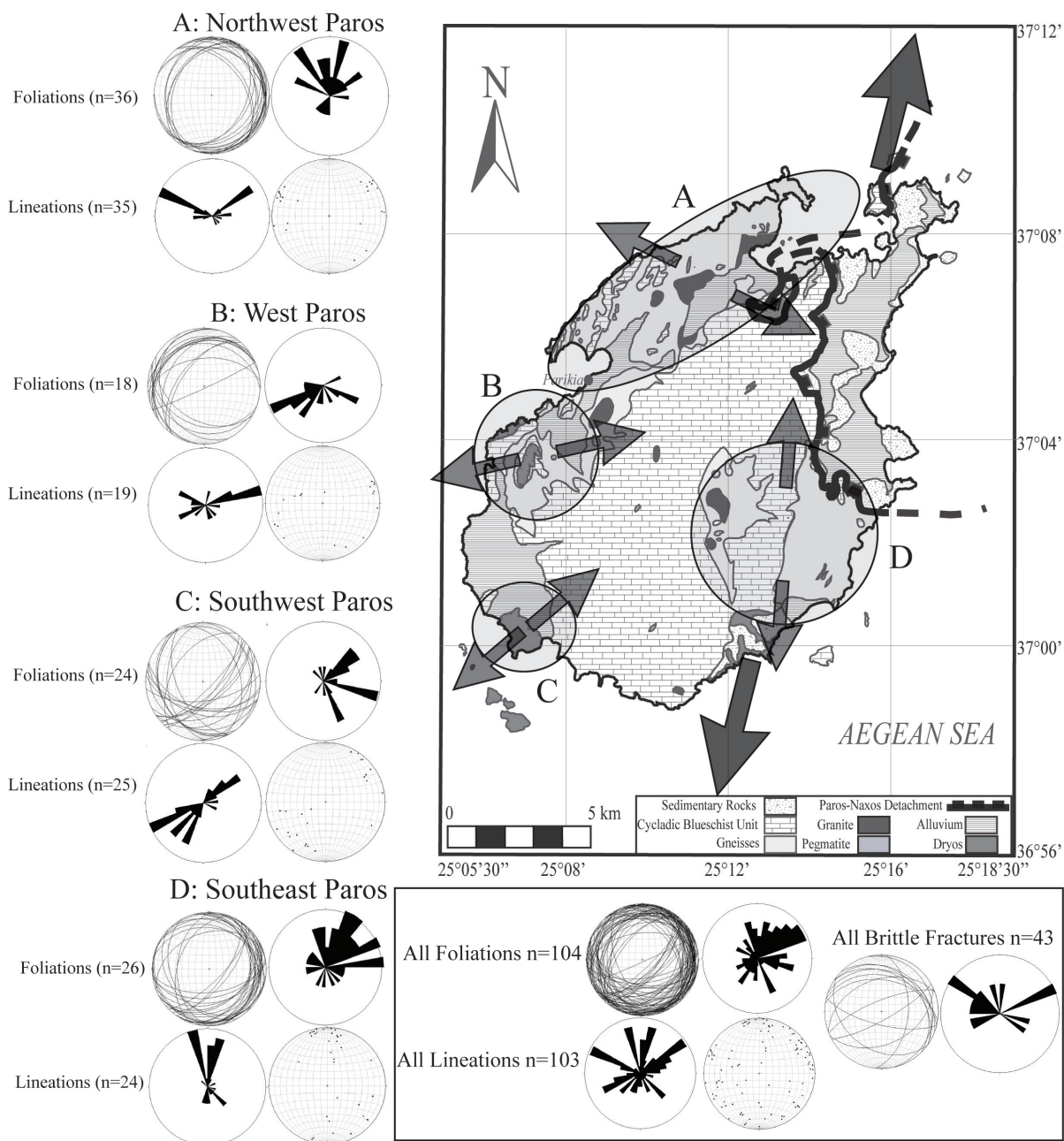


**Figure 4.** Results from structural characterization of the Paros footwall (basemap after Papanikolaou, 1996). All diagrams shown are equal area lower hemisphere projections created with Stereonet software (Allmendinger, 1986). For foliations, great circles and rose diagrams of the dip directions of the planes are shown. For lineations, rose diagrams with plotted trends are shown as well as the corresponding equal area projections with lines. Because the stretching lineation and foliation curve across the island, measurements are separated into four discrete sectors which have their own distinct structural signature. Each zone is shaded in gray and exhibits arrows which show the average trend indicated therein. Measurements of ductile fabrics were taken on footwall gneisses and marbles, while brittle fractures encompass those observed in hanging wall rocks, as well. The overall direction of extension is approximately NNE and is shown by the largest black arrows. Brittle fractures encompass those measured in the hanging wall, as well.



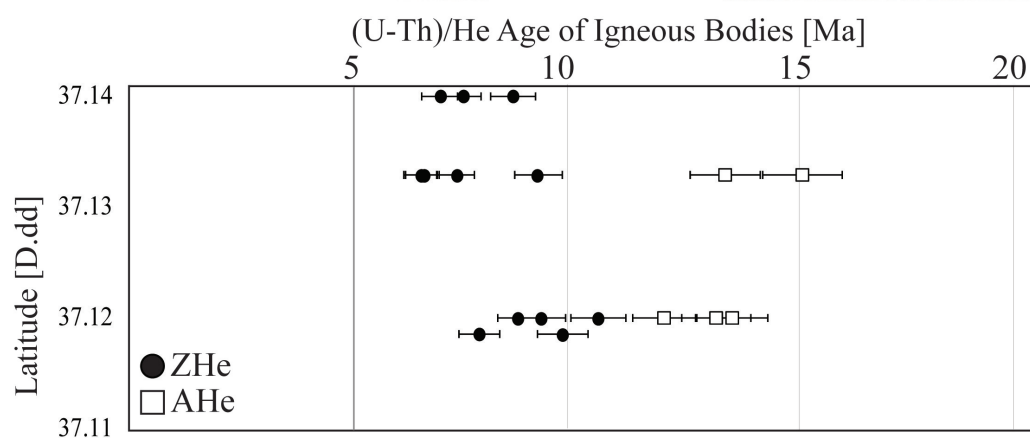
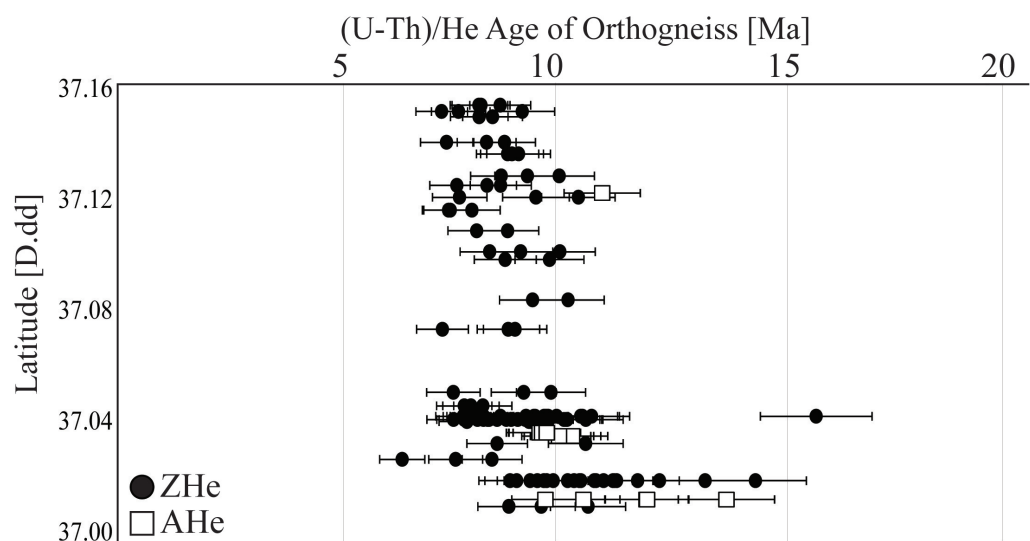


**Figure 5.** (U-Th)/He results from footwall orthogneisses and igneous intrusives. Graphs plot AHe and ZHe against latitude, which is useful proxy for horizontal distance to the detachment, since the location of the detachment north of the island is not well-constrained (see Figure 2). The upper plot shows results from footwall gneisses. The AHe and ZHe are the same age and invariant against latitude, indicating exceptionally fast cooling (i.e.,  $>100$  °C/Ma). The lower plot shows results from igneous bodies which have intruded the orthogneiss. Since individual bodies intruded at a given time, no trend was expected. The samples are, from top to bottom, 08PA42, a rhyolite dike; 08PA48, an S-type granite; 09PA16, a biotite granite; and 08PA46, an aplite. [A] A pegmatite body from northeastern Paros showing a weakly developed stretching lineation, seen by elongated tourmaline grains. This lineation indicates that intrusion was syn-extensional. Mechanical pencil eraser for scale. Location: N 37.150, E 25.262. [B] Stair-stepping  $\sigma$ -type porphyroclast in an orthogneiss exhibiting top to the northeast sense of shear. One euro coin for scale. Location: N 37.132, E 25.214. [C] Parasitic folding in amphibolite schists of the upper footwall. One euro coin for scale. Location: N 39.992, E 25.219 (D.ddd). [D] Panorama of orthogneiss outcrop in northwestern Paros. Aplitic body on left of picture is sample location for 08PA46. There appear to be multiple generations of syn-extensional leucocratic intrusions - some crosscut the foliation and some are foliation parallel. Hammer in lower left is ~30 cm tall.

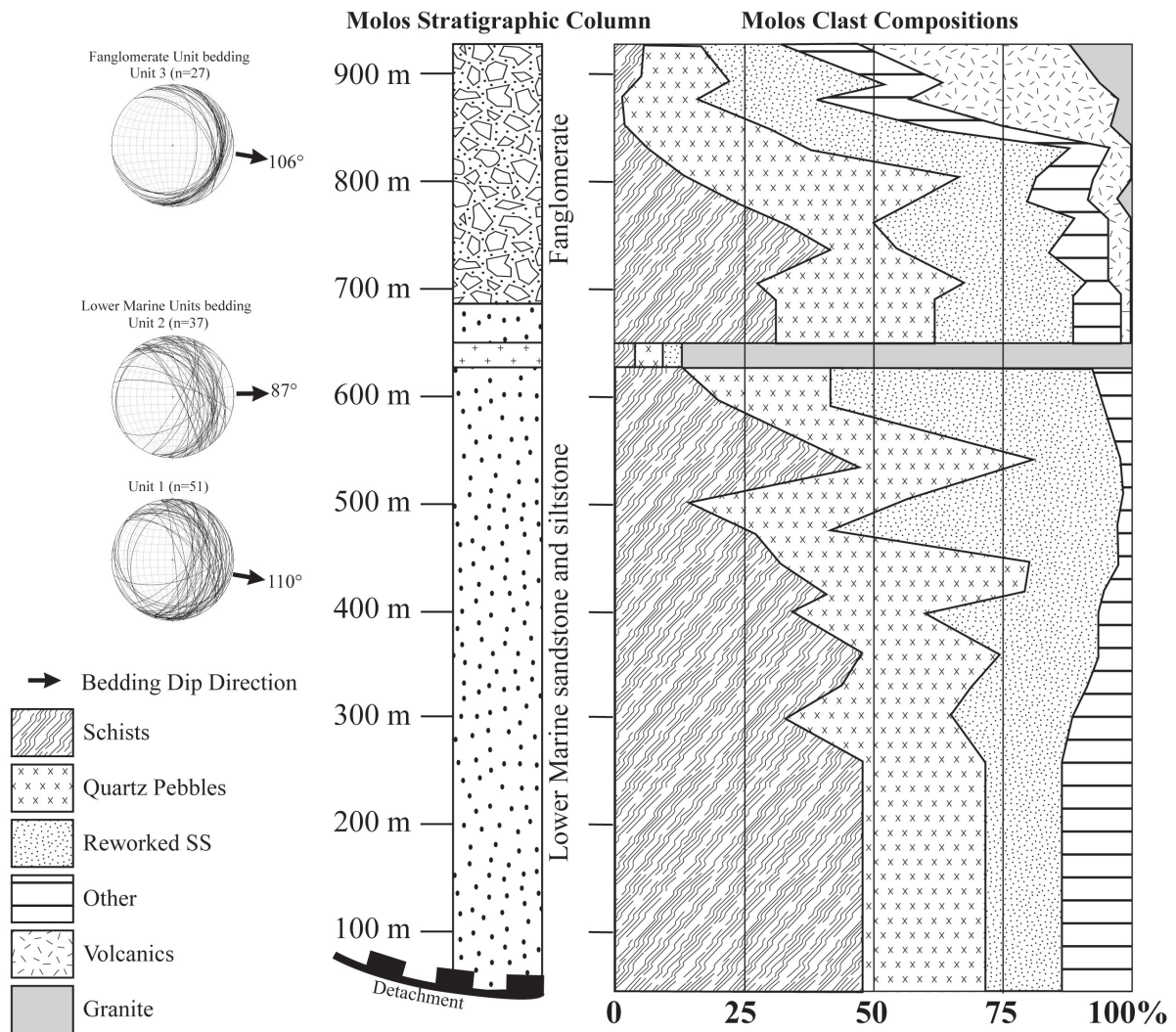
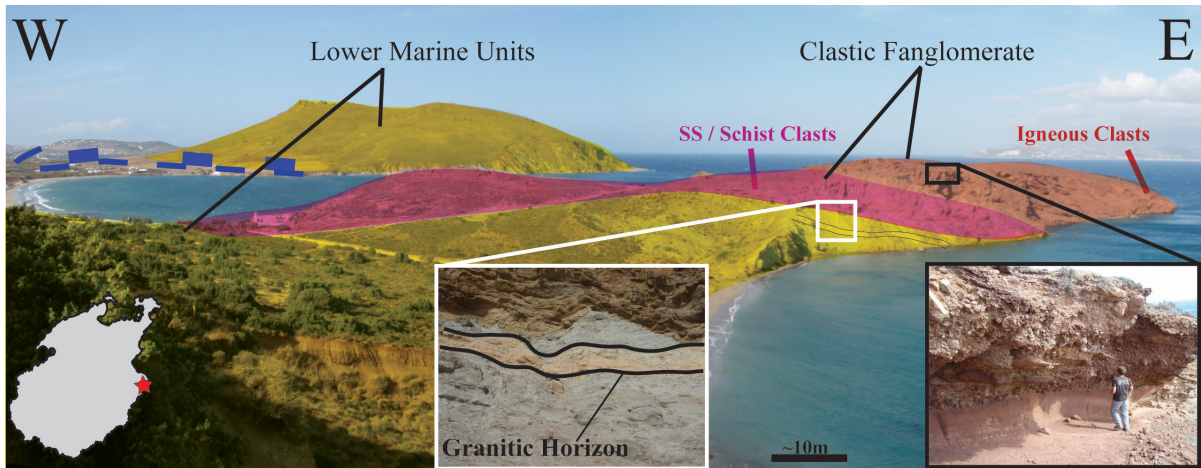


**Figure 6.** Results of stratigraphic analysis on the exposed sedimentary section at Molos Bay. Panoramic field shot shows the stratigraphic and structural interpretation of the section. Contacts between sedimentary units are shown as depositional, but may be erosional in nature. Zoom boxes show the granitic horizon (~2 m thick) and a representative outcrop of the fan-glomerate bedding regime (person for scale). Bedding is shown in an equal area lower hemisphere projection with great circles plotted for the planes. The black arrow shows the average of bedding dip directions. The stereonet diagrams are shown alongside a cartoon stratigraphic column and a clast composition frequency plot. The stratigraphic column is a simplified representation which shows lithology, stratigraphic position and vertical distance upsection from the detachment. The clast composition frequency plot shows the frequency distribution of clast types upsection. The five main clast types observed were schist, quartz exudate, reworked sandstone (SS), rhyolite and granite. Counts were always  $n > 100$  for clasts  $> 2$  cm in diameter. Counts were combined for areas of similar stratigraphic position in the same section.



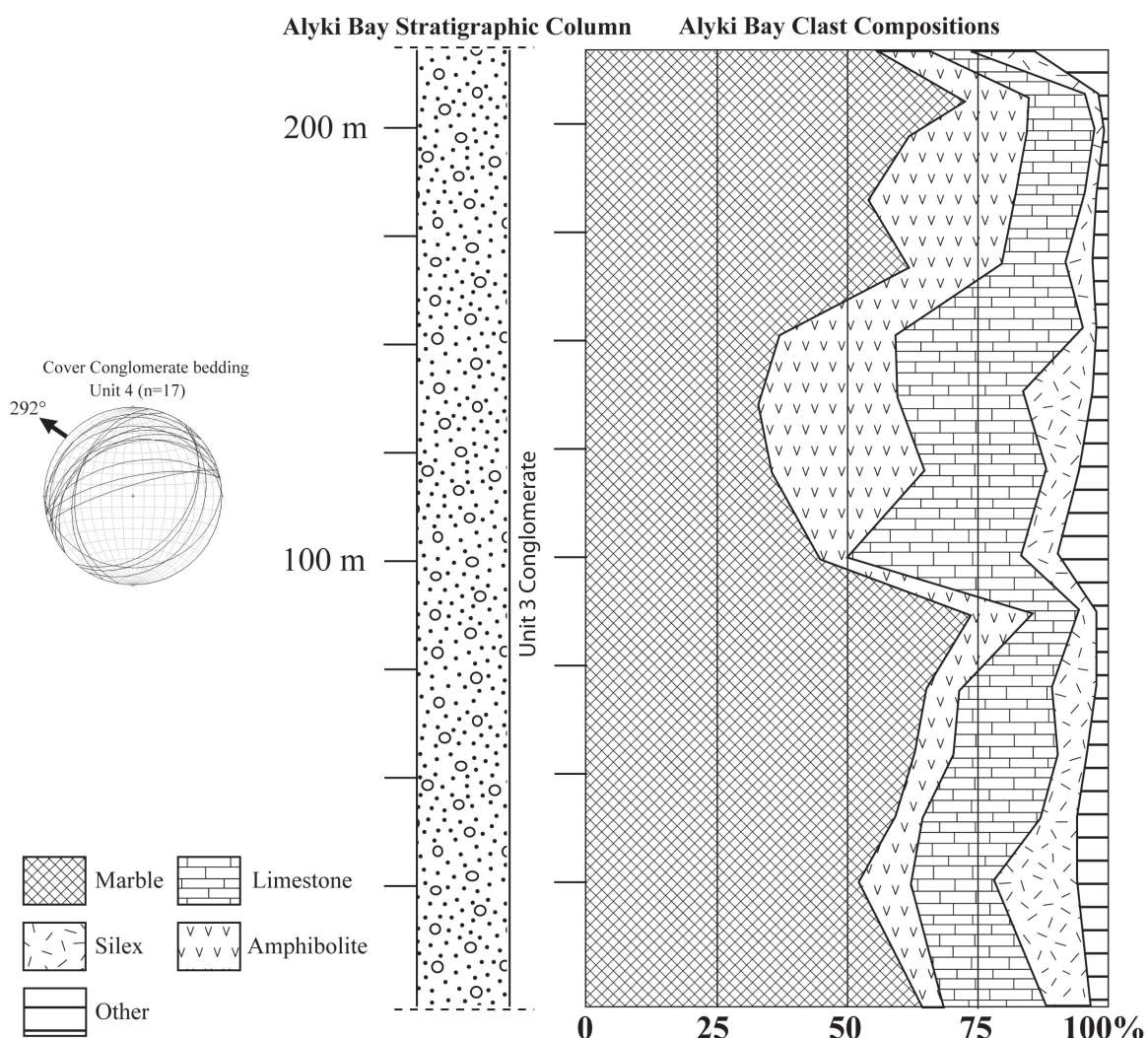
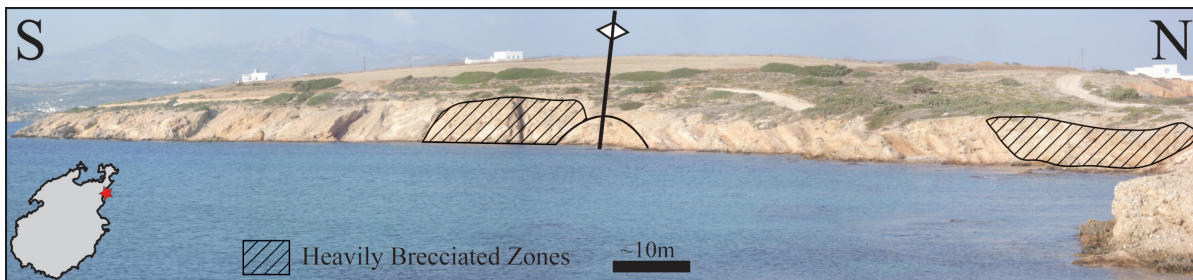


**Figure 7.** Results of stratigraphic analysis on the exposed sedimentary section at Alyki Bay. Panoramic field shot shows the stratigraphic and structural interpretation of the section. Hatched zones are heavily brecciated areas, which are important for temporally constraining deformation. Since the outcrop is folded into a central anticline, folding has to occur before brecciation. Bedding is shown in an equal area lower hemisphere projection with great circles plotted for the planes. The black arrow shows the average of bedding dip direction. Bedding appears to dip in opposite direction due to an anticline in the section. The stereonet diagram is shown alongside a cartoon stratigraphic column and a clast composition frequency plot. The stratigraphic column is a simplified representation which shows the lithology of the single unit and provides context for the clast compositions. The clast composition frequency plot shows the frequency distribution of clast types upsection. The four main clasts observed were marble, limestone, siliceous limestone and amphibolite.

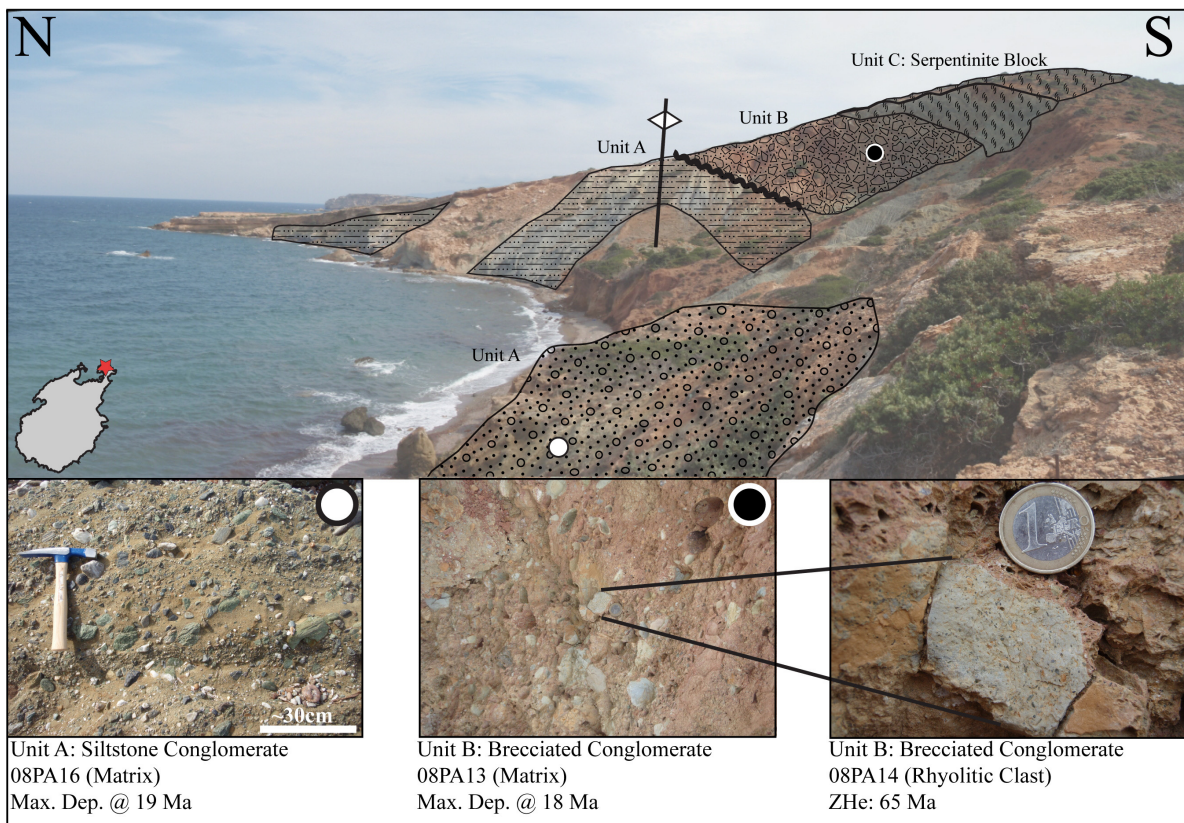


**Figure 8.** Results of stratigraphic analysis on the exposed sedimentary section near the settlement of Santa Maria. Panoramic field shot shows the stratigraphic and structural interpretation of the section. Units are overlain by transparencies of their corresponding lithologic patterns (unit A: silty sandstone with conglomeratic layers and lenses; unit B: brecciated conglomerate). The central anticline of the outcrop is traced and labeled. Two different star polygons highlight key sample locations which provide useful thermochronometric information. Bedding is highly disrupted in this outcrop and was not measured. Clast compositions were not performed because the matrix obscured the identification of clast types. The white circle with black outline shows the sample location for 08PA16, the sandy matrix of unit A. The sample yields a ZHe maximum depositional age of ~19 Ma. The close-up field photo shows the clast types, which are all  $\leq 10$  cm. The black circle with white outline shows the sample location for 08PA13, the sandy matrix of unit B. The sample yields a ZHe maximum depositional age of ~18 Ma. The close-up field photo also shows the location of 08PA14, a rhyolitic clast found in the matrix which yields a ZHe age of ~65 Ma.



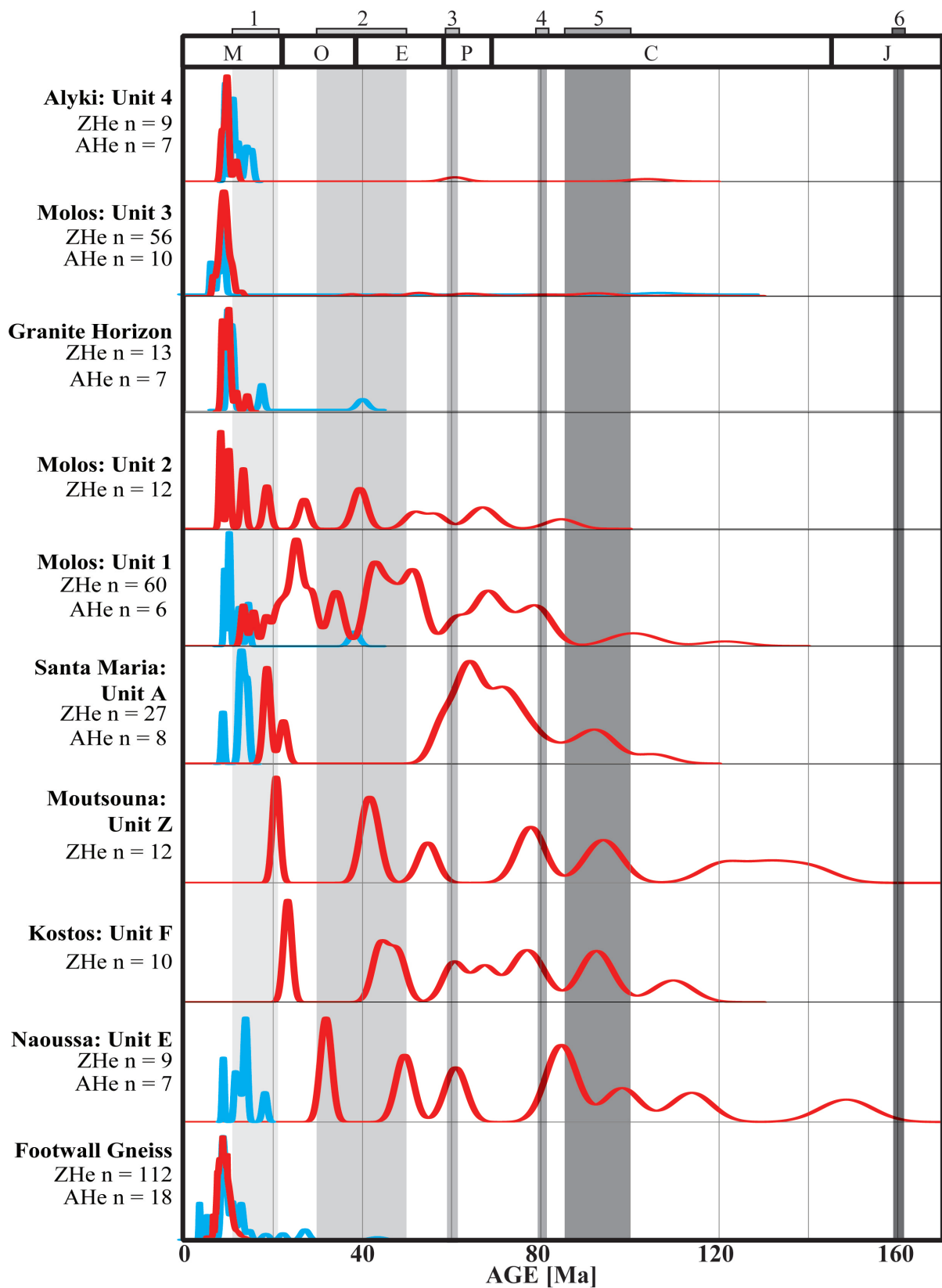


**Figure 9.** Stacked probability density plots showing the results of both crystalline and detrital zircon and apatite (U-Th)/He thermochronometry. Results from the footwall are shown at the bottom for comparison. The y-axis is relative probability and the x-axis is age. The red lines represent ZHe analyses and the blue lines represent AHe. The plots are stacked from oldest to youngest ZHe maximum depositional age and are labeled with the sample location and unit. Note that from the granite horizon upwards the hanging wall detrital signature is indistinguishable from the footwall crystalline signature. Downsection from the granite horizon, various tectonometamorphic signals are present. The signals recorded by these events are taken from 1: Zircon (U-Th)/He ages on footwall rocks from Paros (this study, Brichau et al., 2006) and U-Pb ages on metamorphic zircon overgrowth (Keay et al., 2001); 2: White mica  $^{40}\text{Ar}/^{39}\text{Ar}$  and zircon U-Pb on HP, LT rocks of Syros (Tomaschek et al., 2003; Putlitz et al., 2005); 3: Zircon U-Pb ages on eclogite facies rocks from the island of Tinos (Bröcker and Enders, 1999); 4: Zircon U-Pb ages on eclogite facies rocks from Syros (Bröcker and Enders, 1999); 5: Muscovite  $^{40}\text{Ar}/^{39}\text{Ar}$  ages on HP deformational fabrics from the Pelagonian Zone in the NW Aegean (Lips et al., 1999); 6: Zircon U-Pb ages on HP mélange blocks from the island of Andros (Bröcker and Pidgeon, 2007). It is likely that some ZHe partial retention zones from these discrete events are recorded in the data. See text for full discussion and interpretation.

# Molos Section

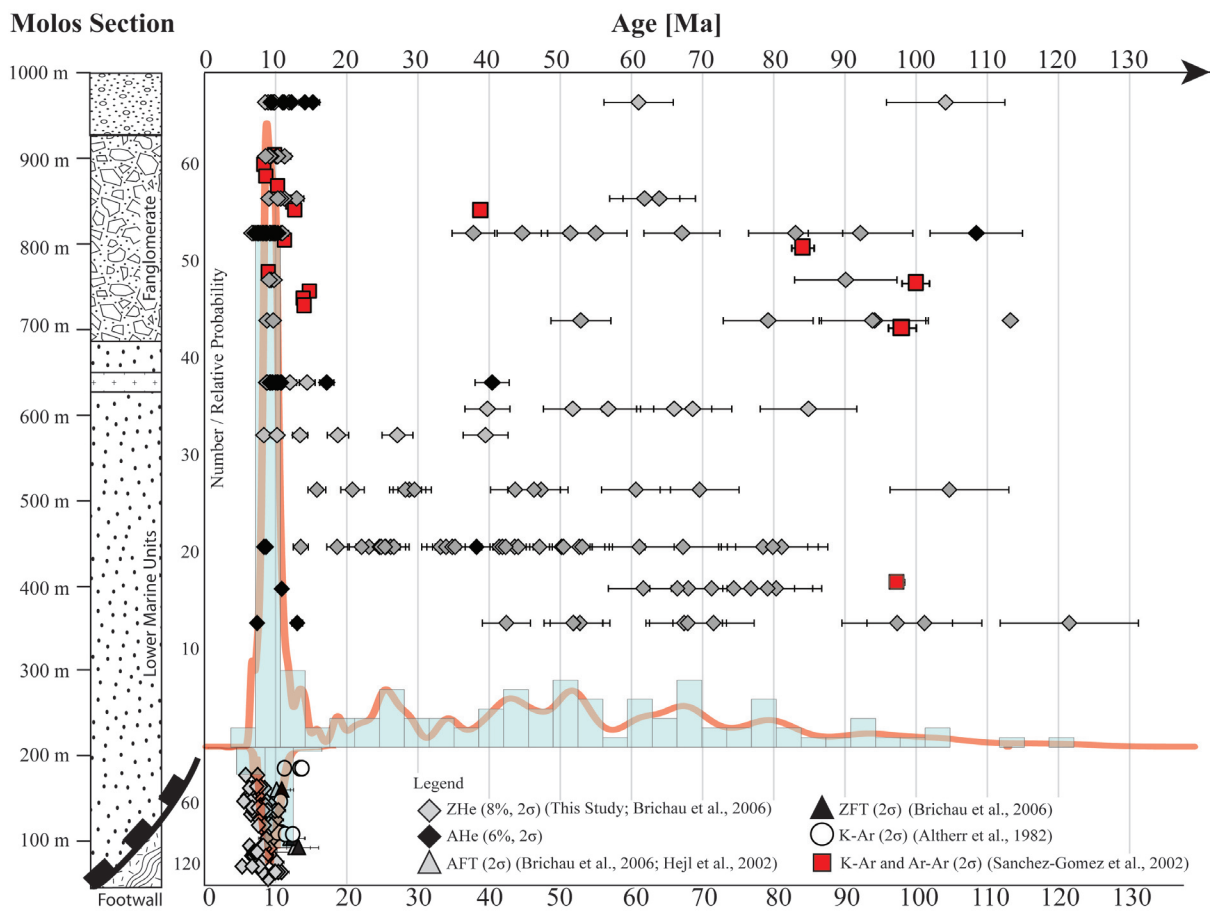


**Figure 10.** Results of detrital thermochronometry on the sections at Molos and Alyki Bay. Here we presume Alyki Bay unit 4 deposits overly unit 3 at Molos Bay (see discussion in text). The plot shows published ZHe, zircon fission-track and apatite fission-track by Brichau and others (2006), apatite fission-track from Hejl and others (2003), hornblende, tourmaline, muscovite and biotite  $^{40}\text{K}/^{39}\text{Ar}$  from Altherr and others (1982) on the footwall rocks of Paros. The plot also shows published detrital white mica  $^{40}\text{Ar}/^{39}\text{Ar}$  and whole-rock  $^{40}\text{K}/^{39}\text{Ar}$  on young volcanic clasts (Sanchez-Gomez et al., 2002). The published data are contrasted with the (U-Th)/He results of this study. The stratigraphic column is “peeled” back to reveal footwall signatures for comparison. All errors are reported to  $2\sigma$ . Relative probability plots are shown in the background with histograms, which show exact quantities of each given population of ZHe ages in the footwall and hanging wall. Probability density plots are only shown for ZHe ages only and do not include other thermochronometric techniques.

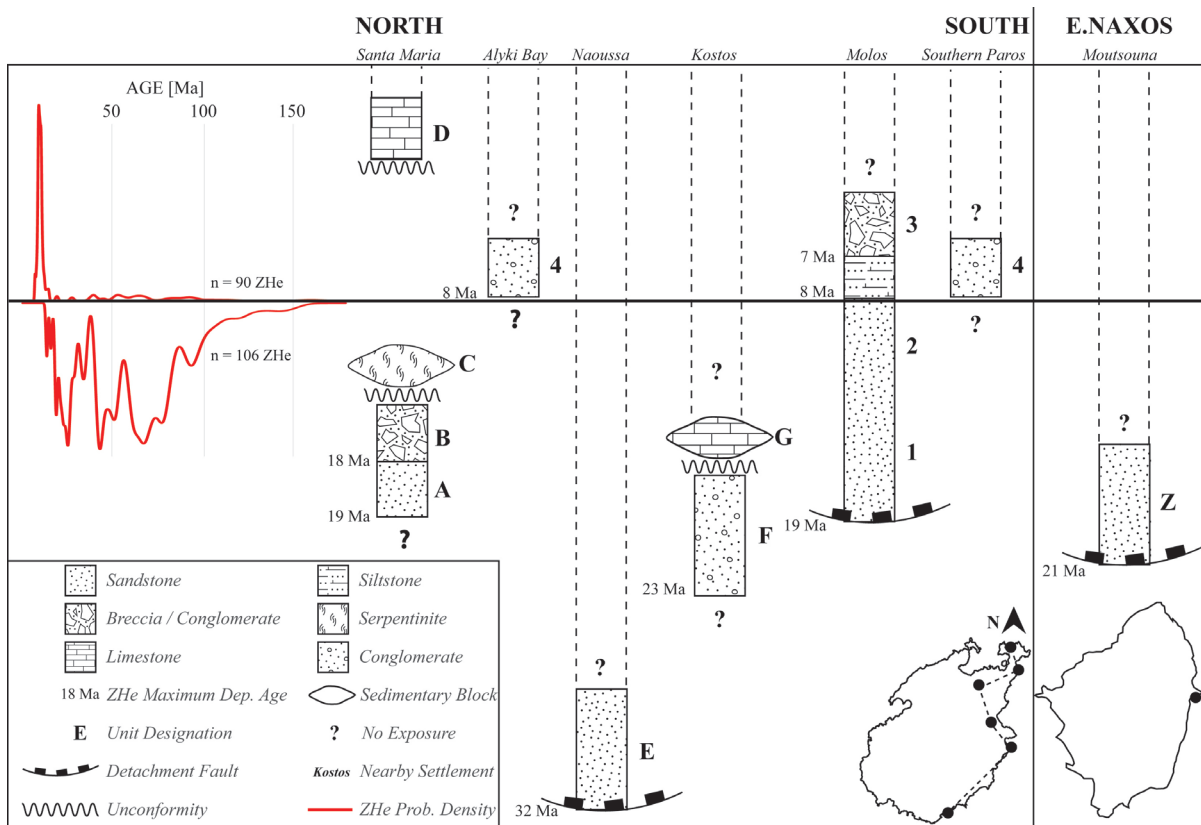


**Figure 11.** Stratigraphic correlation for sedimentary outcrops on the island of Paros. Probability density plots for ZHe data are included to show late-stage footwall input into the basin. Outcrops are organized from North to South, locations are given as black dots on the map in the lower right. The vertical axis represents approximate time, shown to give the reader a qualitative idea of depositional timing. Each location has the present units stacked underneath it with the proper unit names used in the text. Unit thicknesses are not true thicknesses and there is no vertical scale other than time. Lense-shaped units are considered to be olistoliths. Where it is not known if a unit contact is depositional or erosional, an unconformity is utilized. Where stratigraphic context is entirely unknown, a question mark is used. In some cases, the sedimentary rocks are in contact with the Paros-Naxos detachment fault and this is illustrated in the figure. Where known, the ZHe maximum depositional age is given near the base of the unit and is the primary basis for this correlation (complete results are shown in Figure 9). Dashed lines are included to indicate that the ZHe age is a maximum age, although deposition could be significantly younger. See discussion in text for full interpretation.

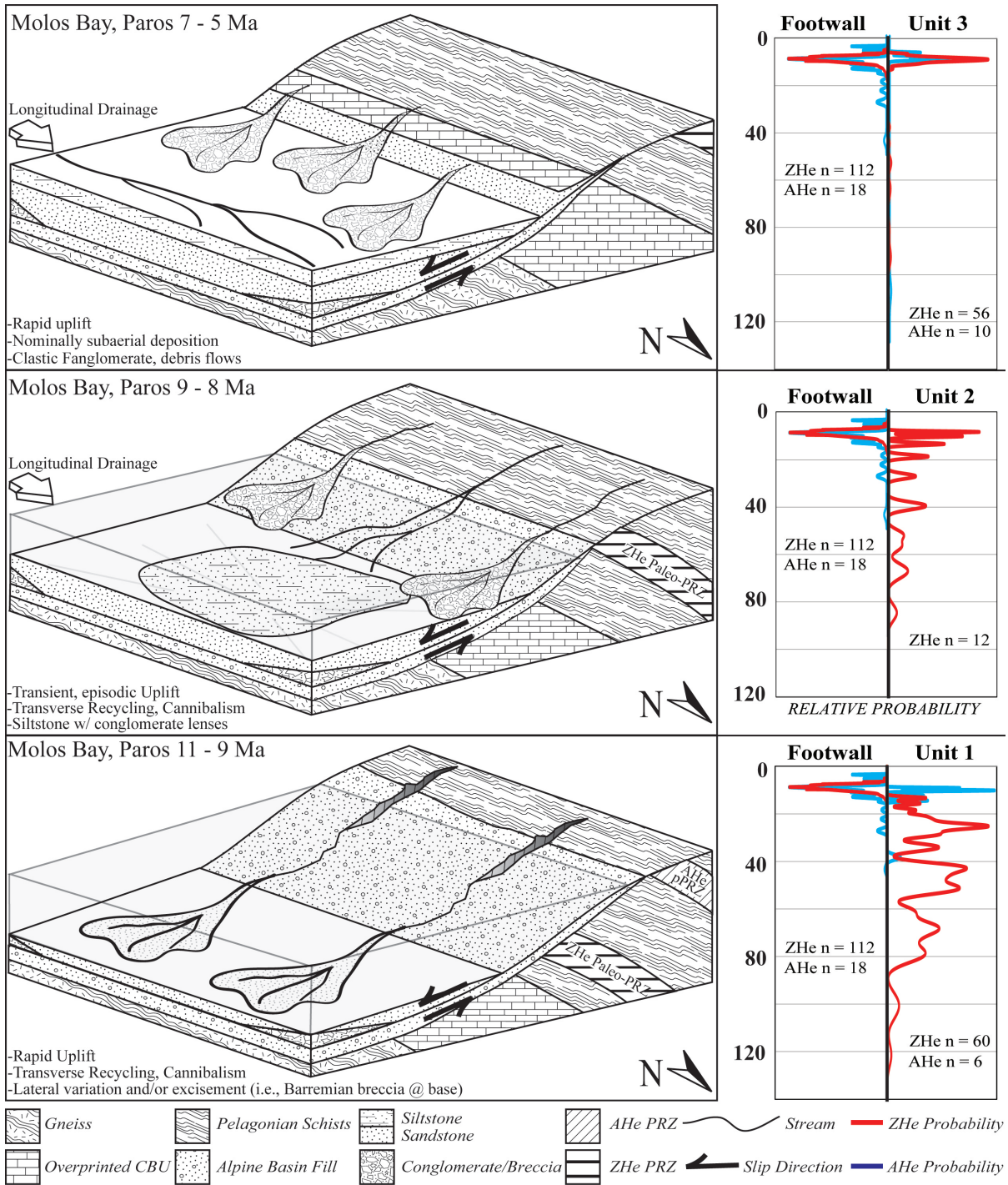


**Figure 12.** Tectonosedimentary evolution of the Paros supradetachment basin (inspired by Friedmann and Burbank, 1995). Block diagrams schematically illustrate the depositional style and timing of sedimentation at Molos Bay. The diagrams also show the relative position of the AHe and ZHe paleo-partial retention zones. The block diagrams are shown side by side with probability density plots comparing the detrital thermochronometric signatures with the crystalline signature from the footwall rocks. The upper diagram shows the deposition of unit 1 in a submarine fan in the Middle Miocene. The detrital signatures from unit 1 record the multi-stage tectonometamorphic history of the overlying, undifferentiated Pelagonian units. The middle diagram shows the deposition of unit 2 in a low-energy, shallow marine environment with some alluvial development creating conglomeratic lenses in the Late Miocene. The detrital signatures from unit 2 preserve diminished pre-extensional signals and exhibit the appearance of locally derived and reset footwall detritus. The lower diagram shows the deposition of unit 3 in an alluvial fan environment in the Late Miocene. The detrital signatures from unit 3 are indistinguishable from the local footwall signature and contain uniformly reset AHe and ZHe ages.



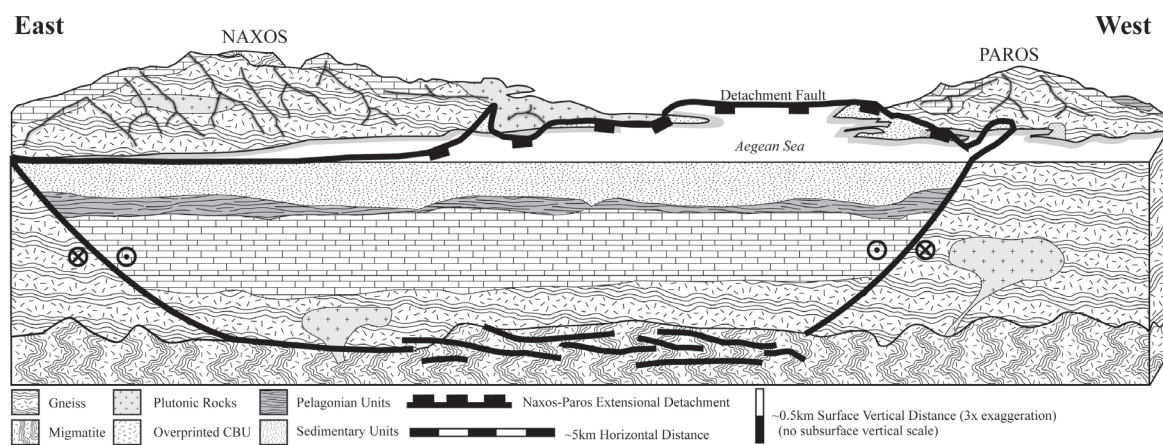


**Figure 13.** Current three-dimensional structural configuration of Paros and Naxos islands based on rocks and structures currently exposed at the surface. There is no vertical scale. The main feature is the Paros-Naxos low-angle extensional detachment fault, which juxtaposes the supradetachment basin deposits against the exhumed metamorphic complexes. See text for full description of lithotectonic units and structures. Figure 12 shows the Middle Miocene to present tectonosedimentary evolution which result in this present configuration.

08PA43	Measured Ratios		Corrected Ratios			Apparent Ages		
	206/238	207/206	206/238	207/235	207/206	206/238	207/235	2σ [Ma]
	[Ma]	[Ma]	[Ma]	[Ma]	[Ma]	[Ma]	[Ma]	2σ [Ma]
	0.05524	0.05498	0.48289	0.06962	0.05031	433.9	400.1	42.8
	0.03855	0.06954	0.45262	0.04876	0.06733	306.9	379.1	13.7
	0.03500	0.06215	0.34857	0.04411	0.05732	278.2	303.6	43.2
	0.03705	0.05782	0.32873	0.04658	0.05119	293.5	288.6	51.8
	0.06055	0.11206	1.15466	0.07643	0.10956	474.8	779.4	72.1
	0.03940	0.05411	0.36094	0.04972	0.05265	312.8	312.9	7.6
	0.03377	0.06713	0.35003	0.04232	0.05732	267.2	304.7	41.7
	0.04059	0.05377	0.36725	0.05107	0.05119	321.1	317.6	10.3
	0.04754	0.05941	0.47454	0.05981	0.10956	374.5	394.3	20.2
	0.03870	0.05458	0.35331	0.04831	0.05265	304.2	307.2	3.8
	0.03987	0.05451	0.36187	0.04977	0.05732	313.1	313.6	5.8
	0.03960	0.06007	0.39240	0.04974	0.05119	312.9	336.1	11.6
	0.03416	0.04208	0.21149	0.04271	0.10956	269.6	194.8	183.1
	0.04042	0.05273	0.35239	0.05079	0.05265	319.4	306.5	16.9
	0.03938	0.05570	0.36758	0.04952	0.05732	311.6	317.9	7.5
	0.03941	0.05419	0.35925	0.04932	0.05119	310.3	311.7	7.1
	0.03885	0.05378	0.35210	0.04862	0.10956	306.1	306.3	5.5
	0.03914	0.05512	0.36337	0.04899	0.05265	308.3	314.7	6.5
	0.03492	0.05993	0.31328	0.04283	0.05732	270.3	276.7	48.5
	0.03787	0.05410	0.34058	0.04678	0.05119	294.7	297.6	4.3
	0.04007	0.05498	0.36504	0.04948	0.10956	311.3	316.0	7.0
	0.04024	0.05351	0.35206	0.04953	0.05265	311.6	306.3	7.2
	0.03803	0.05296	0.33428	0.04685	0.05732	295.2	292.8	10.0
	0.03866	0.05406	0.34592	0.04757	0.05119	299.6	301.6	3.9
	0.04203	0.06713	0.46773	0.05172	0.10956	325.0	389.6	29.2

Measured Ratios	Corrected Ratios				Apparent Ages	
	206/238	207/206	206/238	207/235	207/238 [Ma]	207/235 2 $\sigma$ [Ma]
08PA42	0.04339	0.05429	0.39003	0.05339	335.3	334.4 6.4
	0.03889	0.05468	0.35126	0.04784	301.3	305.7 4.0
	0.34476	0.15591	8.88890	0.42446	2280.7	2326.7 41.7
	0.04023	0.05794	0.37886	0.04948	311.3	326.2 19.6
	0.07285	0.06171	0.74109	0.08969	553.7	563.0 11.4
	0.06356	0.05888	0.61793	0.07826	485.7	488.5 9.9
	0.04065	0.05453	0.36787	0.05008	315.0	318.1 4.8
	0.04010	0.05588	0.36395	0.04917	309.4	315.2 10.1
	0.03931	0.05337	0.34731	0.04826	303.8	302.7 4.7
	0.05083	0.05963	0.46985	0.06212	388.5	391.1 50.7
	0.00107	0.11254	0.01614	0.00128	8.2	16.3 4.5
	0.00101	0.05434	0.00799	0.00122	7.9	8.1 1.8
	0.00104	0.09291	0.01392	0.00125	8.0	14.0 8.4
	0.00106	0.05408	0.00789	0.00128	8.2	8.0 2.6
	0.03648	0.05748	0.33697	0.04434	279.7	294.9 18.9
	0.00097	0.06250	0.00941	0.00118	7.6	9.5 1.9
	0.00108	0.05848	0.00844	0.00130	8.4	8.5 2.2
	0.00094	0.07798	0.01071	0.00113	7.3	10.8 2.6
	0.00097	0.04788	0.00617	0.00117	7.5	6.2 3.2
	0.00100	0.05106	0.00734	0.00121	7.8	7.4 1.3
	0.00098	0.07146	0.01014	0.00118	7.6	10.2 2.3
	0.00095	0.05402	0.00759	0.00115	7.4	7.7 3.2
	0.03390	0.05595	0.30865	0.04117	260.1	273.1 7.4
	0.02107	0.05206	0.17834	0.02559	162.9	166.6 13.3

Measured Ratios	Corrected Ratios			Apparent Ages	207/235	
	206/238	207/206	206/238		206/238 [Ma]	2σ [Ma]
0.00094	0.04548	0.00610	0.00113	7.3	6.2	2.4
0.00101	0.03974	0.00575	0.00122	7.9	5.8	1.8
0.03820	0.05456	0.33969	0.04639	292.4	296.9	5.9
0.04055	0.05357	0.35384	0.04925	309.9	307.6	10.4
0.00097	0.05919	0.00847	0.00117	7.5	8.6	2.3
0.00095	0.04485	0.00597	0.00115	7.4	6.0	5.1
0.00109	0.05852	0.00893	0.00131	8.4	9.0	1.4
0.03950	0.05444	0.34924	0.04804	302.4	304.1	7.1
0.05433	0.05606	0.49168	0.06604	412.3	406.1	19.7
0.03745	0.05401	0.32782	0.04549	286.8	287.9	7.1

**Table 1.** U-Pb data collected at the University of Arizona. Isotope ratios were measured on a multi-collector ICP-MS. Measured and corrected isotope ratios are given, along with apparent ages.

Sample	Rock Type	Latitude [D.ddd]	Longitude [D.ddd]	Age [Ma]	$\pm 2\sigma$ (8%) [My]	U [ppm]	Th [ppm]	eU [ppm]	Th/U	He [nmol/g]	Mass [ $\mu$ g]	Ft
z08PA01-1	Gneiss	37.0388	25.2613	8.3	0.7	312.8	70.0	328.9	0.2	11.67	7.40	0.79
z08PA01-2	Gneiss	37.0388	25.2613	7.8	0.6	168.8	66.9	184.2	0.4	6.17	8.40	0.79
z08PA01-3	Gneiss	37.0388	25.2613	7.5	0.6	400.0	72.1	416.6	0.2	13.31	6.90	0.79
z08PA01-4	Gneiss	37.0388	25.2613	9.1	0.7	224.7	64.2	239.5	0.3	9.07	6.72	0.77
z08PA01-5	Gneiss	37.0388	25.2613	8.1	0.6	271.8	69.5	287.8	0.3	10.13	12.43	0.81
z08PA01-6	Gneiss	37.0388	25.2613	9.1	0.7	250.9	79.1	269.2	0.3	10.51	9.66	0.79
z08PA01-7	Gneiss	37.0388	25.2613	20.9	1.7	539.4	74.4	556.5	0.1	52.45	16.08	0.83
z08PA01-8	Gneiss	37.0388	25.2613	7.8	0.6	606.9	105.0	631.1	0.2	19.56	4.75	0.74
z08PA01-9 <sup>1</sup>	Gneiss	37.0388	25.2613	15.7	1.3	161.8	45.1	172.2	0.3	14.59	1.06	1.00
z08PA01-10 <sup>1</sup>	Gneiss	37.0388	25.2613	9.8	0.8	205.8	124.0	234.4	0.6	12.41	0.66	1.00
z08PA01-11 <sup>1</sup>	Gneiss	37.0388	25.2613	12.2	1.0	95.6	27.6	101.9	0.3	6.72	1.32	1.00
z08PA01-13 <sup>2</sup>	Gneiss	37.0388	25.2613	9.0	0.7	416.5	133.3	447.2	0.3	13.88	2.22	0.64
z08PA01-14 <sup>2</sup>	Gneiss	37.0388	25.2613	10.0	0.8	245.8	66.7	261.1	0.3	11.07	8.86	0.78
z08PA01-15 <sup>2</sup>	Gneiss	37.0388	25.2613	8.3	0.7	731.2	74.1	748.3	0.1	24.26	3.66	0.72
z08PA01-16 <sup>2</sup>	Gneiss	37.0388	25.2613	8.7	0.7	700.6	126.0	729.6	0.2	25.29	5.22	0.74
z08PA01-17 <sup>2</sup>	Gneiss	37.0388	25.2613	9.2	0.7	285.9	61.2	300.0	0.2	11.68	8.66	0.79
z08PA01-18 <sup>2</sup>	Gneiss	37.0388	25.2613	10.1	0.8	666.5	133.9	697.3	0.2	30.11	9.59	0.79
z08PA01-19 <sup>2</sup>	Gneiss	37.0388	25.2613	9.2	0.7	472.8	55.0	485.5	0.1	19.02	8.69	0.79
z08PA01-20 <sup>2</sup>	Gneiss	37.0388	25.2613	8.2	0.7	364.6	90.7	385.5	0.2	13.28	8.01	0.78
z08PA01-21 <sup>2</sup>	Gneiss	37.0388	25.2613	10.0	0.8	193.1	59.4	206.8	0.3	8.68	8.04	0.78
z08PA01-22 <sup>2</sup>	Gneiss	37.0388	25.2613	9.5	0.8	163.3	70.4	179.5	0.4	7.35	11.91	0.80
z08PA01-23 <sup>2</sup>	Gneiss	37.0388	25.2613	10.5	0.8	240.1	109.8	265.4	0.5	11.68	9.09	0.78
z08PA01-24 <sup>2</sup>	Gneiss	37.0388	25.2613	8.5	0.7	1082.4	152.1	1117.4	0.1	38.31	5.37	0.75
z08PA01-25 <sup>2</sup>	Gneiss	37.0388	25.2613	8.8	0.7	219.8	59.7	233.6	0.3	8.64	8.29	0.78
z08PA01-26 <sup>2</sup>	Gneiss	37.0388	25.2613	9.3	0.7	756.5	170.2	795.7	0.2	32.12	11.43	0.81
z08PA01-27 <sup>2</sup>	Gneiss	37.0388	25.2613	9.7	0.8	461.8	77.6	479.7	0.2	20.51	14.71	0.82

Sample	Rock Type	Latitude [D.dddd]	Longitude [D.dddd]	Age [Ma]	$\pm 2\sigma$ (8%) [My]	U [ppm]	Th [ppm]	eU [ppm]	Th/U	He [nmol/g]	Mass [ $\mu$ g]	Ft
z08PA04-1	Gneiss	37.0400	25.2628	7.7	0.6	433.5	77.4	451.3	0.2	14.82	7.40	0.79
z08PA04-2	Gneiss	37.0400	25.2628	9.2	0.7	437.4	178.1	478.4	0.4	17.70	4.70	0.75
z08PA04-3	Gneiss	37.0400	25.2628	9.4	0.7	274.7	108.8	299.8	0.4	11.63	5.90	0.77
z08PA04-4	Gneiss	37.0400	25.2628	10.4	0.8	418.2	170.0	457.4	0.4	18.93	6.18	0.74
z08PA04-5	Gneiss	37.0400	25.2628	7.9	0.6	470.7	49.9	482.2	0.1	15.84	7.07	0.77
z08PA04-6	Gneiss	37.0400	25.2628	9.6	0.8	283.0	45.5	293.5	0.2	11.67	6.59	0.77
z08PA04-7	Gneiss	37.0400	25.2628	10.4	0.8	180.4	26.7	186.6	0.1	8.16	11.46	0.78
z08PA04-8	Gneiss	37.0400	25.2628	9.7	0.8	305.2	112.2	331.1	0.4	13.39	8.09	0.78
z08PA04-9	Gneiss	37.0400	25.2628	10.6	0.9	137.0	41.0	146.4	0.3	6.91	18.98	0.82
z08PA04-10	Gneiss	37.0400	25.2628	8.2	0.7	356.0	34.4	363.9	0.1	12.73	8.81	0.79
z08PA04-11	Gneiss	37.0400	25.2628	8.1	0.6	522.8	32.6	530.3	0.1	17.97	7.55	0.78
z08PA04-12	Gneiss	37.0400	25.2628	9.6	0.8	893.1	197.7	938.6	0.2	35.36	5.03	0.73
z08PA04-13	Gneiss	37.0400	25.2628	9.3	0.7	642.8	122.9	671.1	0.2	24.74	4.77	0.73
z08PA04-14	Gneiss	37.0400	25.2628	15.7	1.3	87.5	42.6	97.3	0.5	6.71	14.28	0.81
z08PA04-15	Gneiss	37.0400	25.2628	8.0	0.6	332.2	45.2	342.6	0.1	11.72	11.27	0.79
z08PA04-16	Gneiss	37.0400	25.2628	9.6	0.8	418.6	130.7	448.6	0.3	17.78	6.75	0.77
z08PA04-17	Gneiss	37.0400	25.2628	9.8	0.8	729.8	154.2	765.3	0.2	31.51	8.48	0.78
z08PA04-18	Gneiss	37.0400	25.2628	8.6	0.7	714.9	138.0	746.7	0.2	25.43	5.66	0.74
z08PA42-1	Rhyolite	37.1389	25.2113	7.0	0.6	893.0	689.6	1051.7	0.8	31.37	6.90	0.79
z08PA42-2	Rhyolite	37.1389	25.2113	7.5	0.6	1581.0	1304.4	1881.3	0.8	55.31	3.00	0.72
z08PA42-3	Rhyolite	37.1389	25.2113	8.7	0.7	1321.1	1062.2	1565.7	0.8	52.98	2.90	0.72
z08PA43-1	Gneiss	37.1388	25.2112	8.7	0.7	640.2	72.1	656.9	0.1	23.16	4.70	0.75
z08PA43-2	Gneiss	37.1388	25.2112	8.3	0.7	203.4	122.2	231.6	0.6	8.39	9.90	0.81
z08PA43-3	Gneiss	37.1388	25.2112	7.4	0.6	348.9	66.7	364.3	0.2	11.51	9.10	0.80
z08PA45-1	Gneiss	37.1347	25.2034	9.0	0.7	270.0	65.3	285.0	0.2	10.83	6.70	0.78
z08PA45-2	Gneiss	37.1347	25.2034	8.8	0.7	517.4	78.4	535.4	0.2	19.53	5.50	0.77



Sample	Rock Type	Latitude [D.dddd]	Longitude [D.dddd]	Age [Ma]	$\pm 2\sigma$ (8%) [My]	U [ppm]	Th [ppm]	eU [ppm]	Th/U	He [nmol/g]	Mass [ $\mu$ g]	Ft
z08PA45-3	Gneiss	37.1347	25.2034	8.7	0.7	444.8	66.1	460.0	0.1	17.39	9.20	0.80
z08PA46-1	Aplite	37.1183	25.2031	9.9	0.8	2484.4	289.2	2551.0	0.1	106.47	6.90	0.78
z08PA46-2	Aplite	37.1183	25.2031	7.9	0.6	2086.5	238.0	2141.3	0.1	71.30	6.70	0.78
z08PA48-1	Granite	37.1321	25.2138	9.3	0.7	1627.8	148.3	1662.0	0.1	67.92	12.90	0.81
z08PA48-2	Granite	37.1321	25.2138	7.4	0.6	1397.8	164.0	1435.6	0.1	45.00	7.80	0.79
z08PA48-3	Granite	37.1321	25.2138	6.6	0.5	1305.8	119.9	1333.4	0.1	36.51	5.50	0.77
z08PA48-4	Granite	37.1321	25.2138	6.6	0.5	1071.8	117.6	1098.9	0.1	30.91	7.50	0.79
z08PA50-1	Amphibolite	37.0404	25.1903	6.8	0.5	13.6	12.9	16.6	1.0	0.48	7.40	0.79
z08PA50-2	Amphibolite	37.0404	25.1903	8.2	0.7	28.9	42.1	38.6	1.5	1.42	12.60	0.82
z08PA52-1	Gneiss	37.0486	25.1187	9.7	0.8	259.0	37.3	267.6	0.1	10.61	5.10	0.76
z08PA52-2	Gneiss	37.0486	25.1187	9.1	0.7	748.1	86.1	767.9	0.1	29.36	6.30	0.78
z08PA52-3	Gneiss	37.0486	25.1187	7.5	0.6	602.2	82.7	621.3	0.1	19.19	5.00	0.76
z08PA58-1	Gneiss	37.1500	25.2623	9.1	0.7	330.6	82.3	349.5	0.2	13.71	8.80	0.80
z08PA58-2	Gneiss	37.1500	25.2623	7.6	0.6	293.0	47.9	304.0	0.2	9.19	3.10	0.73
z08PA58-3	Gneiss	37.1500	25.2623	7.3	0.6	406.0	39.8	415.1	0.1	13.77	19.40	0.85
z08PA59-1	Gneiss	37.1144	25.2012	7.9	0.6	922.6	58.9	936.1	0.1	31.57	7.90	0.79
z08PA59-2	Gneiss	37.1144	25.2012	7.5	0.6	274.0	40.7	283.4	0.1	8.76	6.20	0.77
z08PA59-3	Gneiss	37.1144	25.2012	7.4	0.6	1502.3	113.2	1528.3	0.1	45.67	4.60	0.75
z08PA60-2	Gneiss	37.0965	25.1672	9.7	0.8	458.9	138.5	490.8	0.3	18.98	3.60	0.74
z08PA60-3	Gneiss	37.0965	25.1672	8.7	0.7	306.0	90.1	326.8	0.3	12.19	9.40	0.80
z08PA62-1	Gneiss	37.0714	25.1200	7.3	0.6	478.8	69.2	494.7	0.1	14.13	3.20	0.73
z08PA62-2	Gneiss	37.0714	25.1200	8.8	0.7	62.0	14.8	65.4	0.2	2.24	3.00	0.72
z08PA62-3	Gneiss	37.0714	25.1200	8.9	0.7	312.3	153.1	347.5	0.5	11.68	2.30	0.70
z08PA63-1	Gneiss	37.0381	25.1242	9.3	0.7	589.2	119.0	616.6	0.2	24.81	10.00	0.81
z08PA63-2	Gneiss	37.0381	25.1242	7.8	0.6	735.6	59.6	749.3	0.1	25.38	8.40	0.80
z08PA63-3	Gneiss	37.0381	25.1242	9.2	0.7	589.7	46.1	600.3	0.1	24.15	8.60	0.81

Sample	Rock Type	Latitude [D.dddd]	Longitude [D.dddd]	Age [Ma]	$\pm 2\sigma$ (8%) [My]	U [ppm]	Th [ppm]	eU [ppm]	Th/U	He [nmol/g]	Mass [ $\mu$ g]	Ft
z08PA66-2	Gneiss	37.1069	25.1809	8.7	0.7	243.0	20.3	247.7	0.1	9.60	12.40	0.82
z08PA66-3	Gneiss	37.1069	25.1809	8.0	0.6	829.9	187.0	873.0	0.2	29.95	7.60	0.79
z08PA69-1	Gneiss	37.0302	25.2338	8.5	0.7	127.3	23.5	132.7	0.2	5.13	19.40	0.84
z08PA69-2	Gneiss	37.0302	25.2338	10.5	0.8	227.1	48.1	238.1	0.2	11.08	14.80	0.82
z08PA70-1	Gneiss	37.0074	25.2338	10.5	0.8	708.2	47.1	719.1	0.1	33.76	13.40	0.83
z08PA70-2	Gneiss	37.0074	25.2338	8.8	0.7	582.3	29.5	589.1	0.1	23.27	15.70	0.84
z08PA70-3	Gneiss	37.0074	25.2338	9.5	0.8	729.6	42.6	739.4	0.1	29.16	5.40	0.77
z08PA71-2	Gneiss	37.0168	25.2013	8.9	0.7	348.1	60.4	362.0	0.2	13.67	7.40	0.78
z08PA71-3	Gneiss	37.0168	25.2013	8.8	0.7	374.3	71.4	390.8	0.2	15.14	11.40	0.82
z08PA71-4	Gneiss	37.0168	25.2013	11.1	0.9	1261.6	239.2	1316.6	0.2	61.91	8.11	0.78
z08PA71-5	Gneiss	37.0168	25.2013	10.7	0.9	685.4	104.3	709.4	0.2	29.18	3.09	0.71
z08PA71-6	Gneiss	37.0168	25.2013	10.2	0.8	459.8	45.1	470.2	0.1	20.35	8.01	0.78
z08PA71-7	Gneiss	37.0168	25.2013	10.4	0.8	233.6	34.0	241.4	0.1	10.37	6.74	0.77
z08PA71-8	Gneiss	37.0168	25.2013	10.4	0.8	651.1	79.5	669.4	0.1	27.96	4.77	0.75
z08PA71-9	Gneiss	37.0168	25.2013	9.6	0.8	272.3	37.4	280.9	0.1	11.84	13.01	0.81
z08PA71-10	Gneiss	37.0168	25.2013	9.4	0.8	217.8	49.4	229.1	0.2	9.21	9.31	0.79
z08PA71-11	Gneiss	37.0168	25.2013	10.9	0.9	464.6	64.3	479.4	0.1	22.16	8.77	0.79
z08PA71-12	Gneiss	37.0168	25.2013	10.7	0.9	1357.1	97.6	1379.6	0.1	60.93	6.17	0.77
z08PA71-13	Gneiss	37.0168	25.2013	11.2	0.9	776.7	152.9	811.9	0.2	38.85	9.14	0.79
z08PA71-14	Gneiss	37.0168	25.2013	12.2	1.0	503.9	106.0	528.2	0.2	23.72	5.39	0.68
z08PA71-15	Gneiss	37.0168	25.2013	11.1	0.9	458.8	73.2	475.6	0.2	22.75	10.43	0.80
z08PA71-16	Gneiss	37.0168	25.2013	9.2	0.7	304.2	30.2	311.1	0.1	12.19	9.18	0.79
z08PA71-17	Gneiss	37.0168	25.2013	9.8	0.8	475.4	104.8	499.5	0.2	19.49	7.09	0.74
z08PA71-18	Gneiss	37.0168	25.2013	14.3	1.1	639.4	96.2	661.5	0.2	41.59	13.41	0.81
z08PA71-19	Gneiss	37.0168	25.2013	9.6	0.8	521.9	38.8	530.8	0.1	21.01	6.54	0.77
z08PA71-20	Gneiss	37.0168	25.2013	11.7	0.9	309.8	103.9	333.7	0.3	16.93	12.96	0.81

Sample	Rock Type	Latitude [D.dddd]	Longitude [D.dddd]	Age [Ma]	$\pm 2\sigma$ (8%) [My]	U [ppm]	Th [ppm]	eU [ppm]	Th/U	He [nmol/g]	Mass [ $\mu$ g]	Ft
z08PA71-21	Gneiss	37.0168	25.2013	13.2	1.1	773.9	74.0	791.0	0.1	44.89	10.55	0.80
z08PA71-22	Gneiss	37.0168	25.2013	10.1	0.8	1255.8	149.9	1290.3	0.1	56.63	11.02	0.81
z08PA72-1	Gneiss	37.0244	25.2494	8.4	0.7	481.4	109.9	506.7	0.2	18.84	13.00	0.82
z08PA72-2	Gneiss	37.0244	25.2494	6.4	0.5	177.9	41.5	187.5	0.2	5.32	13.40	0.83
z08PA72-3	Gneiss	37.0244	25.2494	7.6	0.6	136.9	22.4	142.1	0.2	4.61	8.10	0.80
z08PA73-1	Gneiss	37.0438	25.2132	7.8	0.6	620.1	58.3	633.5	0.1	19.90	4.40	0.75
z08PA73-2	Gneiss	37.0438	25.2132	7.9	0.6	213.7	78.1	231.7	0.4	7.54	5.20	0.76
z08PA73-3	Gneiss	37.0438	25.2132	8.2	0.7	194.4	30.9	201.5	0.2	6.85	5.80	0.77
z08PA74-1	Gneiss	37.1522	25.2261	8.1	0.6	727.1	34.8	735.1	0.0	26.04	11.60	0.81
z08PA74-2	Gneiss	37.1522	25.2261	8.6	0.7	769.8	129.4	799.6	0.2	28.44	6.00	0.77
z08PA74-3	Gneiss	37.1522	25.2261	8.1	0.7	789.4	73.5	806.3	0.1	28.59	11.20	0.81
z08PA75-1	Gneiss	37.1267	25.1849	8.6	0.7	194.5	45.8	205.1	0.2	7.31	6.10	0.77
z08PA75-2	Gneiss	37.1267	25.1849	9.9	0.8	136.5	43.9	146.6	0.3	6.03	5.20	0.77
z08PA75-3	Gneiss	37.1267	25.1849	9.2	0.7	308.1	122.1	336.2	0.4	13.61	13.40	0.82
z08PA76-1	Gneiss	37.1190	25.1657	9.4	0.7	222.0	77.9	239.9	0.4	9.62	8.30	0.79
z08PA76-2	Gneiss	37.1190	25.1657	7.7	0.6	559.7	107.2	584.4	0.2	19.84	12.20	0.82
z08PA76-3	Gneiss	37.1190	25.1657	10.3	0.8	131.1	29.1	137.8	0.2	6.29	11.40	0.82
z08PA77-1	Gneiss	37.0994	25.1453	9.9	0.8	478.0	94.1	499.7	0.2	20.30	4.80	0.76
z08PA77-2	Gneiss	37.0994	25.1453	9.0	0.7	115.1	62.7	129.5	0.5	4.91	6.40	0.78
z08PA77-3	Gneiss	37.0994	25.1453	8.3	0.7	181.2	67.8	196.8	0.4	6.81	5.60	0.77
z08PA78-1	Gneiss	37.1233	25.2316	7.6	0.6	570.2	97.8	592.8	0.2	19.29	9.40	0.79
z08PA78-2	Gneiss	37.1233	25.2316	8.6	0.7	152.9	29.3	159.7	0.2	6.13	13.80	0.83
z08PA78-3	Gneiss	37.1233	25.2316	8.3	0.7	397.0	61.5	411.1	0.2	14.99	11.30	0.82
z09PA16-1	Granite	37.1197	25.2031	9.4	0.8	3904.8	159.0	3941.4	0.0	149.25	4.74	0.75
z09PA16-2	Granite	37.1197	25.2031	8.9	0.7	2622.7	174.6	2662.9	0.1	105.58	16.16	0.83
z09PA16-3	Granite	37.1197	25.2031	10.7	0.9	207.7	78.3	225.7	0.4	9.87	6.45	0.75

- <sup>1</sup> Abraded Zircon
- <sup>2</sup> Concentration Profiled Zircon
- NOTE: Unlisted grains lost during processing

**Table 2.** Zircon (U-Th)/He results from extensive footwall sampling campaign on Paros. Sample locations in Figure 2. All aliquots are single grains. All heating, digestion and nuclide analyses were performed at KU-IGL. See full method description in text. Results are shown in Figures 9 and 10.

Sample	Rock Type	Latitude [D.dddd]	Longitude [D.dddd]	Age [Ma]	$\pm 2\sigma$ (6%) [Ma]	U [ppm]	Th [ppm]	<sup>147</sup> Sm [ppm]	eU [ppm]	Th/U	He [nmol/g]	Mass [μg]	Ft
08PA01-1	Gneiss	37.039	25.261	9.9	0.6	14.8	1.7	91.1	15.7	0.1	0.72	20.69	0.85
08PA01-2*¥	Gneiss	37.039	25.261	4.7	0.3	0.3	1.5	0.9	0.6	4.9	0.01	3.04	0.61
08PA01-3	Gneiss	37.039	25.261	10.0	0.6	9.0	2.4	91.3	10.0	0.3	0.39	2.99	0.71
08PA01-4	Gneiss	37.039	25.261	9.7	0.6	14.9	11.6	129.4	18.2	0.8	0.62	1.76	0.63
08PA04-1	Gneiss	37.040	25.263	9.8	0.6	4.2	0.8	43.6	4.6	0.2	0.21	24.37	0.85
08PA04-2	Gneiss	37.040	25.263	9.3	0.6	6.3	0.9	47.7	6.7	0.1	0.30	24.37	0.85
08PA04-3#	Gneiss	37.040	25.263	19.2	1.1	7.0	1.6	54.6	7.6	0.2	0.65	11.44	0.81
08PA04-4	Gneiss	37.040	25.263	9.4	0.6	5.6	1.4	65.2	6.2	0.3	0.24	7.39	0.73
08PA04-5	Gneiss	37.040	25.263	9.4	0.6	6.2	1.0	65.2	6.7	0.2	0.28	10.29	0.81
08PA04-6	Gneiss	37.040	25.263	9.5	0.6	4.1	1.7	44.1	4.7	0.4	0.18	3.68	0.73
08PA48-1	Granite	37.132	25.214	15.5	0.9	8.4	16.1	88.3	12.5	1.9	0.71	4.11	0.66
08PA48-2	Granite	37.132	25.214	13.7	0.8	10.7	18.7	99.9	15.5	1.7	0.81	5.40	0.68
08PA48-3#	Granite	37.132	25.214	27.7	1.7	3.9	6.0	64.2	5.6	1.6	0.52	2.38	0.60
08PA71-1	Gneiss	37.017	25.201	11.7	0.7	11.5	1.2	38.5	12.0	0.1	0.53	5.51	0.69
08PA71-2	Gneiss	37.017	25.201	10.3	0.6	16.8	1.3	55.9	17.4	0.1	0.64	3.50	0.66
08PA71-3	Gneiss	37.017	25.201	13.5	0.8	27.9	2.0	67.0	28.7	0.1	1.43	4.37	0.68
08PA71-4	Gneiss	37.017	25.201	9.4	0.6	18.9	1.4	39.1	19.4	0.1	0.59	1.84	0.59
08PA71-5	Gneiss	37.017	25.201	11.7	0.7	14.5	0.8	34.2	14.9	0.1	0.64	3.82	0.68
08PA78-1	Gneiss	37.123	25.232	10.7	0.6	9.2	0.9	32.3	9.5	0.1	0.46	13.57	0.83
08PA78-2#	Gneiss	37.123	25.232	23.0	1.4	20.2	7.1	77.3	22.2	0.4	1.83	3.28	0.66
08PA78-3#	Gneiss	37.123	25.232	28.2	1.7	17.3	5.8	71.9	19.0	0.3	1.80	2.31	0.62
09PA16-1	Granite	37.127	25.211	13.5	0.8	11.0	18.4	56.0	15.5	1.7	0.75	4.46	0.65
09PA16-2#	Granite	37.127	25.211	44.2	2.7	6.1	6.0	47.6	7.7	1.0	1.16	2.64	0.62
09PA16-3	Granite	37.127	25.211	13.9	0.8	20.5	23.4	58.8	26.2	1.1	1.55	8.54	0.78
09PA16-4	Granite	37.127	25.211	12.3	0.7	26.8	27.8	57.6	33.5	1.0	1.64	4.86	0.73
08PA61-1¥	Dryos Schist	37.071	25.122	6.0	0.4	1.0	4.4	3.3	2.0	4.4	0.04	1.68	0.54

Sample	Rock Type	Latitude [D.ddd]	Longitude [D.ddd]	Age [Ma]	$\pm 2\sigma$ (6%) [Ma]	U [ppm]	Th [ppm]	<sup>147</sup> Sm [ppm]	eU [ppm]	Th/U	He [nmol/g]	Mass [μg]	Ft
08PA61-2#	Dryos Schist	37.071	25.122	9.3	0.6	2.0	3.1	2.0	2.7	1.6	0.08	2.06	0.59
08PA61-3#	Dryos Schist	37.071	25.122	10.5	0.6	1.0	1.1	1.6	1.2	1.1	0.04	2.48	0.61
08PA61-4#	Dryos Schist	37.071	25.122	4.3	0.3	0.8	2.3	2.0	1.3	2.9	0.02	1.95	0.57
08PA61-5#	Dryos Schist	37.071	25.122	11.4	0.7	0.8	3.2	3.2	1.5	4.0	0.05	1.62	0.53

\* Low Uranium (< 0.5 ppm)  
# Low Helium (< 0.1 nmol/g)  
# Mineral Inclusion(?)  
NOTE: Unlisted grains lost during processing

**Table 3.** Apatite (U-Th)/He results from the footwall sampling campaign on Paros. Sample locations in Figure 2. Aliquots are either single or double grains. All heating, digestion and nuclide analyses were performed at KU-IGL. See full method description in text. Results are shown in Figures 9 and 10.



Sample	Rock Type	Latitude [D.dddd]	Longitude [D.dddd]	Age [Ma]	$\pm 2\sigma$ (8%) [Ma]	U [ppm]	Th [ppm]	eU [ppm]	Th/U	He [nmol/g]	Mass [ $\mu$ g]	Ft
z08PA16-1	Unit A Green SS	37.1488	25.2744	58.1	4.6	293.9	79.3	312.2	0.3	73.85	4.30	0.75
z08PA16-2	Unit A Green SS	37.1488	25.2744	22.3	1.8	85.4	115.9	112.1	1.4	11.01	11.00	0.81
z08PA16-3	Unit A Green SS	37.1488	25.2744	93.6	7.5	170.1	52.3	182.1	0.3	70.86	5.30	0.77
z08PA16-4	Unit A Green SS	37.1488	25.2744	94.7	7.6	285.9	146.9	319.8	0.5	110.99	2.30	0.67
z08PA16-5	Unit A Green SS	37.1488	25.2744	63.6	5.1	315.8	125.5	344.8	0.4	81.32	2.81	0.68
z08PA16-8	Unit A Green SS	37.1488	25.2744	65.2	5.2	683.3	205.8	730.7	0.3	176.50	2.66	0.68
z08PA16-9	Unit A Green SS	37.1488	25.2744	57.2	4.6	385.8	92.3	407.0	0.2	88.93	3.30	0.71
z08PA16-10	Unit A Green SS	37.1488	25.2744	18.9	1.5	190.5	246.9	247.3	1.3	17.21	2.47	0.68
z08PA16-11	Unit A Green SS	37.1488	25.2744	75.4	6.0	219.9	57.4	233.2	0.3	71.71	5.57	0.75
z09PA08-1	Unit B Red SS lens	37.1479	25.2758	82.5	6.6	244.4	93.5	265.9	0.4	85.72	3.81	0.72
z09PA08-2	Unit B Red SS lens	37.1479	25.2758	71.7	5.7	127.4	35.1	135.5	0.3	38.12	4.20	0.72
z09PA08-3	Unit B Red SS lens	37.1479	25.2758	70.8	5.7	526.7	193.4	571.2	0.4	158.23	3.71	0.72
z09PA08-4	Unit B Red SS lens	37.1479	25.2758	72.4	5.8	239.3	114.7	265.7	0.5	76.18	4.20	0.73
z09PA08-5	Unit B Red SS lens	37.1479	25.2758	91.3	7.3	49.2	28.6	55.8	0.6	20.39	4.88	0.74
z09PA08-6	Unit B Red SS lens	37.1479	25.2758	18.3	1.5	254.2	261.3	314.3	1.0	21.61	3.14	0.69
z08PA13-1	Unit B Red SS lens	37.1479	25.2758	105.3	8.4	183.4	59.7	197.1	0.3	83.01	3.70	0.74
z08PA13-2	Unit B Red SS lens	37.1479	25.2758	63.8	5.1	557.1	92.6	578.4	0.2	151.91	4.70	0.76
z08PA13-3	Unit B Red SS lens	37.1479	25.2758	67.0	5.4	301.4	115.8	328.0	0.4	89.81	4.30	0.75
z08PA13-4	Unit B Red SS lens	37.1479	25.2758	60.3	4.8	272.0	90.5	292.9	0.3	71.34	3.94	0.75
z08PA13-5	Unit B Red SS lens	37.1479	25.2758	76.3	6.1	270.7	117.8	297.9	0.4	88.26	2.95	0.72
z08PA13-6	Unit B Red SS lens	37.1479	25.2758	68.9	5.5	337.1	70.8	353.4	0.2	105.04	8.74	0.80
z08PA13-7	Unit B Red SS lens	37.1479	25.2758	88.2	7.1	256.6	153.6	292.1	0.6	97.12	2.54	0.69
z08PA13-8	Unit B Red SS lens	37.1479	25.2758	62.1	5.0	283.4	92.4	304.7	0.3	74.53	3.05	0.73
z08PA13-9	Unit B Red SS lens	37.1479	25.2758	72.1	5.8	483.9	204.2	531.0	0.4	144.93	2.26	0.70
z08PA13-10	Unit B Red SS lens	37.1479	25.2758	78.4	6.3	213.1	152.0	248.1	0.7	80.62	5.58	0.76
z08PA14-1	Unit B Rhyolite Clast	37.1479	25.2757	64.5	5.2	717.0	32.3	724.5	0.0	209.83	19.01	0.83

Sample	Rock Type	Latitude [D.dddd]	Longitude [D.dddd]	Age [Ma]	$\pm 2\sigma$ (8%) [Ma]	U [ppm]	Th [ppm]	eU [ppm]	Th/U	He [nmol/g]	Mass [ $\mu$ g]	Ft
z08PA14-2	Unit B Rhyolite Clast	37.1479	25.2757	64.0	5.1	234.9	25.7	240.9	0.1	51.56	1.46	0.62
z08PA32-1	Unit F Purple SS lens	37.0754	25.2461	60.5	4.8	593.5	278.4	657.6	0.5	167.82	6.80	0.78
z08PA32-2	Unit F Purple SS lens	37.0754	25.2461	47.9	3.8	20.1	23.4	25.5	1.2	4.81	3.30	0.73
z08PA32-3	Unit F Purple SS lens	37.0754	25.2461	43.9	3.5	93.8	57.3	107.0	0.6	16.87	1.60	0.66
z08PA32-4	Unit F Purple SS lens	37.0754	25.2461	23.3	1.9	95.4	25.8	101.3	0.3	9.49	3.70	0.75
z09PA13-1	Unit F Purple SS lens	37.0754	25.2462	92.8	7.4	202.1	169.5	241.1	0.8	79.53	2.03	0.65
z09PA13-2	Unit F Purple SS lens	37.0754	25.2462	109.7	8.8	534.0	240.5	589.3	0.5	244.93	3.05	0.70
z09PA13-3	Unit F Purple SS lens	37.0754	25.2462	92.1	7.4	87.9	25.6	93.8	0.3	32.82	3.94	0.70
z09PA13-4	Unit F Purple SS lens	37.0754	25.2462	75.3	6.0	158.8	138.4	190.7	0.9	54.07	2.19	0.69
z09PA13-5	Unit F Purple SS lens	37.0754	25.2462	67.4	5.4	25.2	8.1	27.1	0.3	6.79	3.09	0.69
z09PA13-6	Unit F Purple SS lens	37.0754	25.2462	78.9	6.3	146.8	140.1	179.0	1.0	56.71	5.43	0.74
z08PA54-3	Unit E Fossiliferous SS	37.1194	25.2424	85.3	6.8	276.1	107.8	300.9	0.4	105.17	5.00	0.75
z08PA54-4	Unit E Fossiliferous SS	37.1194	25.2424	60.9	4.9	368.2	150.8	403.0	0.4	96.63	3.00	0.73
z08PA54-5	Unit E Fossiliferous SS	37.1194	25.2424	98.2	7.9	277.5	128.8	307.2	0.5	123.19	4.50	0.75
z08PA54-6	Unit E Fossiliferous SS	37.1194	25.2424	83.9	6.7	382.8	227.5	435.2	0.6	148.85	4.10	0.75
z08PA54-7	Unit E Fossiliferous SS	37.1194	25.2424	223.9	17.9	321.4	106.8	346.0	0.3	278.26	2.05	0.66
z08PA54-8	Unit E Fossiliferous SS	37.1194	25.2424	148.5	11.9	202.4	36.6	210.9	0.2	108.37	3.84	0.64
z08PA54-9	Unit E Fossiliferous SS	37.1194	25.2424	49.5	4.0	80.6	36.0	88.9	0.4	16.27	2.73	0.68
z08PA54-10	Unit E Fossiliferous SS	37.1194	25.2424	113.8	9.1	173.5	38.7	182.4	0.2	77.56	2.81	0.69
z08PA54-11	Unit E Fossiliferous SS	37.1194	25.2424	31.8	2.5	671.3	254.8	730.0	0.4	91.71	5.02	0.73
z08PA33-1	Unit 1 Lower SS	37.0682	25.2646	42.3	3.4	221.5	78.9	239.7	0.4	40.19	3.30	0.73
z08PA33-2	Unit 1 Lower SS	37.0682	25.2646	121.4	9.7	238.9	73.0	255.7	0.3	122.42	3.10	0.72
z08PA33-3	Unit 1 Lower SS	37.0682	25.2646	67.3	5.4	622.7	280.8	687.4	0.5	184.89	3.60	0.74
z08PA33-4	Unit 1 Lower SS	37.0682	25.2646	101.1	8.1	191.9	58.5	205.4	0.3	88.67	7.96	0.79
z08PA33-5	Unit 1 Lower SS	37.0682	25.2646	97.2	7.8	359.1	157.5	395.5	0.4	156.27	4.49	0.75
z08PA33-6	Unit 1 Lower SS	37.0682	25.2646	52.6	4.2	610.3	25.5	616.2	0.0	125.23	3.13	0.71

Sample	Rock Type	Latitude [D.dddd]	Longitude [D.dddd]	Age [Ma]	$\pm 2\sigma$ (8%) [Ma]	U [ppm]	Th [ppm]	eU [ppm]	Th/U	He [nmol/g]	Mass [ $\mu$ g]	Ft
z08PA33-7	Unit 1 Lower SS	37.0682	25.2646	71.4	5.7	370.5	54.5	383.1	0.1	105.14	2.81	0.71
z08PA33-8	Unit 1 Lower SS	37.0682	25.2646	51.7	4.1	248.7	55.2	261.4	0.2	52.71	3.14	0.72
z08PA33-9	Unit 1 Lower SS	37.0682	25.2646	67.8	5.4	425.5	87.7	445.7	0.2	115.49	2.66	0.71
z08PA33-10	Unit 1 Lower SS	37.0682	25.2646	51.7	4.1	227.2	75.3	244.6	0.3	50.76	3.94	0.74
z09PA12-1	Unit 1 Lower SS	37.0682	25.2646	71.1	5.7	310.9	101.1	334.2	0.3	95.92	4.96	0.74
z09PA12-2	Unit 1 Lower SS	37.0682	25.2646	80.2	6.4	274.2	72.6	290.9	0.3	92.85	4.50	0.73
z09PA12-3	Unit 1 Lower SS	37.0682	25.2646	76.7	6.1	324.8	46.2	335.4	0.1	99.76	3.20	0.72
z09PA12-4	Unit 1 Lower SS	37.0682	25.2646	79.0	6.3	315.6	96.1	337.8	0.3	100.26	2.62	0.69
z09PA12-5	Unit 1 Lower SS	37.0682	25.2646	61.5	4.9	293.3	51.7	305.3	0.2	71.35	3.75	0.70
z09PA12-6	Unit 1 Lower SS	37.0682	25.2646	67.9	5.4	186.8	65.1	201.8	0.3	49.40	2.88	0.67
z09PA12-7	Unit 1 Lower SS	37.0682	25.2646	66.3	5.3	238.5	100.5	261.7	0.4	67.99	3.69	0.72
z09PA12-8	Unit 1 Lower SS	37.0682	25.2646	74.3	5.9	334.2	161.7	371.4	0.5	106.39	3.63	0.71
z08PA06-1	Unit 1 Lower SS	37.0428	25.2652	50.0	4.0	183.6	112.6	209.6	0.6	42.75	5.10	0.75
z08PA06-2	Unit 1 Lower SS	37.0428	25.2652	26.0	2.1	282.9	61.7	297.1	0.2	31.17	4.00	0.75
z08PA06-3	Unit 1 Lower SS	37.0428	25.2652	52.5	4.2	402.2	160.8	439.3	0.4	96.99	6.00	0.78
z08PA06-4	Unit 1 Lower SS	37.0428	25.2652	33.0	2.6	133.5	39.1	142.5	0.3	20.51	10.47	0.81
z08PA06-5	Unit 1 Lower SS	37.0428	25.2652	50.3	4.0	101.4	39.5	110.6	0.4	22.54	4.17	0.75
z08PA06-6	Unit 1 Lower SS	37.0428	25.2652	25.3	2.0	167.4	48.0	178.5	0.3	18.81	5.46	0.77
z08PA06-7	Unit 1 Lower SS	37.0428	25.2652	26.4	2.1	269.4	74.9	286.7	0.3	29.06	2.98	0.71
z08PA06-8	Unit 1 Lower SS	37.0428	25.2652	81.0	6.5	71.5	60.0	85.4	0.8	27.06	3.07	0.72
z08PA06-9	Unit 1 Lower SS	37.0428	25.2652	78.4	6.3	212.8	15.6	216.4	0.1	71.22	5.93	0.78
z08PA06-10	Unit 1 Lower SS	37.0428	25.2652	52.9	4.2	228.8	53.4	241.1	0.2	52.74	5.92	0.76
z09PA09-1	Unit 1 Lower SS	37.0428	25.2652	33.8	2.7	604.1	229.2	656.9	0.4	89.29	4.85	0.74
z09PA09-2	Unit 1 Lower SS	37.0428	25.2652	22.9	1.8	189.7	51.9	201.6	0.3	18.35	5.08	0.73
z09PA09-3	Unit 1 Lower SS	37.0428	25.2652	43.4	3.5	203.5	74.9	220.7	0.4	37.96	4.05	0.73
z09PA09-4	Unit 1 Lower SS	37.0428	25.2652	24.4	2.0	723.4	156.5	759.5	0.2	70.45	3.06	0.70

Sample	Rock Type	Latitude [D.dddd]	Longitude [D.dddd]	Age [Ma]	$\pm 2\sigma$ (8%) [Ma]	U [ppm]	Th [ppm]	eU [ppm]	Th/U	He [nmol/g]	Mass [ $\mu$ g]	Ft
z09PA09-5	Unit 1 Lower SS	37.0428	25.2652	50.3	4.0	203.2	70.0	219.3	0.3	40.85	2.60	0.68
z09PA09-6	Unit 1 Lower SS	37.0428	25.2652	18.5	1.5	446.4	96.3	468.5	0.2	31.80	2.47	0.68
z09PA09-7	Unit 1 Lower SS	37.0428	25.2652	24.6	2.0	298.9	74.3	316.0	0.2	34.24	14.89	0.81
z09PA09-8	Unit 1 Lower SS	37.0428	25.2652	79.7	6.4	338.3	82.1	357.2	0.2	121.21	8.87	0.78
z09PA09-9 <sup>1</sup>	Unit 1 Lower SS	37.0428	25.2652	13.3	1.1	976.2	156.9	1012.3	0.2	49.83	2.89	0.68
z09PA09-10	Unit 1 Lower SS	37.0428	25.2652	34.6	2.8	231.4	106.3	255.9	0.5	34.55	4.71	0.72
z09PA09-11	Unit 1 Lower SS	37.0428	25.2652	67.1	5.4	141.7	48.1	152.8	0.3	40.60	4.74	0.73
z09PA09-12	Unit 1 Lower SS	37.0428	25.2652	41.3	3.3	98.6	33.6	106.3	0.3	18.49	7.53	0.78
z09PA09-13	Unit 1 Lower SS	37.0428	25.2652	35.0	2.8	251.5	63.3	266.1	0.3	35.70	3.45	0.71
z09PA09-14	Unit 1 Lower SS	37.0428	25.2652	41.7	3.3	94.9	69.3	110.8	0.7	19.45	6.38	0.78
z09PA09-15	Unit 1 Lower SS	37.0428	25.2652	43.9	3.5	293.8	123.4	322.2	0.4	50.52	2.34	0.66
z09PA09-16	Unit 1 Lower SS	37.0428	25.2652	61.0	4.9	420.7	200.2	466.8	0.5	104.64	2.67	0.68
z09PA09-17	Unit 1 Lower SS	37.0428	25.2652	25.2	2.0	148.4	74.5	165.5	0.5	15.33	2.60	0.68
z09PA09-18	Unit 1 Lower SS	37.0428	25.2652	46.9	3.8	186.4	33.3	194.0	0.2	34.75	3.62	0.71
z09PA09-19	Unit 1 Lower SS	37.0428	25.2652	42.2	3.4	282.1	79.4	300.3	0.3	49.83	3.79	0.73
z09PA09-20	Unit 1 Lower SS	37.0428	25.2652	21.9	1.8	210.0	45.8	220.5	0.2	17.54	2.71	0.67
z08PA08-1	Unit 1 Upper SS	37.0424	25.2667	47.2	3.8	585.7	158.2	622.2	0.3	118.53	5.66	0.75
z08PA08-2	Unit 1 Upper SS	37.0424	25.2667	104.6	8.4	99.2	23.2	104.5	0.2	42.93	3.97	0.72
z08PA08-3	Unit 1 Upper SS	37.0424	25.2667	28.6	2.3	168.2	34.5	176.1	0.2	20.98	5.71	0.77
z08PA08-4	Unit 1 Upper SS	37.0424	25.2667	43.5	3.5	280.0	92.2	301.3	0.3	54.90	7.72	0.77
z08PA08-5	Unit 1 Upper SS	37.0424	25.2667	20.6	1.6	247.2	40.1	256.4	0.2	21.33	5.54	0.75
z08PA08-6	Unit 1 Upper SS	37.0424	25.2667	15.6	1.2	259.9	45.7	270.4	0.2	17.61	9.04	0.77
z08PA08-7	Unit 1 Upper SS	37.0424	25.2667	28.1	2.2	280.5	119.7	308.1	0.4	33.76	3.36	0.72
z08PA08-8	Unit 1 Upper SS	37.0424	25.2667	46.1	3.7	251.7	150.8	286.5	0.6	50.61	3.97	0.71
z08PA08-9	Unit 1 Upper SS	37.0424	25.2667	46.2	3.7	790.3	418.3	886.6	0.5	146.44	2.54	0.66
z08PA08-10	Unit 1 Upper SS	37.0424	25.2667	60.5	4.8	357.6	167.7	396.3	0.5	96.81	4.65	0.75

Sample	Rock Type	Latitude [D.ddd]	Longitude [D.ddd]	Age [Ma]	$\pm 2\sigma$ (8%) [Ma]	U [ppm]	Th [ppm]	eU [ppm]	Th/U	He [nmol/g]	Mass [ $\mu$ g]	Ft
z08PA08-11	Unit 1 Upper SS	37.0424	25.2667	69.4	5.6	472.9	139.3	505.0	0.3	134.94	3.93	0.71
z08PA08-12	Unit 1 Upper SS	37.0424	25.2667	29.3	2.3	217.0	57.6	230.2	0.3	28.05	6.41	0.77
z09PA10-1	Unit 1 Upper SS	37.0442	25.2675	8.2	0.7	297.5	245.1	353.9	0.8	19.17	6.13	0.75
z09PA10-2	Unit 1 Upper SS	37.0442	25.2675	10.1	0.8	234.6	113.1	260.6	0.5	36.40	1.82	0.65
z09PA10-3	Unit 1 Upper SS	37.0442	25.2675	13.3	1.1	244.1	190.5	288.0	0.8	42.66	2.92	0.69
z09PA10-4	Unit 1 Upper SS	37.0442	25.2675	18.6	1.5	293.8	113.8	320.0	0.4	62.38	4.46	0.70
z09PA10-5	Unit 1 Upper SS	37.0442	25.2675	27.0	2.2	278.8	61.8	293.0	0.2	76.45	4.09	0.73
z09PA10-6	Unit 1 Upper SS	37.0442	25.2675	39.3	3.1	176.3	60.2	190.2	0.3	13.61	3.18	0.71
z09PA04-1	Unit 2 SltStone	37.0484	25.2713	39.6	3.2	287.8	91.5	308.9	0.3	33.35	5.03	0.74
z09PA04-2	Unit 2 SltStone	37.0484	25.2713	51.6	4.1	145.8	85.3	165.4	0.6	44.32	4.04	0.72
z09PA04-3	Unit 2 SltStone	37.0484	25.2713	56.6	4.5	138.2	57.5	151.4	0.4	35.12	5.85	0.76
z09PA04-4	Unit 2 SltStone	37.0484	25.2713	65.8	5.3	504.6	85.5	524.2	0.2	16.97	3.82	0.73
z09PA04-5	Unit 2 SltStone	37.0484	25.2713	68.4	5.5	240.0	128.0	269.5	0.5	85.32	3.12	0.69
z09PA04-6	Unit 2 SltStone	37.0484	25.2713	84.7	6.8	567.4	245.7	623.9	0.4	24.83	4.23	0.73
z08PA12-1	Unit 2 Granitic Horizon	37.0483	25.2711	9.2	0.7	353.1	143.4	386.1	0.4	15.57	11.20	0.81
z08PA12-2	Unit 2 Granitic Horizon	37.0483	25.2711	8.3	0.7	290.1	128.2	319.6	0.4	11.27	6.90	0.78
z08PA12-3	Unit 2 Granitic Horizon	37.0483	25.2711	8.8	0.7	692.0	289.7	758.6	0.4	28.51	9.00	0.79
z08PA12-4	Unit 2 Granitic Horizon	37.0483	25.2711	10.4	0.8	600.1	239.3	655.2	0.4	29.18	10.79	0.79
z08PA12-5	Unit 2 Granitic Horizon	37.0483	25.2711	11.6	0.9	519.5	292.9	586.9	0.6	27.95	8.38	0.76
z08PA12-6	Unit 2 Granitic Horizon	37.0483	25.2711	9.2	0.7	483.9	197.5	529.4	0.4	20.55	8.93	0.79
z08PA12-7	Unit 2 Granitic Horizon	37.0483	25.2711	9.9	0.8	384.1	189.4	427.8	0.5	18.57	15.40	0.81
z08PA12-8	Unit 2 Granitic Horizon	37.0483	25.2711	9.9	0.8	460.2	190.0	504.0	0.4	21.45	10.56	0.80
z08PA12-9	Unit 2 Granitic Horizon	37.0483	25.2711	9.9	0.8	385.9	171.8	425.5	0.4	17.74	10.57	0.78
z08PA12-10	Unit 2 Granitic Horizon	37.0483	25.2711	9.8	0.8	633.2	275.5	696.6	0.4	27.59	5.65	0.75
z08PA12-11	Unit 2 Granitic Horizon	37.0483	25.2711	8.4	0.7	1091.9	389.0	1181.6	0.4	40.46	5.99	0.76
z08PA12-12	Unit 2 Granitic Horizon	37.0483	25.2711	8.4	0.7	844.6	244.0	900.8	0.3	32.59	12.33	0.80

Sample	Rock Type	Latitude [D.dddd]	Longitude [D.dddd]	Age [Ma]	$\pm 2\sigma$ (8%) [Ma]	U [ppm]	Th [ppm]	eU [ppm]	Th/U	He [nmol/g]	Mass [ $\mu$ g]	Ft
z08PA12-13	Unit 2 Granitic Horizon	37.0483	25.2711	14.0	1.1	724.2	315.6	796.9	0.4	44.72	4.83	0.74
z09PA05-1	Unit 3 Silicified SS	37.0486	25.2712	94.2	7.5	321.3	62.8	335.8	0.2	114.28	3.73	0.67
z09PA05-3	Unit 3 Silicified SS	37.0486	25.2712	79.1	6.3	254.8	79.2	273.0	0.3	85.08	4.39	0.73
z09PA05-4	Unit 3 Silicified SS	37.0486	25.2712	8.5	0.7	768.2	251.0	826.0	0.3	28.01	4.51	0.74
z09PA05-5	Unit 3 Silicified SS	37.0486	25.2712	9.4	0.8	871.1	375.9	957.6	0.4	34.89	3.74	0.72
z09PA05-6	Unit 3 Silicified SS	37.0486	25.2712	52.7	4.2	883.1	352.2	964.2	0.4	186.57	2.50	0.68
z09PA05-7	Unit 3 Silicified SS	37.0486	25.2712	93.8	7.5	266.6	79.6	285.0	0.3	104.86	4.12	0.72
z09PA05-8	Unit 3 Silicified SS	37.0486	25.2712	113.3	9.1	227.9	75.0	245.1	0.3	113.79	6.01	0.75
z09PA06-1	Unit 3 Yellow SS	37.0483	25.2717	9.5	0.8	550.8	228.1	603.3	0.4	22.44	4.69	0.73
z09PA06-2	Unit 3 Yellow SS	37.0483	25.2717	9.1	0.7	521.1	227.3	573.4	0.4	19.82	3.29	0.70
z09PA06-3	Unit 3 Yellow SS	37.0483	25.2717	90.1	7.2	302.6	68.3	318.4	0.2	119.53	6.42	0.77
z09PA06-4	Unit 3 Yellow SS	37.0483	25.2717	9.0	0.7	713.4	254.1	771.9	0.4	25.40	2.64	0.68
z09PA06-5	Unit 3 Yellow SS	37.0483	25.2717	9.5	0.8	506.0	272.7	568.8	0.5	21.44	4.59	0.73
z09PA06-6	Unit 3 Yellow SS	37.0483	25.2717	8.8	0.7	531.4	185.9	574.2	0.3	19.26	3.49	0.70
z08PA34-1	Unit 3 Red SS	37.0486	25.2715	6.6	0.5	966.3	270.5	1028.6	0.3	29.18	8.40	0.80
z08PA34-2	Unit 3 Red SS	37.0486	25.2715	7.1	0.6	688.6	235.5	742.8	0.3	21.35	4.80	0.75
z08PA34-3	Unit 3 Red SS	37.0486	25.2715	37.6	3.0	331.8	88.3	352.1	0.3	53.70	4.20	0.75
z08PA34-4	Unit 3 Red SS	37.0486	25.2715	8.4	0.7	793.3	210.2	841.7	0.3	28.39	4.21	0.75
z08PA34-5	Unit 3 Red SS	37.0486	25.2715	9.6	0.8	923.1	304.9	993.3	0.3	37.19	3.43	0.73
z08PA34-6	Unit 3 Red SS	37.0486	25.2715	8.5	0.7	518.4	185.1	561.0	0.4	19.74	5.81	0.77
z08PA34-7	Unit 3 Red SS	37.0486	25.2715	7.9	0.6	494.9	172.7	534.7	0.3	16.34	3.24	0.72
z08PA34-8	Unit 3 Red SS	37.0486	25.2715	8.9	0.7	987.8	369.9	1073.1	0.4	38.39	4.70	0.75
z08PA34-9	Unit 3 Red SS	37.0486	25.2715	9.0	0.7	391.6	150.9	426.3	0.4	15.36	3.59	0.74
z08PA34-10	Unit 3 Red SS	37.0486	25.2715	8.5	0.7	441.7	174.3	481.9	0.4	16.69	4.42	0.75
z08PA34-11	Unit 3 Red SS	37.0486	25.2715	9.5	0.8	534.7	295.8	602.8	0.6	22.70	4.31	0.73
z08PA34-12	Unit 3 Red SS	37.0486	25.2715	10.5	0.8	217.7	176.8	258.4	0.8	9.96	2.46	0.68

Sample	Rock Type	Latitude [D.ddd]	Longitude [D.ddd]	Age [Ma]	$\pm 2\sigma$ (8%) [Ma]	U [ppm]	Th [ppm]	eU [ppm]	Th/U	He [nmol/g]	Mass [ $\mu$ g]	Ft
z09PA07-1	Unit 3 Red SS	37.1479	25.2758	9.4	0.8	847.6	227.1	899.9	0.3	34.52	7.25	0.75
z09PA07-2	Unit 3 Red SS	37.1479	25.2758	51.2	4.1	369.1	169.9	408.2	0.5	78.93	3.52	0.70
z09PA07-3	Unit 3 Red SS	37.1479	25.2758	54.8	4.4	155.1	42.6	164.9	0.3	35.07	4.26	0.72
z09PA07-4	Unit 3 Red SS	37.1479	25.2758	67.0	5.4	370.9	169.5	409.9	0.5	112.99	6.56	0.76
z09PA07-5	Unit 3 Red SS	37.1479	25.2758	44.5	3.6	442.0	183.0	484.2	0.4	75.74	2.11	0.65
z09PA07-6	Unit 3 Red SS	37.1479	25.2758	7.9	0.6	771.8	162.1	809.1	0.2	23.68	3.35	0.69
z09PA07-7	Unit 3 Red SS	37.1479	25.2758	8.4	0.7	506.8	114.3	533.1	0.2	19.10	8.91	0.79
z09PA07-8	Unit 3 Red SS	37.1479	25.2758	83.0	6.6	162.6	53.2	174.9	0.3	56.05	3.10	0.71
z09PA07-9	Unit 3 Red SS	37.1479	25.2758	9.2	0.7	519.4	203.6	566.3	0.4	20.91	5.71	0.74
z09PA07-10	Unit 3 Red SS	37.1479	25.2758	8.9	0.7	876.5	241.7	932.1	0.3	33.72	6.13	0.76
z09PA07-11	Unit 3 Red SS	37.1479	25.2758	92.1	7.4	285.6	95.1	307.5	0.3	113.03	4.47	0.73
z09PA07-12	Unit 3 Red SS	37.1479	25.2758	10.7	0.9	602.5	256.4	661.5	0.4	30.35	11.58	0.80
z08PA35-1	Unit 3 Rhyolite Clast	37.0485	25.2728	8.3	0.7	282.9	103.0	306.6	0.4	10.19	4.10	0.74
z08PA35-2	Unit 3 Rhyolite Clast	37.0485	25.2728	7.3	0.6	142.7	51.0	154.5	0.4	4.50	3.70	0.74
z08PA35-3	Unit 3 Rhyolite Clast	37.0485	25.2728	8.1	0.6	205.8	82.2	224.7	0.4	7.36	4.20	0.75
z08PA35-4	Unit 3 Rhyolite Clast	37.0485	25.2728	6.4	0.5	119.4	216.2	169.2	1.8	4.12	2.70	0.70
z08PA35-5	Unit 3 Rhyolite Clast	37.0485	25.2728	7.9	0.6	376.7	186.1	419.6	0.5	11.94	1.70	0.67
z08PA35-6	Unit 3 Rhyolite Clast	37.0485	25.2728	7.6	0.6	148.9	46.8	159.7	0.3	4.85	3.30	0.74
z09PA15-1	Unit 3 SS	37.0507	25.2720	12.7	1.0	278.4	67.3	293.9	0.2	15.16	7.16	0.75
z09PA15-2	Unit 3 SS	37.0507	25.2720	11.0	0.9	776.2	193.4	820.7	0.2	37.65	7.44	0.78
z09PA15-3	Unit 3 SS	37.0507	25.2720	10.4	0.8	314.1	126.3	343.2	0.4	15.12	10.93	0.78
z09PA15-4	Unit 3 SS	37.0507	25.2720	8.8	0.7	238.6	39.2	247.7	0.2	8.92	4.69	0.76
z09PA15-5	Unit 3 SS	37.0507	25.2720	63.8	5.1	371.7	30.7	378.8	0.1	99.00	6.39	0.76
z09PA15-6	Unit 3 SS	37.0507	25.2720	10.0	0.8	410.6	29.6	417.4	0.1	17.58	7.23	0.78
z09PA15-7	Unit 3 SS	37.0507	25.2720	61.7	4.9	155.3	63.1	169.8	0.4	46.25	14.69	0.81
z08PA41-1	Unit 3 Lighthouse SS	37.0495	25.2776	9.8	0.8	623.7	109.1	648.8	0.2	27.28	10.67	0.80

Sample	Rock Type	Latitude [D.dddd]	Longitude [D.dddd]	Age [Ma]	$\pm 2\sigma$ (8%) [Ma]	U [ppm]	Th [ppm]	eU [ppm]	Th/U	He [nmol/g]	Mass [ $\mu$ g]	Ft
z08PA41-2	Unit 3 Lighthouse SS	37.0495	25.2776	11.0	0.9	934.2	138.1	966.0	0.1	46.87	14.31	0.82
z08PA41-3	Unit 3 Lighthouse SS	37.0495	25.2776	10.0	0.8	451.2	204.5	498.3	0.5	21.56	10.17	0.80
z08PA41-4	Unit 3 Lighthouse SS	37.0495	25.2776	9.1	0.7	602.6	146.1	636.2	0.2	23.88	6.97	0.77
z08PA41-5	Unit 3 Lighthouse SS	37.0495	25.2776	8.9	0.7	660.1	165.0	698.1	0.3	25.64	8.40	0.77
z08PA41-6	Unit 3 Lighthouse SS	37.0495	25.2776	8.3	0.7	1051.5	233.5	1105.3	0.2	37.87	6.27	0.76
z08PA57-1	Unit 4 SS lens	37.1235	25.2820	8.8	0.7	1326.1	344.5	1405.4	0.3	49.28	3.70	0.74
z08PA57-2	Unit 4 SS lens	37.1235	25.2820	9.7	0.8	508.1	254.7	566.7	0.5	23.08	6.80	0.77
z08PA57-4	Unit 4 SS lens	37.1235	25.2820	9.6	0.8	1779.6	63.7	1794.3	0.0	65.01	3.33	0.70
z08PA57-5	Unit 4 SS lens	37.1235	25.2820	104.0	8.3	338.3	99.5	361.3	0.3	139.89	2.72	0.69
z08PA57-6	Unit 4 SS lens	37.1235	25.2820	9.7	0.8	461.6	95.3	483.6	0.2	18.35	3.52	0.72
z08PA57-7	Unit 4 SS lens	37.1235	25.2820	9.7	0.8	1368.6	385.6	1457.3	0.3	61.04	10.05	0.80
z08PA57-8	Unit 4 SS lens	37.1235	25.2820	8.4	0.7	591.5	312.3	663.5	0.5	21.77	3.96	0.72
z08PA57-9	Unit 4 SS lens	37.1235	25.2820	60.9	4.9	174.3	29.3	181.1	0.2	41.60	2.62	0.70
z08PA57-10	Unit 4 SS lens	37.1235	25.2820	11.7	0.9	633.9	290.0	700.7	0.5	31.03	2.85	0.70
z09PA17-1	Unit Z Moutsouna SS	37.0796	25.5894	77.3	6.2	98.6	38.4	107.4	0.4	33.39	5.46	0.74
z09PA17-2	Unit Z Moutsouna SS	37.0796	25.5894	42.8	3.4	617.3	264.5	678.2	0.4	111.97	3.70	0.71
z09PA17-3	Unit Z Moutsouna SS	37.0796	25.5894	40.7	3.3	217.6	102.5	241.2	0.5	39.70	5.82	0.75
z09PA17-4	Unit Z Moutsouna SS	37.0796	25.5894	92.6	7.4	519.8	34.8	527.8	0.1	202.33	6.25	0.76
z09PA17-5	Unit Z Moutsouna SS	37.0796	25.5894	54.7	4.4	155.2	97.6	177.7	0.6	36.82	3.06	0.70
z09PA17-6	Unit Z Moutsouna SS	37.0796	25.5894	95.7	7.7	145.6	58.0	158.9	0.4	57.37	3.02	0.69
z09PA17-7	Unit Z Moutsouna SS	37.0796	25.5894	130.5	10.4	270.2	96.5	292.4	0.4	169.83	15.08	0.82
z09PA17-8	Unit Z Moutsouna SS	37.0796	25.5894	140.3	11.2	426.5	77.5	444.4	0.2	248.23	4.32	0.73
z09PA17-9	Unit Z Moutsouna SS	37.0796	25.5894	270.0	21.6	183.5	64.0	198.3	0.3	214.85	4.28	0.73
z09PA17-10	Unit Z Moutsouna SS	37.0796	25.5894	120.5	9.6	222.9	121.9	251.0	0.5	124.91	6.47	0.76
z09PA17-11	Unit Z Moutsouna SS	37.0796	25.5894	78.2	6.3	282.2	63.0	296.7	0.2	89.81	3.75	0.71
z09PA17-12	Unit Z Moutsouna SS	37.0796	25.5894	20.7	1.7	183.4	233.2	237.1	1.3	19.57	5.08	0.73



<sup>1</sup> Highly Metamict Zircon

NOTE: Unlisted grains lost during processing

**Table 4.** Zircon (U-Th)/He results from the hanging wall sampling campaign in the Paros supradetachment basin. Sample locations in Figure 2. All aliquots are single grains. All heating, digestion and nuclide analyses were performed at KU-IGL. See full method description in text. Results are summarized as probability density plots in Figure 9.

Sample	Rock Type	Latitude [D.dddd]	Longitude [D.dddd]	Age [Ma]	$\pm 2\sigma$ (6%) [Ma]	U [ppm]	Th [ppm]	<sup>147</sup> Sm [ppm]	eU [ppm]	Th/U	He [nmol/g]	Mass [μg]	Ft
08PA16-1	Unit A SS	37.149	25.274	12.2	0.7	8.7	51.4	60.6	20.8	5.9	0.84	1.55	0.59
08PA16-2	Unit A SS	37.149	25.274	13.6	0.8	13.1	85.2	74.2	33.1	6.5	1.41	1.28	0.57
08PA16-3	Unit A SS	37.149	25.274	12.7	0.8	4.9	28.5	38.4	11.6	5.9	0.49	1.55	0.60
08PA16-4	Unit A SS	37.149	25.274	12.5	0.8	6.2	43.1	48.2	16.3	7.0	0.63	1.34	0.55
08PA16-5	Unit A SS	37.149	25.274	13.2	0.8	6.6	46.6	52.0	17.6	7.1	0.71	1.05	0.55
08PA16-6	Unit A SS	37.149	25.274	13.8	0.8	6.0	34.9	40.5	14.2	5.9	0.77	5.18	0.71
08PA16-7	Unit A SS	37.149	25.274	8.5	0.5	12.4	36.3	46.7	21.0	2.9	0.56	1.09	0.57
08PA16-8	Unit A SS	37.149	25.274	12.0	0.7	4.3	24.7	31.9	10.1	5.8	0.48	4.96	0.71
08PA54-1	Unit E SS	37.119	25.242	11.5	0.7	4.8	37.0	47.4	13.6	7.7	0.46	0.94	0.54
08PA54-2	Unit E SS	37.119	25.242	10.6	0.6	12.4	86.3	73.0	32.7	7.0	1.03	0.81	0.54
08PA54-3	Unit E SS	37.119	25.242	17.2	1.0	11.1	64.5	98.4	26.4	5.8	1.46	1.15	0.58
08PA54-4	Unit E SS	37.119	25.242	13.0	0.8	16.1	132.3	104.5	47.1	8.2	2.12	1.83	0.63
08PA54-5	Unit E SS	37.119	25.242	8.0	0.5	6.8	137.3	63.7	38.7	20.1	1.07	1.63	0.63
08PA54-6	Unit E SS	37.119	25.242	13.1	0.8	11.2	89.5	69.1	32.1	8.0	1.67	4.32	0.72
08PA06-1¥	Unit 1 SS	37.043	25.265	3.5	0.2	3.4	1.2	1.1	3.7	0.4	0.05	2.41	0.68
08PA06-2	Unit 1 SS	37.043	25.265	8.4	0.5	28.1	108.4	62.0	53.4	3.9	1.64	2.36	0.66
08PA06-3	Unit 1 SS	37.043	25.265	8.2	0.5	17.9	252.2	75.5	76.4	14.1	1.99	1.04	0.58
08PA06-4*	Unit 1 SS	37.043	25.265	1138.5	68.3	0.1	0.3	3.7	0.2	4.9	0.63	1.06	0.57
08PA06-5	Unit 1 SS	37.043	25.265	38.1	2.3	16.4	3.2	52.5	17.4	0.2	2.22	1.05	0.61
09PA09-1*¥	Unit 1 SS	37.043	25.265	3.4	0.2	0.2	1.6	0.8	0.5	8.9	0.01	1.59	0.61
09PA09-2¥	Unit 1 SS	37.043	25.265	-0.1	-0.0	4.3	1.9	1.3	4.8	0.4	-0.00	0.99	0.60
09PA09-3*¥	Unit 1 SS	37.043	25.265	-3.8	-0.2	0.4	1.3	1.5	0.7	3.3	-0.01	0.86	0.53
09PA09-4	Unit 1 SS	37.043	25.265	10.7	0.6	39.2	109.7	70.8	64.8	2.8	2.49	2.30	0.66
09PA09-5*¥	Unit 1 SS	37.043	25.265	5.1	0.3	0.6	3.4	2.3	1.4	5.6	0.02	1.15	0.59
09PA09-6¥	Unit 1 SS	37.043	25.265	-1.6	-0.1	0.3	1.0	0.7	0.6	3.3	-0.00	2.00	0.64
09PA09-7*¥	Unit 1 SS	37.043	25.265	1.3	0.1	0.1	0.3	0.3	0.2	2.3	0.00	5.07	0.72

Sample	Rock Type	Latitude [D.dddd]	Longitude [D.dddd]	Age [Ma]	$\pm 2\sigma$ (6%) [Ma]	U [ppm]	Th [ppm]	<sup>147</sup> Sm [ppm]	eU [ppm]	Th/U	He [nmol/g]	Mass [ $\mu$ g]	Ft
09PA09-8¥	Unit 1 SS	37.043	25.265	-0.3	-0.0	0.4	1.2	1.7	0.7	3.0	-0.00	1.52	0.61
08PA33-1	Unit 1 SS	37.068	25.265	7.2	0.4	5.3	25.9	21.5	11.4	4.9	0.26	1.09	0.58
08PA33-2*	Unit 1 SS	37.068	25.265	481.5	28.9	0.4	0.8	3.6	0.6	1.9	0.84	0.72	0.53
08PA33-3	Unit 1 SS	37.068	25.265	12.8	0.8	7.0	6.0	83.0	8.8	0.9	0.43	2.49	0.69
08PA33-4¥	Unit 1 SS	37.068	25.265	4.5	0.3	1.3	13.3	7.4	4.4	10.6	0.06	1.06	0.58
08PA12-1	Horizon SS	37.048	25.271	10.3	0.6	32.0	46.3	162.2	43.4	1.5	1.36	0.94	0.55
08PA12-2	Horizon SS	37.048	25.271	8.9	0.5	29.8	30.2	139.5	37.4	1.0	1.03	1.03	0.56
08PA12-3	Horizon SS	37.048	25.271	40.1	2.4	27.2	58.4	115.9	41.2	2.1	4.27	0.42	0.47
08PA12-4	Horizon SS	37.048	25.271	16.8	1.0	43.6	12.0	76.7	46.7	0.3	3.12	3.86	0.73
08PA12-5	Horizon SS	37.048	25.271	9.6	0.6	37.4	57.4	154.1	51.4	1.5	1.85	2.67	0.68
08PA12-6	Horizon SS	37.048	25.271	9.9	0.6	30.5	77.2	173.9	49.1	2.5	1.75	2.01	0.66
08PA12-7	Horizon SS	37.048	25.271	8.9	0.5	23.4	58.3	134.5	37.5	2.5	1.16	1.98	0.64
08PA34-1	Unit 3 SS	37.049	25.272	9.6	0.6	31.4	56.1	106.2	44.9	1.8	1.49	1.60	0.63
08PA34-2	Unit 3 SS	37.049	25.272	9.2	0.6	15.2	26.1	67.3	21.6	1.7	0.68	1.37	0.62
08PA34-3	Unit 3 SS	37.049	25.272	10.1	0.6	23.6	37.7	81.5	32.7	1.6	1.08	1.29	0.60
08PA34-4	Unit 3 SS	37.049	25.272	8.5	0.5	16.4	25.0	41.9	22.4	1.5	0.65	1.70	0.63
08PA34-5	Unit 3 SS	37.049	25.272	9.8	0.6	26.6	24.0	105.5	32.7	0.9	0.94	0.66	0.54
08PA34-6	Unit 3 SS	37.049	25.272	9.5	0.6	13.2	20.2	54.3	18.1	1.5	0.56	1.04	0.59
08PA34-7	Unit 3 SS	37.049	25.272	7.4	0.4	21.2	31.4	79.1	28.8	1.5	0.59	0.57	0.50
08PA34-8	Unit 3 SS	37.049	25.272	9.4	0.6	15.4	34.3	59.9	23.6	2.2	0.64	0.88	0.52
08PA34-9	Unit 3 SS	37.049	25.272	108.4	6.5	3.3	0.6	0.0	3.4	0.2	1.22	1.20	0.60
08PA34-10	Unit 3 SS	37.049	25.272	6.8	0.4	34.1	24.5	42.7	39.9	0.7	0.96	1.78	0.65
08PA34-11¥	Unit 3 SS	37.049	25.272	0.1	0.0	2.0	0.2	0.0	2.0	0.1	0.00	1.11	0.62
08PA54-7	Unit E SS	37.119	25.242	12.6	0.8	18.9	66.6	62.0	34.6	3.5	1.44	1.32	0.60
08PA57-1	Unit 4 SS	37.123	25.282	9.4	0.6	19.7	9.8	-1.3	21.9	0.5	0.66	0.94	0.59
08PA57-2	Unit 4 SS	37.123	25.282	10.8	0.6	9.0	5.6	-1.5	10.3	0.6	0.39	1.70	0.66

08PA57-3	Unit 4 SS	37.123	25.282	15.1	0.9	1.8	6.4	-3.6	3.2	3.6	0.14	0.70	0.54
08PA57-4	Unit 4 SS	37.123	25.282	11.0	0.7	25.5	16.9	-4.0	29.4	0.7	0.95	0.63	0.54
08PA57-5	Unit 4 SS	37.123	25.282	12.1	0.7	28.1	7.7	-3.2	29.9	0.3	1.12	0.78	0.57
08PA57-6	Unit 4 SS	37.123	25.282	14.0	0.8	54.0	8.6	5.3	56.0	0.2	2.37	0.74	0.56
08PA57-7¥	Unit 4 SS	37.123	25.282	2.3	0.1	1.0	0.3	1.6	1.1	0.3	0.01	2.39	0.69
08PA57-8¥	Unit 4 SS	37.123	25.282	7.7	0.5	1.0	1.7	2.9	1.4	1.6	0.04	1.35	0.62
08PA57-9*¥	Unit 4 SS	37.123	25.282	7.0	0.4	0.1	1.0	1.3	0.4	7.3	0.01	2.01	0.65
08PA57-10	Unit 4 SS	37.123	25.282	9.2	0.6	6.6	4.0	1.6	7.5	0.6	0.24	1.58	0.64

\* Low Uranium (< 0.5 ppm)

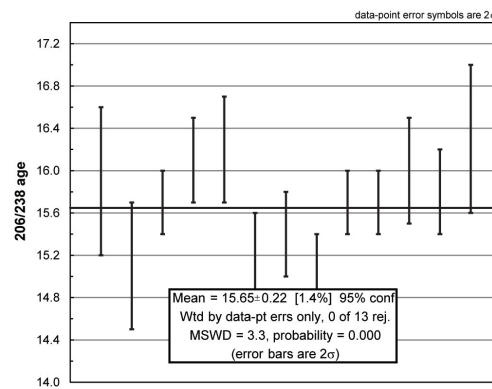
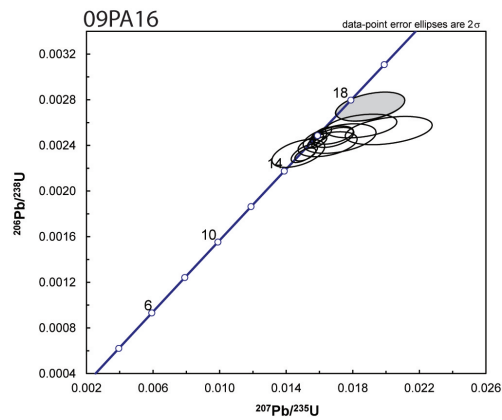
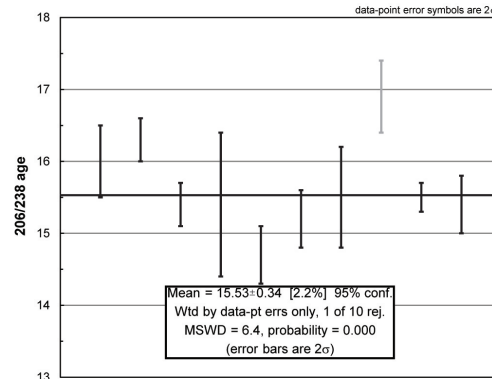
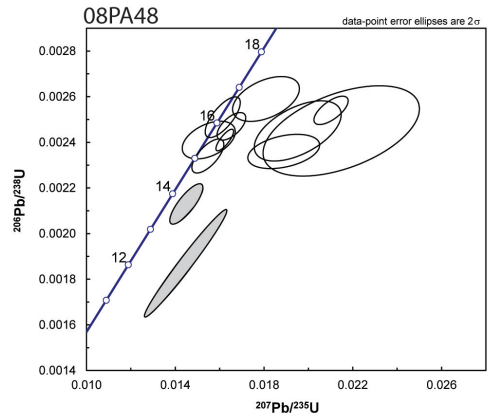
¥ Low Helium (< 0.1 nmol/g)

# Mineral Inclusion(?)

NOTE: Unlisted grains lost during processing

**Table 5.** Apatite (U-Th)/He results from the hanging wall sampling campaign in the Paros supradetachment basin. Sample locations in Figure 2. All aliquots are single grains. All heating, digestion and nuclide analyses were performed at KU-IGL. Some results are problematic due to low U and low He. See full method description in text. Results are summarized as probability density plots in Figure 9.

## APPENDIX A: KU-IGL U-Pb Data



GJ1 Standards

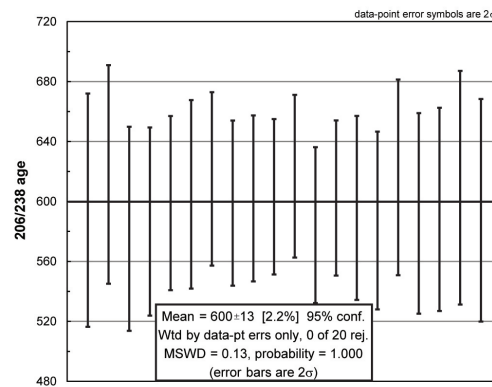


**Figure A1.** U-Pb results from the Kolymbithres pluton of Paros, Greece (See Chapter 2, Table 1 for sample locations). Plots were created using Isoplot 4. Shown are the concordia diagrams and weighted mean calculations for the two plutonic samples. Note that data were manually rejected prior to weighted mean calculations (see Table A1 for full list). Including rejected ages did not substantially change the final age of ~15 Ma.



	Measured Ratios			Corrected Ratios			Apparent Ages			
	206/238	207/235	207/206	206/238	207/235	207/206	206/238 [Ma]	2σ [Ma]	207/235 [Ma]	2σ [Ma]
GJ1	0.07654	0.83332	0.06015	0.09655	0.80353	0.06036	594.2	13.1	598.8	12.3
	0.07969	0.82969	0.06058	0.10061	0.84329	0.06079	618.0	11.8	621.0	11.2
	0.07462	0.77293	0.06008	0.09445	0.78475	0.06026	581.8	11.7	588.2	11.2
	0.07507	0.78601	0.05982	0.09526	0.78780	0.05998	586.6	10.7	589.9	10.3
	0.07653	0.76840	0.05959	0.09736	0.80168	0.05972	598.9	9.7	597.8	9.5
	0.07712	0.81649	0.05986	0.09835	0.81322	0.05997	604.7	10.4	604.3	10.1
	0.07830	0.81652	0.05977	0.10011	0.82626	0.05986	615.1	9.4	611.5	8.8
	0.07596	0.79678	0.05963	0.09736	0.80141	0.05970	598.9	9.2	597.6	9.5
	0.07618	0.76710	0.06013	0.09789	0.81212	0.06017	602.0	9.2	603.6	9.1
	0.07626	0.80843	0.06044	0.09807	0.81780	0.06048	603.1	8.6	606.8	8.7
	0.07789	0.80848	0.06058	0.10042	0.83892	0.06059	616.9	8.8	618.5	9.3
	0.07339	0.80887	0.06064	0.09485	0.79291	0.06063	584.2	8.9	592.8	9.0
	0.07558	0.73261	0.06016	0.09793	0.81191	0.06013	602.3	8.6	603.5	9.1
	0.07454	0.77606	0.05995	0.09682	0.79964	0.05990	595.7	10.3	596.6	10.0
	0.07325	0.78818	0.06019	0.09538	0.79051	0.06011	587.3	10.1	591.5	9.9
	0.07683	0.74480	0.05955	0.10029	0.82207	0.05945	616.1	10.6	609.2	10.1
	0.07351	0.77360	0.06036	0.09619	0.79894	0.06024	592.0	11.3	596.2	10.9
	0.07380	0.76128	0.06031	0.09665	0.80196	0.06018	594.7	11.4	597.9	10.9
0.07550	0.80383	0.06097	0.09911	0.83099	0.06081	609.2	12.8	614.2	12.1	
0.07348	0.76494	0.06037	0.09654	0.80145	0.06021	594.1	12.5	597.6	11.4	
08PA48	0.00199	0.01562	0.04649	0.00251	0.01614	0.04664	16.0	0.5	16.1	0.6
	0.00201	0.02162	0.05982	0.00254	0.02102	0.06001	16.3	0.3	21.0	0.6
	0.00195	0.01519	0.04840	0.00247	0.01653	0.04853	15.4	0.3	16.2	0.5

	Measured Ratios				Corrected Ratios				Apparent Ages			
	206/238	207/235	207/206		206/238	207/235	207/206		206/238 [Ma]	2 $\sigma$ [Ma]	207/235 [Ma]	2 $\sigma$ [Ma]
09PA16	0.00193	0.02873	0.06342		0.00245	0.02148	0.06358		15.4	1.0	21.0	2.8
	0.00184	0.01476	0.04785		0.00234	0.01547	0.04796		14.7	0.4	15.2	0.6
	0.00185	0.01214	0.05793		0.00236	0.01889	0.05805		15.2	0.4	19.0	1.3
	0.00192	0.01485	0.05769		0.00245	0.01952	0.05779		15.5	0.7	19.3	1.6
	0.00203	0.01519	0.05058		0.00259	0.01809	0.05066		16.9	0.5	18.4	1.2
	0.00188	0.01569	0.04876		0.00241	0.01623	0.04883		15.5	0.2	16.3	0.3
	0.00188	0.01627	0.04663		0.00241	0.01551	0.04668		15.4	0.4	15.6	1.0
	0.00166	0.01164	0.04932		0.00213	0.01450	0.04938		13.3	0.5	14.2	0.6
	0.00147	0.01900	0.05601		0.00187	0.01447	0.05613		12.1	1.2	14.7	1.5
	0.00191	0.02419	0.05071		0.00246	0.01721	0.05073		15.9	0.7	17.4	1.8
	0.00181	0.01747	0.04582		0.00233	0.01473	0.04584		15.1	0.6	14.9	1.3
	0.00188	0.01507	0.04770		0.00243	0.01599	0.04771		15.7	0.3	16.2	0.4
	0.00193	0.01520	0.04899		0.00249	0.01682	0.04899		16.1	0.4	17.0	1.0
	0.00199	0.01939	0.05222		0.00257	0.01850	0.05221		16.2	0.5	18.3	1.7
	0.00186	0.01145	0.04966		0.00241	0.01649	0.04964		15.0	0.6	16.1	1.4
	0.00180	0.01423	0.04699		0.00233	0.01509	0.04696		15.4	0.4	15.7	0.7
	0.00179	0.01585	0.04740		0.00232	0.01515	0.04736		15.1	0.3	15.5	0.5
	0.00190	0.01574	0.04688		0.00247	0.01595	0.04683		15.7	0.3	15.9	0.4
	0.00187	0.01575	0.04692		0.00244	0.01576	0.04685		15.7	0.3	15.9	0.4
	0.00189	0.01417	0.04958		0.00247	0.01685	0.04949		16.0	0.5	17.1	1.0
	0.00190	0.01560	0.04695		0.00249	0.01608	0.04684		15.8	0.4	15.9	0.5
	0.00193	0.01844	0.05793		0.00253	0.02016	0.05779		16.3	0.7	20.3	2.1
	0.00210	0.01744	0.05049		0.00274	0.01905	0.05042		17.7	0.7	19.2	1.7

Measured Ratios	Corrected Ratios			Apparent Ages		
206/238	207/235	207/206	206/238	207/235	206/238	207/235
0.02157	0.17861	0.05649	0.02820	0.21922	174.8	196.6
0.00129	0.00917	0.05079	0.00168	0.01175	16.2	17.7
					2 $\sigma$ [Ma]	2 $\sigma$ [Ma]
					8.5	9.2
					8.2	9.0

**Table A1.** U-Pb data collected at KU-IGL. Isotope ratios were measured on an Element 2 ICP-MS. No  $^{204}\text{Pb}$  correction was performed. Measured and corrected isotope ratios are given, along with apparent ages. See Figure A1 for concordia diagrams and weighted mean ages.

### **CHAPTER 3: Improved accuracy of zircon (U-Th)/He ages by rectifying parent nuclide zonation with practical methods**

#### **ABSTRACT**

Zircon (U-Th)/He thermochronometry is a potent tool for constraining the t-T evolution of tectonic systems, understanding the development of fault kinematics and elucidating thermal histories of upper crustal rocks. A major limitation in the accuracy of the method is the alpha-ejection correction, which statistically corrects for helium nuclei ejected from the crystal lattice during radioactive decay. The commonly used alpha-ejection correction assumes a homogeneous U-Th distribution in the host crystal, which has been empirically proven to be incorrect for many natural zircons; a methodology has been proposed to account for the heterogeneity. We present an empirical test and refinement of this methodology on a suite of bedrock zircons from Variscan orthogneisses of the central Aegean, which display marked parent nuclide heterogeneity. The findings show that a single sample may exhibit relative age biases between zircon aliquots of ~40%. This study also introduces a technique for determining the true ZHe age of a sample via mechanical abrasion of zircons. During progressive abrasion of enriched U, Th, and He zones, the change in grain diameter exhibits a parabolic relationship with respect to the apparent age, where the youngest age represents the true age of the sample. In this case, the abrasion-corrected weighted mean age for 08PA01 is  $8.8 \pm 0.7$  Ma. Custom ejection corrections informed by a LA-ICP-MS depth-profile increase the weighted mean age ~12% for sample 08PA01, from  $8.9 \pm 0.8$  Ma to  $10.4 \pm 0.8$  Ma, and ~7% for sample 08PA71, from  $10.3 \pm 0.8$  Ma to  $11.2 \pm 0.9$  Ma. These increases have

significant tectonic implications, indicating that cooling of the Paros footwall below 180°C may have occurred earlier than hitherto thought. The depth profile-controlled ejection correction modifies ages and may improve the overall accuracy of the (U-Th)/He technique, but further refinement is needed to reduce the overdispersion in ages.

## INTRODUCTION

Low-temperature thermochronometry is a powerful and popular method for tectonic and geomorphic investigations because of its ability to constrain time-temperature histories of upper crustal rocks. Data can be carefully interpreted and modeled to tease out information that provides insights into crustal processes (see Reiners and Ehlers, 2005). Various methodologies have been developed for calculating fault slip rates (e.g., John and Howard, 1995), exhumation rates (e.g., Braun, 2002), geothermal gradients (e.g., Brown, 1991) and kinematic histories (e.g., Ehlers et al., 2003). The number of tectonic studies is immense, but mineralogic evaluations of low-T thermochronometric methods have been largely limited to understanding the diffusion of noble gases in solids (Lovera et al., 1989; Wolf et al., 1996; Reiners et al., 2004; Cherniak et al., 2009). Curiously, thermochronometric data sets often produce improbable or overdispersed results, which are often attributed to mineral inclusions, lattice defects such as metamictization, or helium implantation. These errors can be difficult to spot and nearly impossible to identify with any degree of certainty. Some authors have expressed concerns over such inexplicable results and have raised questions about fundamental assumptions, which

are required to produce (U-Th)/He data, such as the zonation of uranium and thorium (Hourigan et al., 2005), anisotropic noble gas diffusion (Farley, 2007; Watson et al., 2010) and the myriad effects of radiation damage on the crystal lattice (Flowers et al., 2007; Flowers et al., 2009; Marsellos and Garver, 2010; Nasdala et al., 2004; Nasdala et al., 2010; Shuster et al., 2006) and on diffusion (Meesters and Dunai, 2002).

The likelihood for compositional complications in zircon is higher when considering rocks that may have a convolute thermal history and have cooled at variety of rates during a variety of tectonic episodes. During high-temperature and/or high-pressure events, elements may reorganize within the crystal lattice, minerals may grow (concentrically and otherwise) incorporating elements from dissolved minerals or cannibalizing their cores, and often times new minerals can crystallize in the melt with a distinctly different composition. Thus, zircons subjected to intense metamorphism may be problematic for zircon (U-Th)/He dating, especially if the zircons exhibit complex zonation or parent nuclide patterns with highly differential concentrations (Figure 1).

The zircons from high-grade rocks of the Paros metamorphic core complex of the Central Cyclades Islands, Greece (Figure 2) display complex and variable zonation patterns. The gneisses of the footwall have experienced multiple tectonic events which are not well constrained in time, including a pervasive amphibolite facies overprinting of an earlier high-pressure event (Avigad, 1998). Rapid, large-magnitude extension of the collapsing Alpine orogen exhumed the Paros metamorphic core complex at fast rates along a low-angle detachment fault (Bargnesi,

Chapter 2). The resultant rapid cooling should be recorded by AHe data that are the same age or slightly younger than the zircon (U-Th)/He (ZHe) ages for the same samples. This data should allow calculation of the cooling rate and geothermal gradient, as well as extrapolation of the fault slip rate. However, a systematic AHe and ZHe investigation into the footwall of the Paros metamorphic complex produces data incompatible with this hypothesis, wherein AHe ages are reproducibly older than ZHe ages in given footwall samples (Brichau, 2006; Bargnesi, Chapter 2) (Figure 3).

Here we attempt to resolve this thermochronometric discrepancy in the Paros footwall by evaluating zircon zonation and its effects on (U-Th)/He dating. Specifically, this study challenges the fundamental assumption of homogenous parent nuclide distribution in zircon grains, especially those which have been subjected to high-grade metamorphic events or those that crystallized during such events. This study also refines the methodology for correcting effected data. Since zonation affects the alpha-ejection correction, which is a direct multiplier on the final age, understanding zonation is of great importance to the study of (U-Th)/He thermochronometry. We use mechanical abrasion of zoned zircon and Monte Carlo simulated alpha-ejection corrections informed by laser ablation depth-profiles as described by Hourigan and others (2005).

## **THE ALPHA-EJECTION CORRECTION**

The alpha-ejection, or  $F_T$ , correction is a statistical approach to correct for the potential ejection of  $^4\text{He}$  from a given crystal lattice. As the respective parent nuclides decay ( $^{238}\text{U}$ ,  $^{235}\text{U}$ ,  $^{232}\text{Th}$ ,  $^{147}\text{Sm}$ ), alpha particles are emitted with energy



approaching 8 MeV and can cause minor recoil of the parent nuclide involved (Farley et al., 1996). The absolute distance each alpha particle travels is a function of the mineral type, lattice integrity, and respective isotope ejecting the alpha particle (Farley et al., 1996). If the given isotope nucleus is less than the travel distance from the grain boundary, there is a statistical chance that an alpha particle may be ejected from the grain domain. To correct for this possibility, overall retentivity is calculated via analytical or Monte Carlo simulation techniques. One key assumption in making this calculation is a homogeneous distribution of parent nuclides throughout the grain, which if falsely assumed can lead to an over- or underestimation of the true (U-Th)/He age (Farley, 2002; Hourigan et al., 2005; Dobson et al., 2008) (Figures 1, 3 and 4).

The commonly used analytical solution for ejection correction on zircon utilizes early work from Farley and others (1996), which identified the procedure for both analytical and iterative approaches for simple geometries. For zircon, a density of 4.65 g/cm<sup>3</sup> and alpha stopping distances from Farley and others (1996) are used. Grain measurements of zircon length (L), width (W<sub>1</sub>) and sometimes depth (W<sub>2</sub>) are used to calculate surface area to volume ratio ( $\beta$ ). For tetragonal grains, this can be calculated by  $\beta = (4L+2W_1)/(L*W_1)$ . For orthorhombic grains, it is calculated by  $\beta = (2LW_1+2LW_2+2W_1W_2)/(LW_1W_2)$ . The analytical solution to the alpha-ejection correction is then given by  $F_T = 1 - 4.55*\beta + 5.2\beta^2$ , where -4.55 and 5.2 are second order polynomial fitting parameters (Farley, 2002). A more realistic approach

involving tip heights and a wider range of morphologies is also available (Hourigan et al., 2005).

In a Monte Carlo simulation, a two- or three-dimensional system of nodes is used to simulate the presence of parent nuclides. The simulation calculates the statistical likelihood of alpha-ejection at every given node based on its root concentration, then integrates over the entire grid and divides by the number of simulations to reach a bulk  $^4\text{He}$  retentivity. The model can be adjusted to accommodate a variety of geometries and variations in concentration (i.e., zonation and/or inclusions). In theory, the more accurate the input parameters mirror the actual crystal, the more accurate the result will be. The Monte Carlo approach is powerful and can be used to correct for U and Th zonation in zircons, assuming self-similar growth (Hourigan et al., 2005).

Modeling the alpha-ejection correction is more computationally and temporally intensive than analytical solutions, but can provide much greater accuracy, especially in cases of atypical morphologies or parent nuclide distribution patterns. Hourigan and others (2005) demonstrate a discrepancy between analytical and modeled ejection corrections in grains often used as standards. Depth-profiling U and Th of these grains reveals significant zonation, which contributes to the inaccuracy of the ejection correction and thus, the final age. This powerful technique allows direct measurement of the parent isotopes and creates a unique ejection correction for a specific grain. Here we refine this methodology on natural zircons from the island of Paros, Greece.

## PROCEDURES AND METHODS

### *Cathodoluminescence imaging of apatite and zircon*

Cathodoluminescent scanning electron microscopy (SEM-CL) imagery was captured on a LEO Field scanning electron microscope at the University of Kansas Microscopy and Imaging Laboratory (Figures 5 and 6). Roughly 40 zircon grains each from samples 08PA01 and 08PA71 were handpicked and mounted in low-Pb epoxy; a few apatite grains were also mounted from the same samples for comparison. The mounts were hand-polished, sputter coated with zero-Pb gold and grounded using Cu tape and Ag paint. Image magnification ranges from 400 – 1200x with a working distance of 14.2 mm and an electron high tension of 15.00 kV. Images were captured with a split detector under CL to evaluate zonation and with secondary electrons to evaluate zircon grain integrity and morphology

. Images from CL analyses are shown in Figures 5 and 6.

### *Mechanical abrasion of zircon*

Mechanical abrasion was used to assess if the effects of high concentration uranium rims could be offset by physical removal of the rim and implanted helium. A procedure similar to Krogh (1982) was utilized. Between 10 – 20 grains of similar width were handpicked and batch abraded with low-U pyrite in stainless steel abrasion vessels (Figure 7). Pyrite was determined to be the optimal choice for a buffer after abrading zircons alone and abrading zircons with pure quartz sand. When zircons are abraded alone, too few collisions occur for significant grain size reduction

to occur. When zircons are abraded with quartz sand, the similarity in mineral hardness can result in cracked or pitted zircons that shatter before reaching the target abrasion size. When pyrite is added, it acts a mediator for collisions, slowly wearing down the exterior of the crystals without pitting or shattering the crystals.

Assuming a nominal rim thickness of 10 $\mu$ m (based on CL imagery) and average alpha-stopping distances of 16.65 for  $^{238}\text{U}$ , 19.64 for  $^{235}\text{U}$ , and 19.32 for  $^{232}\text{Th}$  (Farley et al., 1996), the target abrasion thickness was ~30 $\mu$ m of radial distance (Figure 8). Grains were abraded for ~70 hours under 25 kPa of continuous air pressure. The pyrite-zircon mix was washed in a hot 7N  $\text{HNO}_3$  bath to dissolve the pyrite. After rinsing with DI water and acetone, individual zircons were measured and prepared for (U-Th)/He analysis (see discussion of helium extraction in Bargnesi, Chapter 2). All abrasion experiments and subsequent (U-Th)/He analyses were conducted at the University of Kansas Isotope Geochemistry Laboratory (KU-IGL) (Table 1).

#### *Laser ablation depth-profiling*

Samples were depth-profiled at University of California Santa Cruz using laser ablation with inductively coupled mass spectrometry (LA-ICP-MS). About 20 zircon grains from footwall samples 08PA01 and 08PA71 were analyzed. Grains were hand-picked, mounted on tape and placed in a HelEx laser ablation cell. Each grain was lased with a Photon Machines Analyte 193H Excimer laser at 40% output with an energy density of 5.15 J/cm<sup>2</sup> focused to a 17 $\mu$ m circular spot. Elemental analyses were performed on a Plasmaquad X-series ICP-MS with a SQUID

smoothing device. Samples were scanned for  $^{29}\text{Si}$ ,  $^{96}\text{Zr}$ ,  $^{178}\text{Hf}$ ,  $^{204,206,207,208}\text{Pb}$ ,  $^{232}\text{Th}$  and  $^{238}\text{U}$ .  $^{235}\text{U}$  was calculated *ex post facto* by dividing the  $^{238}\text{U}$  value by 137.88, making the assumption of constant natural abundance. A Sri Lankan zircon, M146, was used as a standard (ion probe-derived compositions are given in Nasdala et al., 2004) to correct for fractionation. Three standards were measured alternately with 20 depth-profiles. Drill pits were measured on a binocular microscope and analyzed for (U-Th)/He ages at KU-IGL (Table 2) (see procedure in Bargnesi, Chapter 2). Data were reduced from raw counts to ppm using Microsoft Excel 2010. An exponential fit was derived from the standards and used to calculate unknown concentrations from cps to limit the effect of fractionation.

#### *Unique alpha-ejection corrections*

Using LA-ICP-MS data, one-dimensional concentration arrays were modeled as three-dimensional using the Helium Modeling Package (HeMP) (Hager and Stockli, 2009). A spherical model using an identical surface area to volume ratio of a given tetragonal prism can provide a useful approximation for a computationally effective alpha-ejection Monte Carlo simulation. However, here we use tetragonal and orthorhombic prisms with bi-pyramidal tips, which allows for more accurate simulation, since tip-grown zones increase the likelihood of ejection and can contribute heavily to the statistical correction (Hourigan et al., 2005). We find that orthorhombic corrections are most useful, as few measured grains exhibit truly equal widths; a tetragonal model is only used when both widths are equal within 10%.  $^{147}\text{Sm}$  is a potential contributor to the overall  $^4\text{He}$  content of a given zircon grain, but

is commonly omitted from Monte Carlo simulations to increase computational efficacy (Hourigan et al., 2005). However,  $^{147}\text{Sm}$  is included in HeMP.

Zones are binned based on concentration values, up to the maximum of 20 allowed by HeMP. In most cases, nuclide zone boundaries are gradational. To increase simulation accuracy, these areas are binned into 1  $\mu\text{m}$  zones up and down gradient whenever possible. Concentric zonation was assumed for all grains, with no asymmetry and no inclusions.

Aliquot 08PA01-13 was used to evaluate the effects of changing parameters on the unique alpha-ejection correction. Iterations were run with drill rates of 1.7  $\mu\text{m/s}$  (artificially enhanced rate) and 0.6  $\mu\text{m/s}$  (true rate). Within these two groups of drill rates, geometry was varied from prisms with bi-pyramidal tips to prisms with pinacoidal tips. Some models were created using the three-dimensional knowledge of the grain and some were created assuming that both widths are equal. Results are shown in Table 3.

Bulk nuclide concentrations were calculated by radially weighting laser ablation measurements. The square radius was normalized to the equivalent spherical radius at the given radial position for each measurement. At each of these radial positions, the total spherical volume was calculated. The shell volume was then calculated by subtracting the spherical volume at every radial position  $n$  by the spherical volume at radial position  $(n-1)$ . The respective volumes were normalized from 0 (center) to 1 (rim) to create a weighting factor for the concentration

measurements. The weight factor was applied to the concentration measurements and summed to equal the total concentration.

## RESULTS

### *SEM-CL analyses*

Interpretations derived from SEM-CL imagery are not conclusive and not entirely quantitative. CL intensity is a relative quality resulting from imperfections in the zircon crystal lattice and has numerous causes including the following: presence of REE<sup>3+</sup> ions (esp. Dy<sup>3+</sup>), radiation damage (typically from U and Th), recrystallization, and hydrothermal alteration (Nasdala et al., 2003). The interplay of these imperfections can be difficult to determine, especially without the use of spectra and colored CL analyses. Nevertheless, CL imagery can provide a qualitative understanding of morphology, internal structures and textures, zonation type and zonation magnitude (see Corfu et al., 2003).

Zircons from 08PA01 have typically euhedral magmatic morphologies, with well-developed bi-pyramids, although some grains with nearly pinacoidal terminations were observed (Figure 5F) and some grains were cracked or broken. The grains often display complex to patchy zoning, but simple oscillatory growth zoning is not uncommon; few grains display sector zoning (Figure 5H). Low CL intensity inclusions are common and may be areas broken during polishing or a U-rich mineral phase, such as monazite.

Some zircons exhibit replacement textures that rim pre-metamorphic growth. Other grains have complex, zoned cores surrounded by concentric zones that are

frequently disrupted by alteration and resorption. Many grains have low-CL inclusions. Many grains are fractured, but rarely following a predictable pattern. Most interesting are the commonly observed rims with low intensity CL signal. The low intensity CL rims occur both on grains that have oscillatory zoning and those with complex or convolute zoning and probably indicate radiation damage from high-U concentration.

Sample 08PA71 exhibits similar morphology to 08PA01. Magmatic textures such as oscillatory zoning are frequently preserved and usually interrupted. Xenocrystic cores are common and sometimes cracked. Episodes of convolute zoning appear disturbed by extensive recrystallization textures and relict magmatic growth (Figure 6B). Grains rarely display homogeneous CL (Figure 6F); it is common to see bright or dim cores. CL quenched rims are frequently observed.

SEM-CL analyses from this study are in agreement with earlier imaging of gneissic zircons from Paros (Engel and Reischmann, 1998), as well as imaging performed prior to U-Pb analysis at University of Arizona (Bargnesi, Chapter 2).

#### *Abraded zircon (U-Th)/He analyses*

The results of the SEM-CL may indicate high-U rims, which could bias the alpha-ejection correction in typical Zircon (U-Th)/He analysis (ZHe). Therefore, mechanical abrasion was attempted to remove the enriched rim and any implanted helium. Results are shown in Table 1 and Figures 9 and 10. The abrasion rate varies widely from 0.1 to 1  $\mu\text{m/hr}$ . When estimating total abrasion, the minimum abrasion thickness, although conservative, is considered the most reliable for interpretation.



The relationship between abraded samples remains nearly identical if maximum, mean, or a statistical method is employed to determine the amount of abrasion. The minimum abrasion thickness is calculated by subtracting the post-abrasion width from the smallest pre-abrasion width which is greater than the post-abrasion width. The maximum abrasion thickness is calculated by subtracting the post-abrasion width from the largest pre-abrasion width. The mean abrasion thickness is the average of the minimum and maximum. The statistical method involves matching post-abrasion grains to pre-abrasion widths by a process of elimination. Whichever method is employed, the parabolic relationship between measured age and abraded thickness remains constant, where progressively abrading zircon width cause an increase, then decrease in the overall age (Figure 10). Some scatter in the data may be related to errors in estimating the amount abraded.

#### *LA-ICP-MS depth-profiled (U-Th)/He analyses*

The results indicate several different categories of parent nuclide distribution (Figure 3). The first is a distribution which does not cause the modeled ejection correction to deviate from the analytical correction. This may indicate a homogeneous parent nuclide distribution or a heterogeneous distribution which does not affect the correction, (i.e., complex, but balanced zonation). The second type is a zonation pattern which does cause the analytical ejection correction to deviate from the modeled correction. Within this second type are two subtypes: zonation patterns that result in an older modeled age and patterns that result in a younger modeled age. The existence of these categories attests to the exceptional diversity in zonation of the

samples. The overdispersion of the age data indicates that there may be other factors involved, such as inclusions and/or metamictization.

Three representative cases were used to assess the effectiveness and results of the modeling (Figures 9-11). Zircon grain 08PA01-13 is the “median” result – it has a 10 $\mu$ m, 10x U-Th enriched rim with respect to a homogeneous core (Figure 11). The presence of the rim does not dramatically change the age of the sample (about +6%, Table 2). This type of result was expected based on the CL imagery. The age increase is not dramatic, but it is nearly 2 $\sigma$  greater than the original age. It also brings the age of the grain closer to the mean AHe age, creating a dataset less problematic for interpretation (Bargnesi, Chapter 2). In general, grains which demonstrate this type of zonation are more likely to generate overdispersed data than to elicit a completely inaccurate tectonic interpretation.

Zircon 08PA71-16 illustrates the “too young” result in which the unmodeled age is younger than the true age (Figure 12). This grain has a 10 $\mu$ m rim that exhibits a nearly linear decrease from 25x to 5x U-Th enrichment (with respect to the core). The core is very homogeneous (Figure 12). In this case, helium retentivity will be significantly lower than estimated by a simple analytical alpha-ejection correction, resulting in an age that is far too young. By modeling this, we see a +29% change in the age. This increase brings the zircon age from 2 Ma younger than the mean AHe age to 0.6 Ma older than the AHe age (Figure 12).

Zircon 08PA71-20 illustrates the “too old” result, where the unmodeled age is older than the true age (Figure 13). In this case, the grain has a 15 $\mu$ m, 10x U-Th

depleted rim with respect to a very heterogeneous zircon interior. The highly enriched core generates much more helium than the depleted rims, and results in a much higher He retentivity than estimated by the analytical correction. By modeling the zonation, we see a -11% change in the age.

For sample 08PA01, the average change in ejection correction is about 8% and the average age bias about 12%. The maximum increase in age as a result of applying a modeled correction is ~28%, while the maximum decrease is ~1% (Figure 14, Table 2). The average drill rate is ~0.8  $\mu\text{m/s}$ , but varies from 0.6 to 1  $\mu\text{m/s}$ . For sample 08PA71 the average change in ejection correction is ~4% and the average age bias ~7%. The maximum increase in age is ~29% and the maximum decrease is ~11% (Figure 15, Table 2).

Several modeling iterations were performed for 08PA01-13 to better understand the limitations and effects of geometry, asymmetry, and binning of zones on the modeled alpha-ejection correction (Table 3). For this exercise, we consider the three-dimensional prism with tips and the highest zone bin resolution to be the optimal, or “true,” age from which all percentage differences are derived. The results indicate that an accurate drill rate is essential for an accurate alpha-ejection correction, though the interplay between drill rate, mass scanning speed and washout time of the laser ablation sample cell all contribute to what is resolvable. If the assumed drill rate is higher than the true drill rate, the zones will essentially become pinched together, and underestimate the size and impact of zones within 20 $\mu\text{m}$  from the edge of the crystal, whereas the opposite will occur if the assumed drill rate is

lower than the true drill rate. The results show that, if all other parameters remain identical, but the drill rate varies by  $1\mu\text{m/s}$ , the true age will be biased 4 – 7%. Modeling a grain as a prism with pinacoidal terminations rather than terminations will result in a bias of 2 – 3%. Binning in observed, discrete zones vs. continuous  $1\mu\text{m}$  binning may result in limitless bias proportional to what the user feels is appropriate. Here we note a difference of 0 – 2%.

It appears that agreement between concentrations measured by solution ICP-MS and LA-ICP-MS may indicate that extrapolation of the 1-D concentration array to 3-D is a reasonable assumption.

## **DISCUSSION**

### *Grain morphology and parent nuclide distribution*

There are some dramatic intra-sample variations in grain morphology. CL-imagery and binocular microscopy indicate asymmetric crystal face development and pronounced {010}-type planes in between typical tetragonal {100}-type faces. In some cases, only one or two of the {010} faces are developed resulting in pseudo-pentagonal (Figures 5C, 16) or pseudo-hexagonal morphometries. These multifaceted zircons possess more apices and vertices, which are zones of characteristically lower He retentivity (Hourigan et al., 2005).

Most of the zircons have well-developed bi-pyramids though some possess pinacoidal terminations (e.g., Figure 5F). These tip morphologies can be well-approximated by the bi-pyramidal model and will not significantly affect the final ejection-correction (Hourigan et al., 2005). The dominant grain populations display

typical magmatic morphologies, which indicates that an alpha-ejection correction that uses a tetragonal prism with bi-pyramidal terminations is appropriate. Unfortunately, for some grains, this correction will result in an age bias, but should not exceed ~2% (Hourigan et al., 2005).

Asymmetric zoning is an obstacle in obtaining accurate results from depth-profiling. CL-imagery indicates that growth of U-rich rims occurs preferentially along zircon tips rather than central width. In fact, zones tend to pinch out towards the middle of the grain, which may not be the ideal place to analyze depth-profiles (Figure 16). A possible approach would involve drilling profiles in the central width and tip of each grain, or polishing grains to half-width and rastering transects.

#### *Mechanically abraded zircon (U-Th)/He data*

In the case of enriched rims, an age which is “too young” is expected. As the U-Th enriched rim is abraded, the ingrown helium remains, resulting in a “too old” age (Figure 8). As the He enriched zone is abraded away, the age decreases, eventually reaching the true age. In the case of 08PA01, ~40 – 60µm of abrasion are required to reveal the true age of the sample. The natural zircons follow the expected trend (Figure 10). A decrease in age with increasing abraded thickness indicates that there is some degree of similarity of rim behavior in sample 08PA01.

The limitations of this technique are largely methodological. For instance, a sample must have enough zircons of similar size to perform a batch abrasion. The grains must also be large enough to survive ~60µm of mechanical abrasion, but not so large that the abrasion rate becomes prohibitive; a test batch indicates that grains

>120 $\mu\text{m}$  width demonstrate a threshold behavior and abraded at rates  $\ll 0.1\mu\text{m/hr}$ . Batch abrasion also assumes that the  $\text{width}_1$  and  $\text{width}_2$  dimensions are equal, while typical variations of 8 – 15% or greater are observed in the natural zircons. Another problem is that it is impossible to determine if a sufficient thickness has been abraded without performing single grain abrasion, which is precarious, as losing 10-30% of grains due to shattering during the process is common.

If the zoning is very complicated, the method could give mixed results. For instance, grains that are homogeneous before abrasion will still be homogeneous after abrasion. Grains with enriched rims or depleted rims may require different abrasion times that scale with the width of the rim. This may be problematic in cases of thick depleted rims (>30 $\mu\text{m}$ ), as the enriched U-Th core will be relatively depleted in He and insufficient abrasion will result in an age that is too young. If grains exhibit complex or patchy zoning abrasion may result in a different, yet still heterogeneous situation. For samples with variations that include multiple zonation patterns, such as 08PA71, there may be depleted rims on some grains and enriched rims on others. In this case, defining a single methodology for abrasion may be impossible. Ultimately, the (U-Th)/He age is required to make determinations on how well the technique is working and how to adjust the approach to obtain the correct age.

#### *Depth-profile controlled alpha-ejection corrections*

The application of modeling one dimensional concentration arrays to natural zircons is a useful method for correcting zircon (U-Th)/He results that are independently known to be problematic (e.g., by apatite fission track). This study

presents a dataset in which ZHe ages are consistently younger than AHe ages, suggesting systematic issues (Figure 3). Since the ZHe data are overdispersed and independent tectonothermal controls constrain cooling to ages older than the calculated ZHe age values, the problem was assumed to be with the zircons.

The extrapolation of one-dimensional concentration arrays to three-dimensional zonation models requires the assumption of concentric, symmetric zoning. The CL imagery and depth-profiles suggest that this is a faulty assumption in some cases. In the case of sample 08PA01, the assumption of homogeneous parent nuclide concentration results in alpha-ejection corrections that are ~8% too high, resulting in ages that are ~12% too young (Table 2). The resultant correction brings ZHe and AHe ages to roughly the same age, but does not fix the overdispersed ZHe ages. In addition, multiple iterations with individual parameter adjustments provide insight on how the correction will change and underscore the need for accurate drill rate measurements. The effects of geometry and zone bins are less important, attesting to the robustness of the calculation (Table 3). There is a potential test for the appropriateness of extrapolating a one-dimensional concentration array to three dimensional, which involves comparing the nuclide concentrations calculated during laser ablation to those obtained via solution ICP-MS. There appears to be a tentative correlation between age bias and uranium concentration, but more work is required to evaluate this test.

Results from custom alpha-ejection corrections show that although grain ages are apparently older than calculated by standard alpha-ejection corrections, the

corrections do not resolve the large spread between individual aliquot ages of the same sample. The largest inaccuracies in this method are probably related to uncertainty in the drill rate. Drill rate variations may be related to instrumental parameters, such as spontaneous fluctuation in fluence and defocussing with depth or more likely, changes in the crystalline integrity of each given zircon grain. . Another source of uncertainty is the measurement of pit depth by binocular microscopy. Since the tape mount method does not ensure that the c-axis is parallel to the laser-grain interface, oblique angle pits can result, and are difficult to measure. Variations in grain morphology can also result in pits that intersect {010}-type faces or, in the worst-case, a unique crystal face which lacks mirror symmetry (Figure 16). Additionally, internal structures can mask the location of the pit. Future work should ensure that the depth-profile is orthogonal to the c-axis and measure pit depth by laser interferometry.

## CONCLUSIONS

Since there is no current technique to visually comprehend the magnitude of parent heterogeneity in zircon grains, we recommend CL imagery as the first step towards understanding overdispersed or improbable (U-Th)/He data. SEM-CL works well for initial evaluations of elemental zonation in zircon and could be useful to map ideal depth-profile locations prior to laser ablation. Mechanical abrasion is a viable technique for confirming parent nuclide heterogeneity, but cannot normally correct for it alone. For abrasion to work successfully, all zircons would need to be true tetragonal prisms, possess enriched rims of constant thickness and have cores of



constant concentration, assumptions commonly violated by natural zircon. Overall, the method is logistically simple and more financially feasible than LA-ICP-MS depth-profiling, but works best if used in tandem with other techniques.

Zonation in natural zircon is the main limitation in obtaining accurate, precise ZHe data. We note that if the zonation is significant, relative age biases for a single sample can be  $\geq 40\%$ . This large of a bias is problematic for tectonic interpretations, which will be skewed if the weighted mean age is too low or too high. The older the individual grains are, the more pronounced the age bias will be.

Zonation can also cause overdispersion in ZHe data which are ejection-corrected assuming homogeneous parent nuclide distribution. Some samples, such as 08PA71, may have both highly enriched and highly depleted rims of different thickness and magnitude. Individual grains may also possess a concentration pattern that yields the correct age for the sample, meaning that each grains needs a unique correction and that batch correction *ex post facto* is not possible. Unfortunately, the current methodology does not resolve all scatter in the data, but future studies will address this matter.

Wide ranges in zircon morphology in a given sample will also impact the dispersion of (U-Th)/He data. This is especially true in analytical corrections which assume spherical or pinacoidal geometries for sample that display well-developed bi-pyramids. Samples which have been subjected to intense metamorphism can display unusual morphologies and prism growths which have not been discussed with respect to ejection-correction.

This work represents a fundamental step forward in refining (U-Th)/He and correcting biases in measured ages as a result of compositional heterogeneities. Future work should focus on creating the most realistic alpha-ejection corrections possible for individual grains. This may include expanding geometrically possible simulations and detailed parent nuclide concentration mapping in two or three dimensions.

### CHAPTER 3: REFERENCES

- Avigad, D., 1998. High-pressure metamorphism and cooling on SE Naxos (Cyclades, Greece). *European Journal of Mineralogy*. 10, 1309–1319.
- Braun, J., 2002. Quantifying the effect of recent relief changes on age-elevation relationships. *Earth and Planetary Science Letters*. 200, 331–343.
- Brichau, S., Ring, U., Ketcham, R.A., Carter, A., Stockli, D., Brunel, M., 2006. Constraining the long-term evolution of the slip rate for a major extensional fault system in the central Aegean, Greece, using thermochronology. *Earth and Planetary Science Letters*. 241, 293–306.
- Brown, R.W., 1991. Backstacking apatite fission-track “stratigraphy”: A method for resolving the erosional and isostatic rebounded components of tectonic uplift histories. *Geology*. 19, 74–77.
- Cherniak, D.J., Watson, E.B., Thomas, J.B., 2009. Helium diffusion in apatite and zircon. *Chemical Geology*. 10.1016/j.chemgeo.2009.08.011.
- Corfu, F., Hanchar, J.M., Hoskin, P.W.O., Kinny, P., 2003. Atlas of zircon textures, in: Hanchar, J.M., Hoskin, P.W.O. (Eds.), *Zircon. Reviews in Mineralogy and Geochemistry*. 53, 468–500
- Dobson, K.J., Stuart, F.M., Dempster, T.J., EIMF, 2008. U and Th zonation in Fish Canyon Tuff zircons: Implications for a zircon (U-Th)/He standard. *Geochimica et Cosmochimica Acta*. 72, 4745–4755.
- Ehlers, T.A., Willett, S.D., Armstrong, P.A., Chapman, D.S., 2003. Exhumation of the central Isatch Mountains, Utah: 2. Thermokinematic model of exhumation,

- erosion, and thermochronometer interpretation. *Journal of Geophysical Research*. 108, 10.1029/2001JB001723.
- Engel, M., Reischmann, T., 1998. Single Zircon Geochronology of orthogneisses from Paros, Greece: *Bulletin of the Geological Society of Greece*. 32, 91–99.
- Farley, K.A., Wolf, R.W., Silver, L.T., 1996. The effects of long alpha-stopping distances on (U-Th)/He ages. *Geochimica et Cosmochimica Acta*. 60, 4223–4229.
- Farley, K.A., 2002. (U-Th)/He dating: techniques, calibrations and applications, in: Porcelli, D., Ballentine, C.J., Wieler, R. (Eds.), *Noble Gases in Geochemistry and Cosmochemistry*. *Reviews in Mineralogy and Geochemistry*. 47, 819–843.
- Farley, K.A., 2007. He diffusion systematic in minerals: evidence from synthetic monazite and zircon structure phosphates. *Geochimica et Cosmochimica Acta*. 71, 4015–4024.
- Flowers, R.M., Shuster, D.L., Wernicke, B.P., Farley, K.A., 2007. Radiation damage control on apatite (U-Th)/He dates from the Grand Canyon region, Colorado Plateau. *Geology*. 35, 447–450.
- Flowers, R.M., Ketcham, R.A., Shuster, D.L., Farley, K.A., 2009. Apatite (U-Th)/He thermochronometry using a radiation damage accumulation and annealing model. *Geochimica et Cosmochimica Acta*. 73, 2347–2365.
- Hager, C., Stockli, D.F., 2009. A new Matlab©-based Helium Modeling Package (“HeMP”) for thermal history recovery from single and multi-

- thermochronometer (U–Th)/He data and data arrays. Geological Society of America Abstracts with Programs. 41, 487.
- Hourigan, J.K., Reiners, P.W., Brandon, M.T., 2005. U-Th zonation-dependent alpha-ejection in (U-Th)/He chronometry. *Geochimica et Cosmochimica Acta*. 69, 3349–3365.
- John, B.E., Howard, K.A., 1995. Rapid extension recorded by cooling-age patterns and brittle deformation, Naxos, Greece. *Journal of Geophysical Research*. 100, 9969–9979.
- Krogh, T.E., 1982. Improved accuracy of U-Pb zircon ages by the creation of more concordant systems using an air abrasion technique. *Geochimica et Cosmochimica Acta*. 46, 637–649.
- Lovera, O.M., Richter, R.M., Harrison, T.M., 1989. The  $^{40}\text{Ar}/^{39}\text{Ar}$  thermochronometry for slowly cooled samples having a distribution of diffusion domain sizes. *Journal of Geophysical Research*. 94, 17917–17935.
- Marsellos, A.E., Garver, J.I., 2010. Radiation damage and uranium concentration in zircon as assessed by Raman spectroscopy and neutron irradiation. *American Mineralogist*. 95, 1192–1201.
- Meesters, A.G.C.A., Dunai, T.J., 2002. Solving the production-diffusion equation for finite diffusion domains of various shapes: Part II. Application to cases with alpha-ejection and nonhomogeneous distribution of the source. *Chemical Geology*. 186, 57–73.

- Nasdala, L., Wenzel, M., Vavra, G., Irmer, G., Wenzel, T., Kober, B., 2001. Metamictisation of natural zircon: accumulation versus thermal annealing of radioactivity-induced damage. *Contributions to Mineralogy and Petrology*. 141, 125–144.
- Nasdala, L., Reiners, P.W., Garver, J.I., Kennedy, A.K., Stern, T.A., Balan, E., Wirth, R., 2004. Incomplete retention of radiation damage in zircon from Sri Lanka. *American Mineralogist*. 89, 219–231.
- Nasdala, L., Grambole, D., Götze, J., Kempe, U., Váczi, T., 2010. Helium irradiation study on zircon. *Contributions to Mineralogy and Petrology*. 10.1007/s00410-010-0562-7.
- Papanikolaou, D., 1996. Geological Map of Paros. IGME.
- Putlitz, B., Cosca, M.A., Schumacher, J.C., 2005. Prograde mica  $^{40}\text{Ar}/^{39}\text{Ar}$  growth ages recorded in high pressure rocks (Syros, Cyclades, Greece). *Chemical Geology*. 214, 79–98.
- Reiners, P.W., Spell, T.L., Nicolescu, S., Zanetti, K.A., 2004. Zircon (U-Th)/He Thermochronometry: He diffusion and comparisons with  $^{40}\text{Ar}/^{39}\text{Ar}$  dating. *Geochimica et Cosmochimica Acta*. 68, 1857–1887.
- Reiners, P.W., Ehlers, T.A. (Eds.), 2005. Low-temperature Thermochronology: Techniques, Interpretations, and Applications. *Reviews in Mineralogy and Geochemistry*. 58, pp. 622.

- Shuster, D.L., Flowers, R.M., Farley, K.A., 2006. The influence of natural radiation damage on helium diffusion kinetics in apatite. *Earth and Planetary Science Letters*. 249, 148–161.
- Tomaschek, F., Kennedy, A.K., Villa, I.M., Lagos, M., Ballhaus C., 2003. Zircons from Syros, Cyclades, Greece: recrystallization and mobilization of zircon during high-pressure metamorphism. *Journal of Petrology*. 44, 1977–2002.
- Watson, E.B., Wanser, K.H., Farley, K.A., 2010. Anisotropic diffusion in a finite cylinder, with geochemical applications. *Geochimica et Cosmochimica Acta*. 74, 614–633.
- Wolf, R.A., Farley, K.A., Silver, L.T., 1996. Helium diffusion and low temperature thermochronometry of apatite. *Geochimica et Cosmochimica Acta*. 60, 4231–4240.

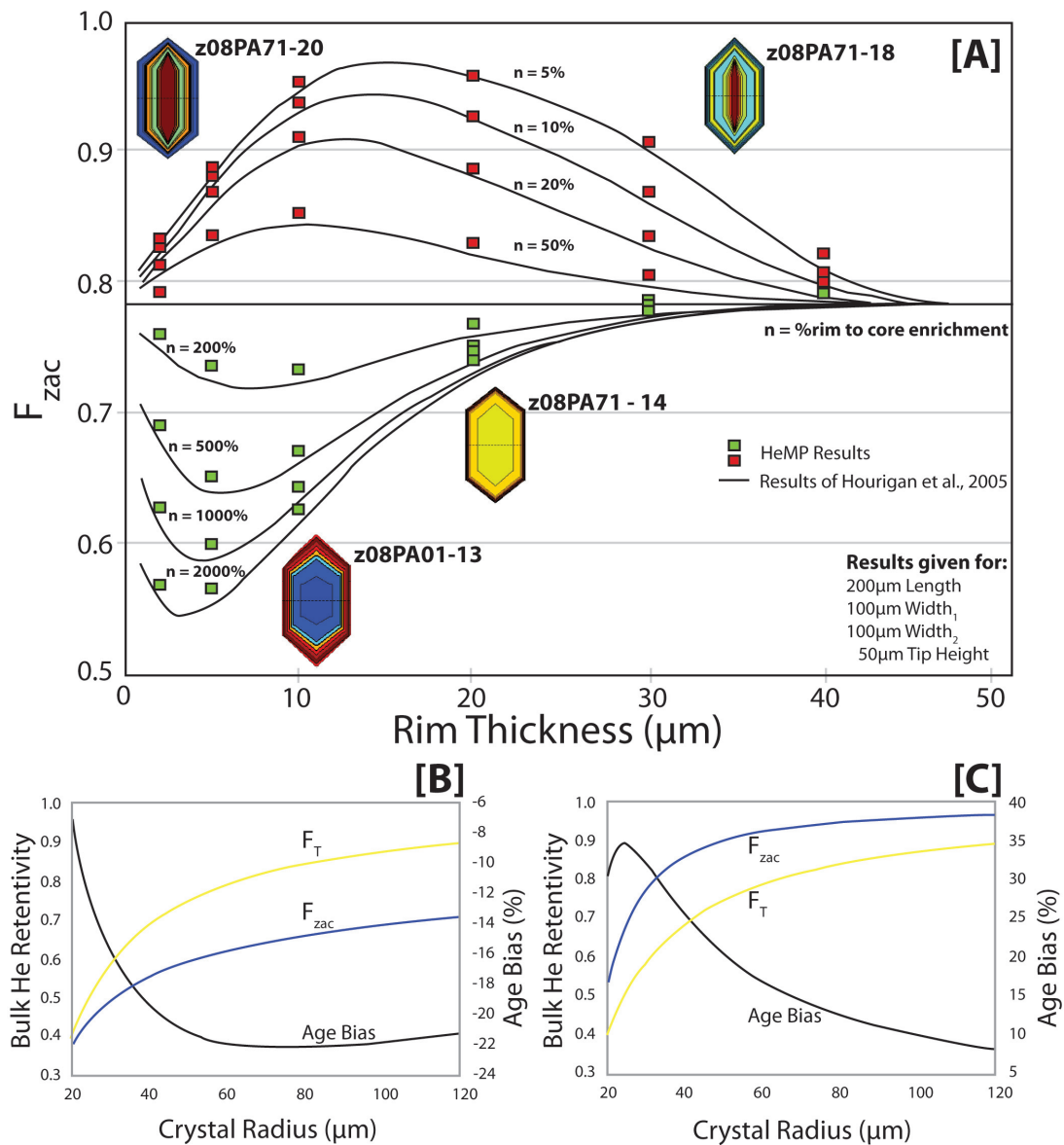




**Figure 1.** [A] Comparison of age bias with enriched or depleted rims based on rim position and differential concentration (modified from Hourigan et al., 2005). The plot show how HeMP compares with work from Hourigan and others (2005). [B] Plots showing how age bias varies with crystal size (modified from Hourigan et al., 2005). A series of plots taken from Hourigan et al., 2005 which illustrate how the alpha-ejection correction changes with relative concentration variations in zircon as well as the difference between modeled and analytical solution to the correction. The figure also shows how age bias changes with various concentrations.

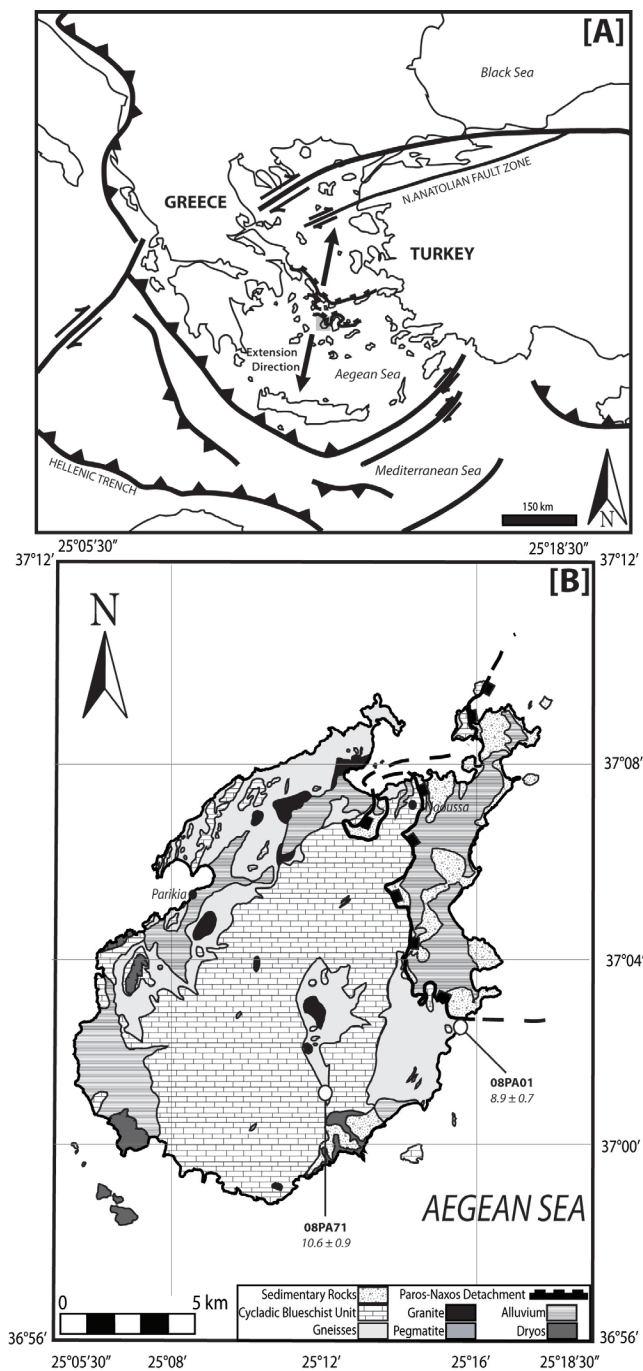


**Figure 2.** [A] Simplified regional tectonic map for the greater Aegean region (from Bargnesi, Chapter 2). The central Aegean experienced HP metamorphism ~50 Ma (Tomaschek, 2003; Putlitz, 2005; etc.) and subsequent Barrovian overprinting in the Miocene (Bargnesi, Chapter 2). [B] Simplified geologic map of the island of Paros (modified from Papanikolaou, 1996). The dominant structural feature is the low-angle Paros-Naxos extensional detachment fault which has juxtaposed the high-grade metamorphic core complex against completely unmetamorphosed sedimentary rocks in the Paros supradetachment basin. The footwall comprises Variscan gneisses (Engel and Reischmann, 1998; Bargnesi, Chapter 2) from which the two samples for this study were taken, as well as marbles, amphibolites and amphibolite schists of the overprinted Cycladic Blueschist Unit. The italic number underneath the sample name is the mean ZHe age with 8% ( $2\sigma$ ) error.

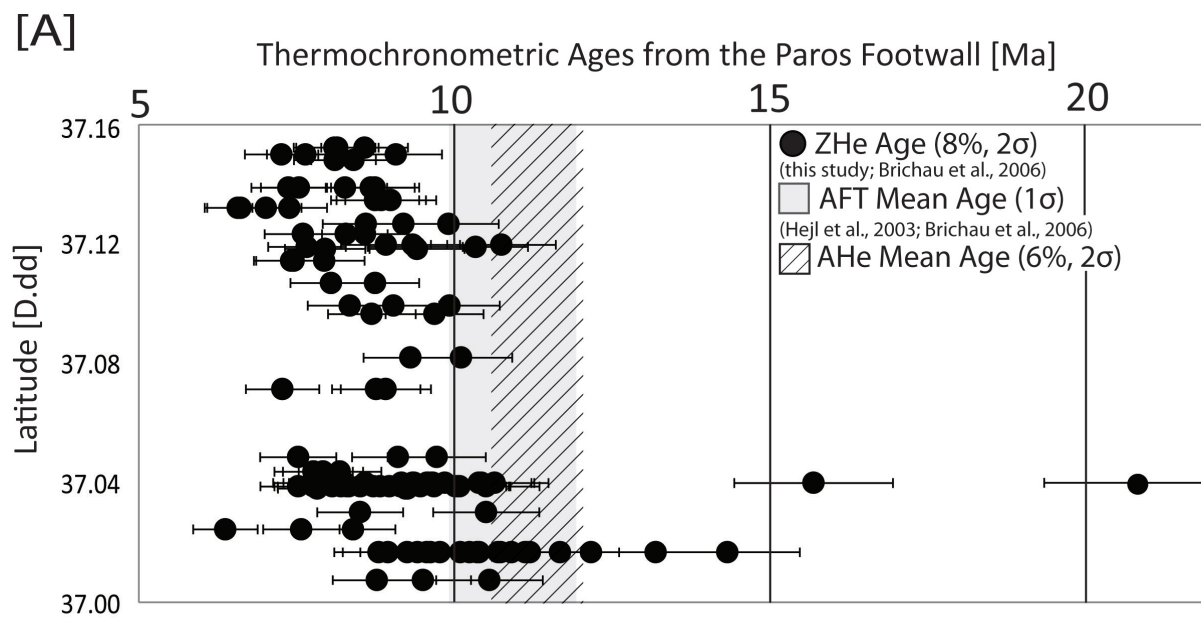


**Figure 3.** [A] Results from thermochronometric analysis of the Paros footwall (from Bargnesi, Chapter 2). Age is plotted against latitude as a useful proxy for distance from the detachment fault, since the position of the fault offshore is not known and extension has been roughly N-S. The plot illustrates the problem addressed in this study, which is that apatite (U-Th)/He ages and apatite fission track (AFT) ages are apparently older than zircon (U-Th)/He ages. [B] Orthogneiss outcrop on Paros at 37.11833, 25.20306. Hammer in lower left is ~30cm tall.

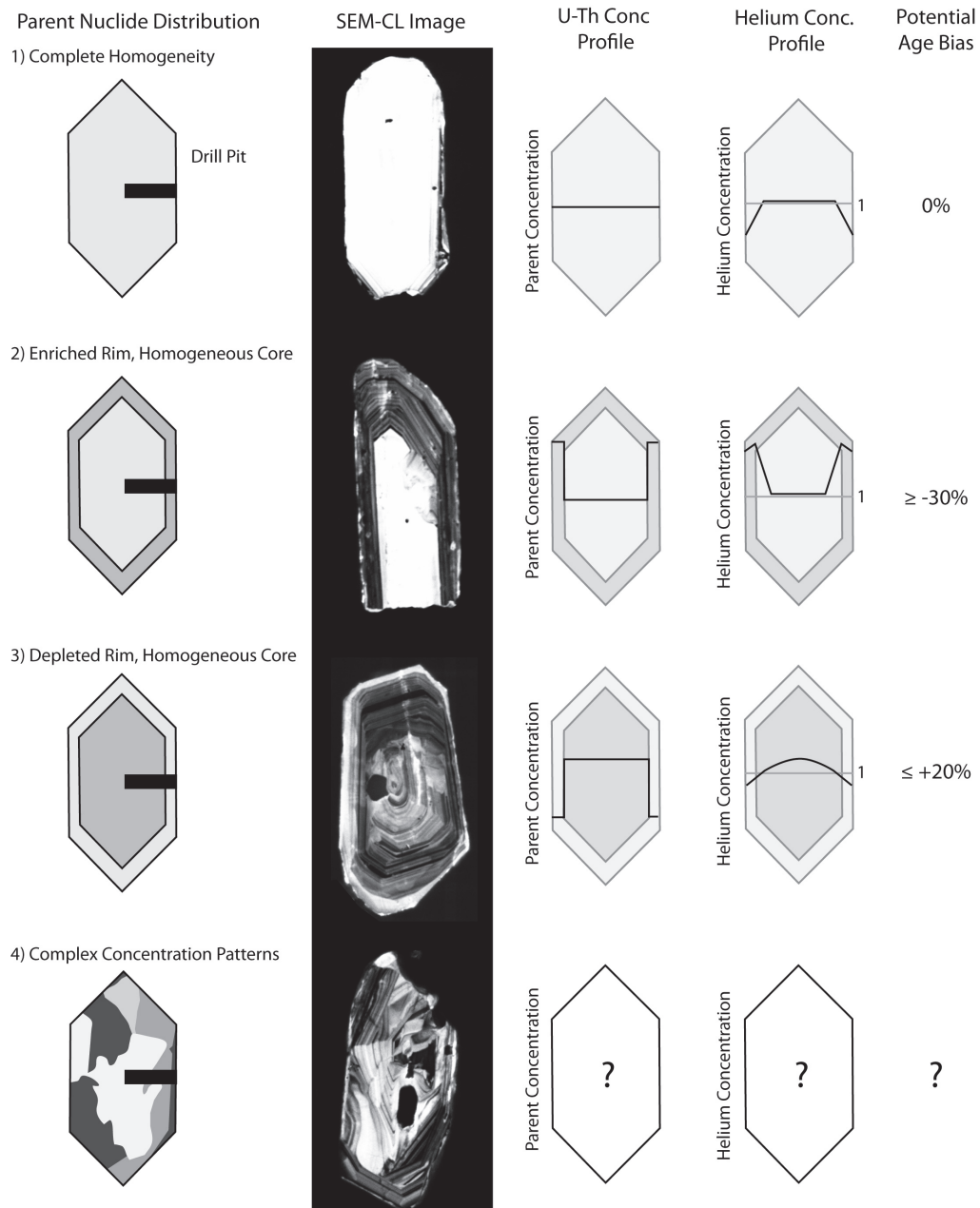


**Figure 4.** Different zonation scenarios illustrated with [A] a schematic representation of parent nuclide distribution, [B] a representative CL image, [C] the relative rim to core concentrations of U, Th, and [D] He, and [E] the potential age bias resulting from the given scenario. There are four possible types of parent zonation: [1] Complete parent nuclide homogeneity, [2] Enriched rims and homogeneous core, [3] Depleted rim and homogeneous core, and [4] Chaotic zonation. See text for discussion. Nuclide concentration profiles are qualitative and used here only to illustrate the effects of zoning.

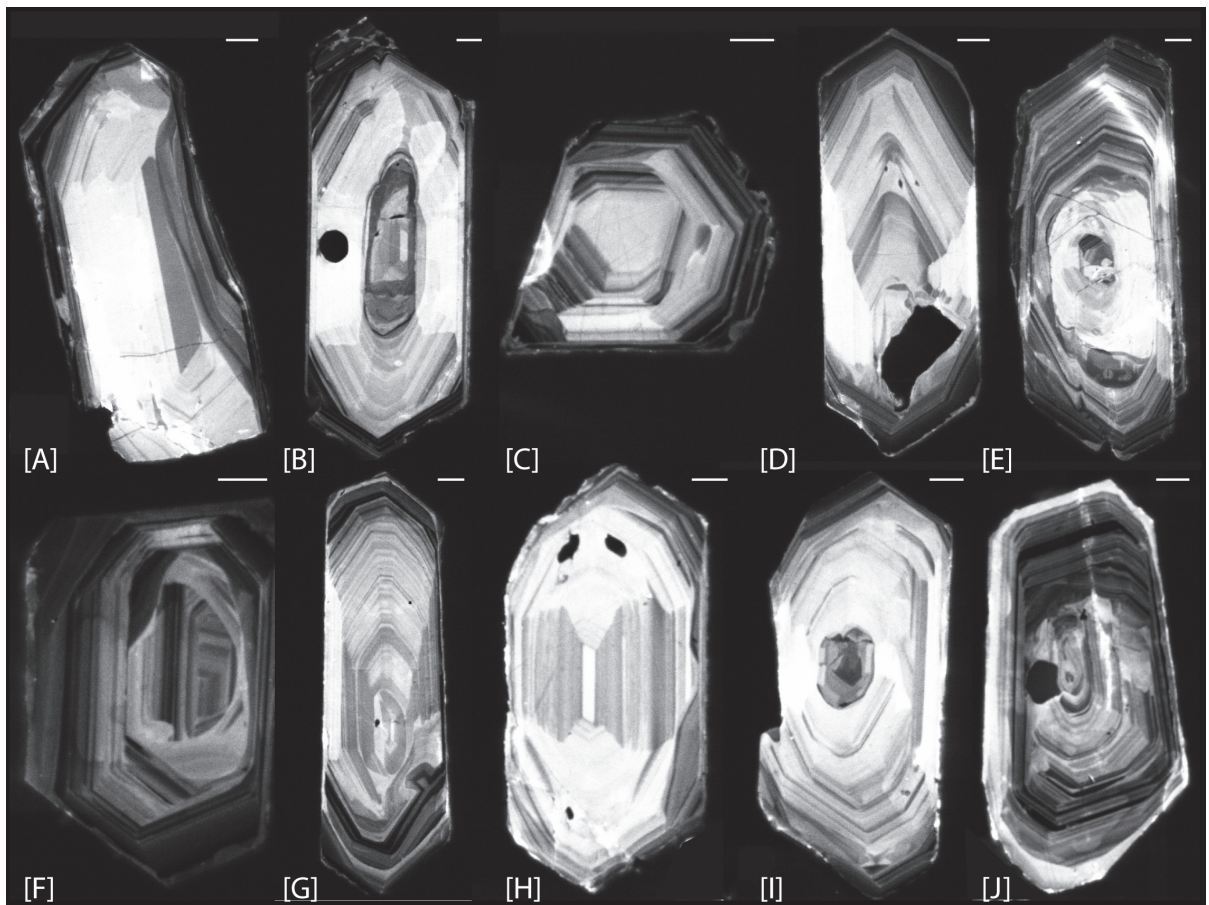




**Figure 5.** Scanning electron microscopy cathodoluminescence (SEM-CL) imagery from sample 08PA01. A color-neutral CL detector was used. The white scale bars are 20  $\mu\text{m}$ ; images were taken at a variety of magnifications. The images provide a qualitative proxy for parent nuclide zonation. CL-quenched zones indicate areas of lower crystallinity relative to surrounding areas and therefore higher radioactivity, probably as a result of increased U and Th concentrations. The CL-intense zones indicate the opposite. These images indicate a complex growth history for the zircons of 08PA01, including periods of asymmetric growth and incorporation of monazite inclusions (black areas). Oscillatory zoning is common, although chaotic zoning and sector zoning can also be observed. There are a number of overgrowth and recrystallization textures at the rims as well as inherited cores. These types of zircon are not ideal for (U-Th)/He analyses, which are corrected using a statistical method that assumes a homogenous distribution of parent nuclides in the host crystal.

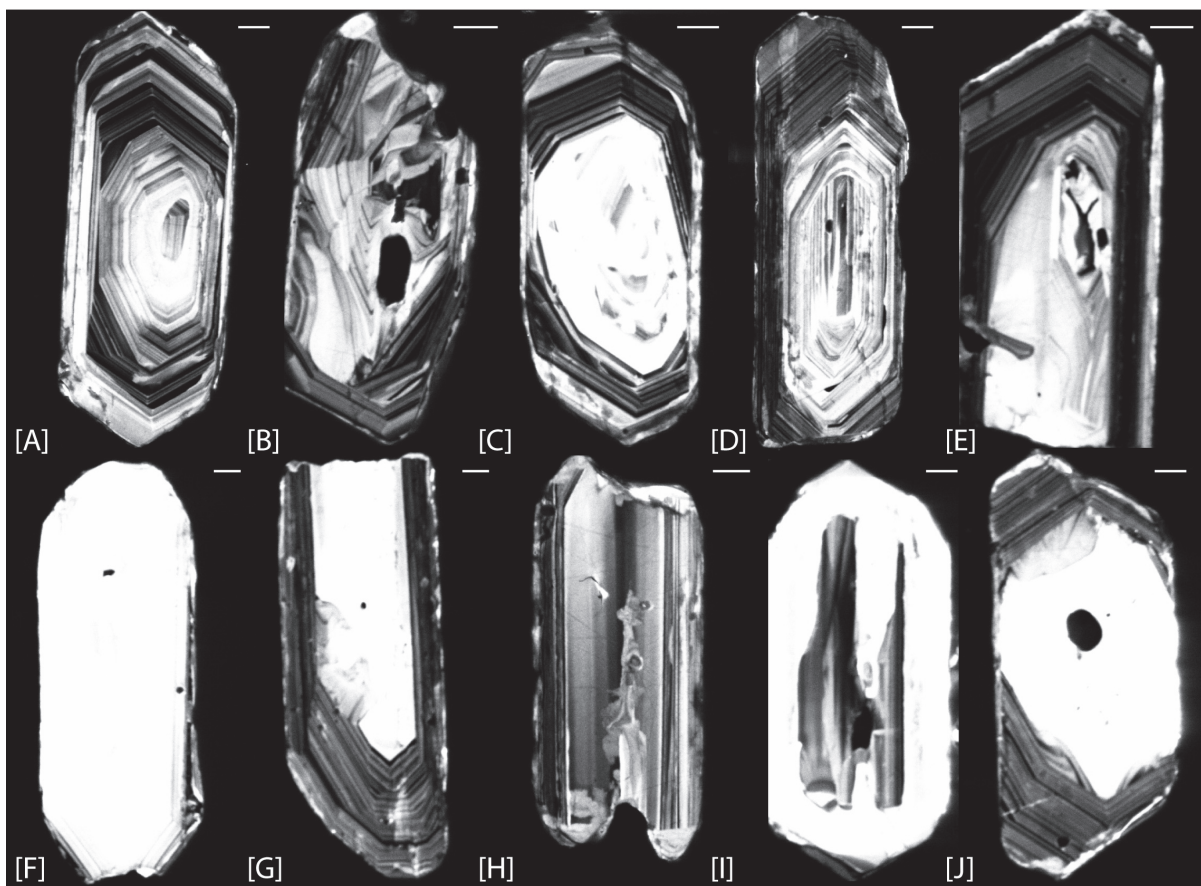


**Figure 6.** Scanning electron microscopy cathodoluminescence (SEM-CL) imagery from sample 08PA71. A color-neutral CL detector was used. The white scale bar is 20  $\mu\text{m}$ ; images were taken at a variety of magnifications. These images indicate a complex growth history for the zircons similar to that of 08PA01, including periods of asymmetric growth and incorporation of monazite inclusions (black areas). Oscillatory zoning is common, although chaotic zoning can also be observed. There are a number of overgrowth and recrystallization textures at the rims as well as inherited cores. These types of zircon are not ideal for (U-Th)/He analyses, which are corrected using a statistical method that assumes a homogenous distribution of parent nuclides in the host crystal.

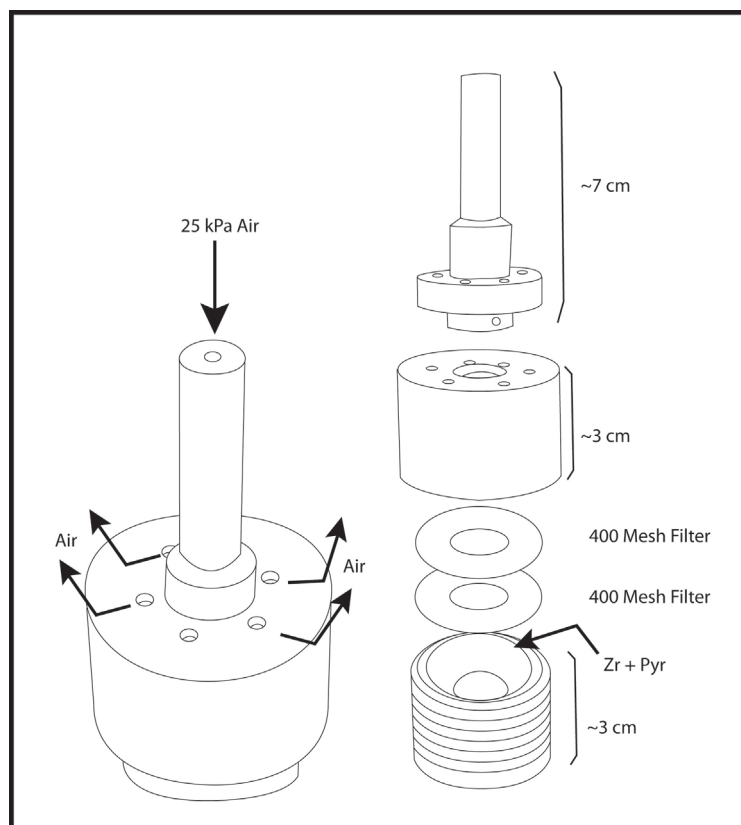


**Figure 7.** Schematic diagram of a stainless steel vessel used for air abrasion. The vessel attaches to an air compressor which is regulated to 25 kPa of pressure. The vessels are filled with low-U pyrite and 10 - 20 zircon grains of similar width. The air circulates into the vessel, causing pyrite to mediate grain-grain collisions during mechanical reduction in grain volume. To separate zircon from pyrite, a 7N HNO<sub>3</sub> heat bath was used. See text for full methodology. Photographs of grains are shown in Figure 9 and results are given in Figure 10 and Table 1.

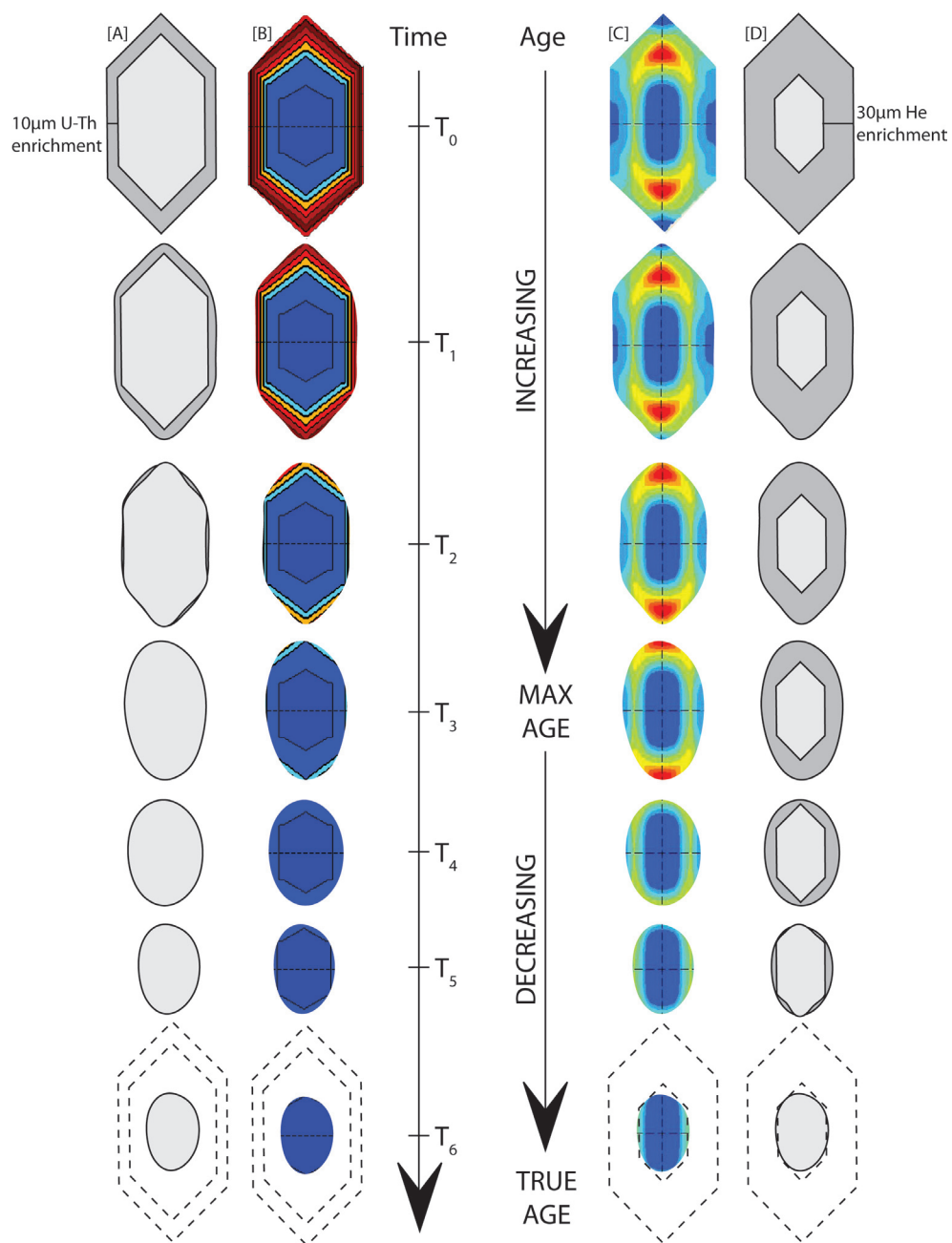


**Figure 8.** Schematic illustrating how zircon grains with 10 $\mu$ m thick U-Th enriched rims are abraded. Schematic diagrams of [A] U,Th, and [D] He enriched zones are shown alongside representative aliquot 08PA01-13, which exhibits [B] a 10 $\mu$ m thick U-Th enriched rim (complete depth profile in Figure 11) and [C] a corresponding 30 $\mu$ m thick He enriched rim. Because the stopping distance of alpha particles in zircon are 15 - 20 $\mu$ m (Farley et al., 1996), a 10 $\mu$ m thick U-Th enriched rim will implant helium into the grain resulting in a 30 $\mu$ m helium-enriched rim. To obtain a true corrected age, the rim and corresponding helium must be abraded away and the remaining core must have homogeneous distributions of U, Th, and He. The age will increase as U and Th are removed, but implanted helium remains. Age the implanted helium is removed the age will begin to decrease until homogeneous concentrations of U, Th, and He are present and the true age is obtained (experimental results in Figure 10).

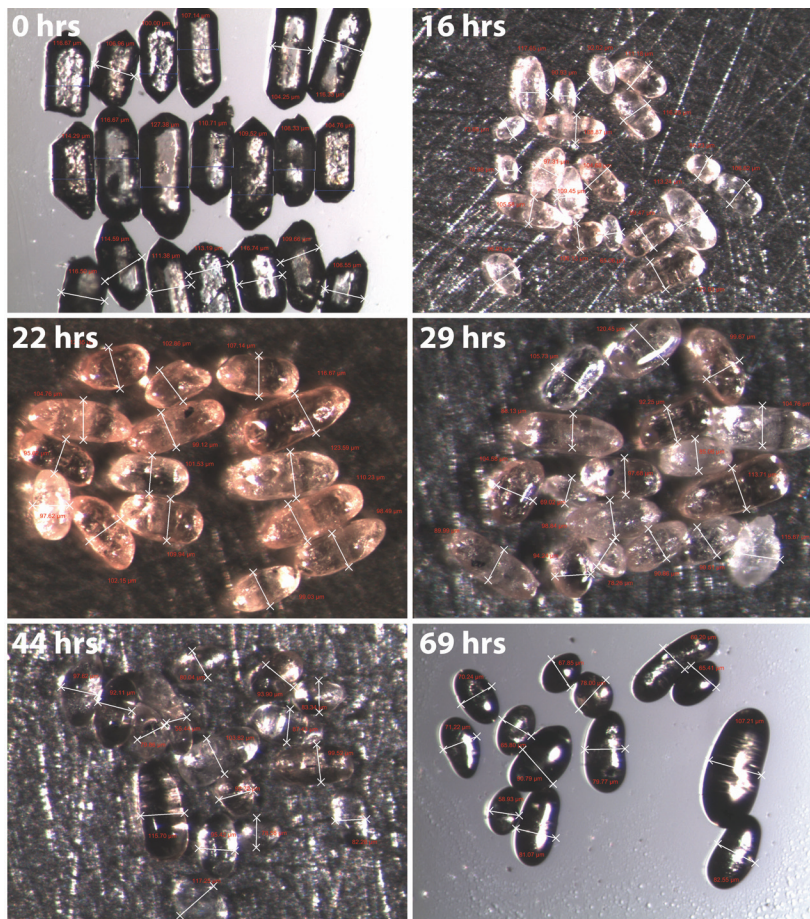




**Figure 9.** Photographic history illustrating progressive abrasion of zircon grains from sample 08PA01. 20 grains were handpicked to have uniform width. Grains did not abrade evenly (Table 1), probably as result of lattice heterogeneities (i.e., inclusions, zonation, radiation damage) and the cubic dependence of volume on crystal radius.

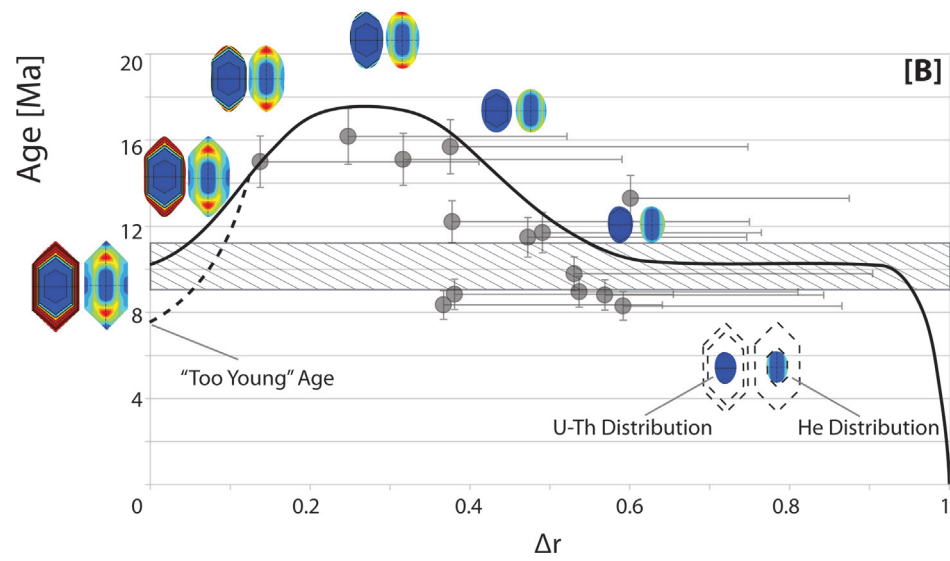
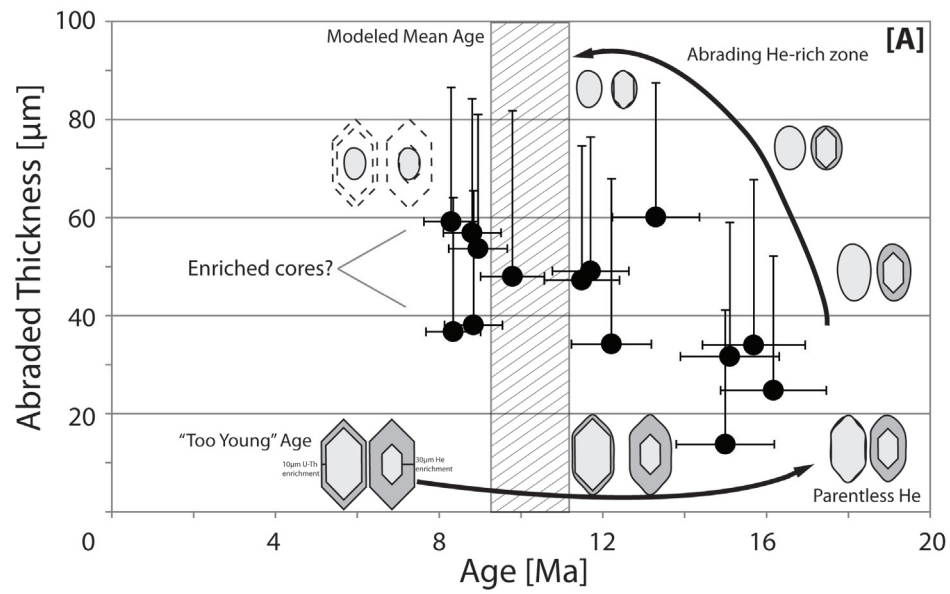


**Figure 10.** [A] Results from mechanically abraded zircon (U-Th)/He ages from sample 08PA01. Plot shows age vs. minimum abrasion thickness. Error bars are 8% ( $2\sigma$ ) for ZHe ages. Vertical error bars are shown to illustrate the possible abrasion thicknesses for each individual grain, from the minimum to the maximum. Since batch abrasion was used, the true abraded thickness is not known. Grains show a linear relationship between increasing abrasion thickness and decreasing age. Scatter in the data is probably related to heterogeneities in concentration, especially U-Th enriched cores. Another source of scatter may be related to the incidental abrasion of fragments, which appear to be abraded heavily, but are actually broken off of a larger grain. [B] Age plotted against change in grain radius. Abraded evolution is shown with representative HeMP zonation models from Figures 7 and 11 that show what how differential concentrations affect a given age. The relationship is parabolic. The dark line shows the expected trend of age with  $\Delta r$ . The hatchured box shows the “true” modeled age for 08PA01 (see Figure 14). The resultatnt “too young” ages are probably due to enriched cores.

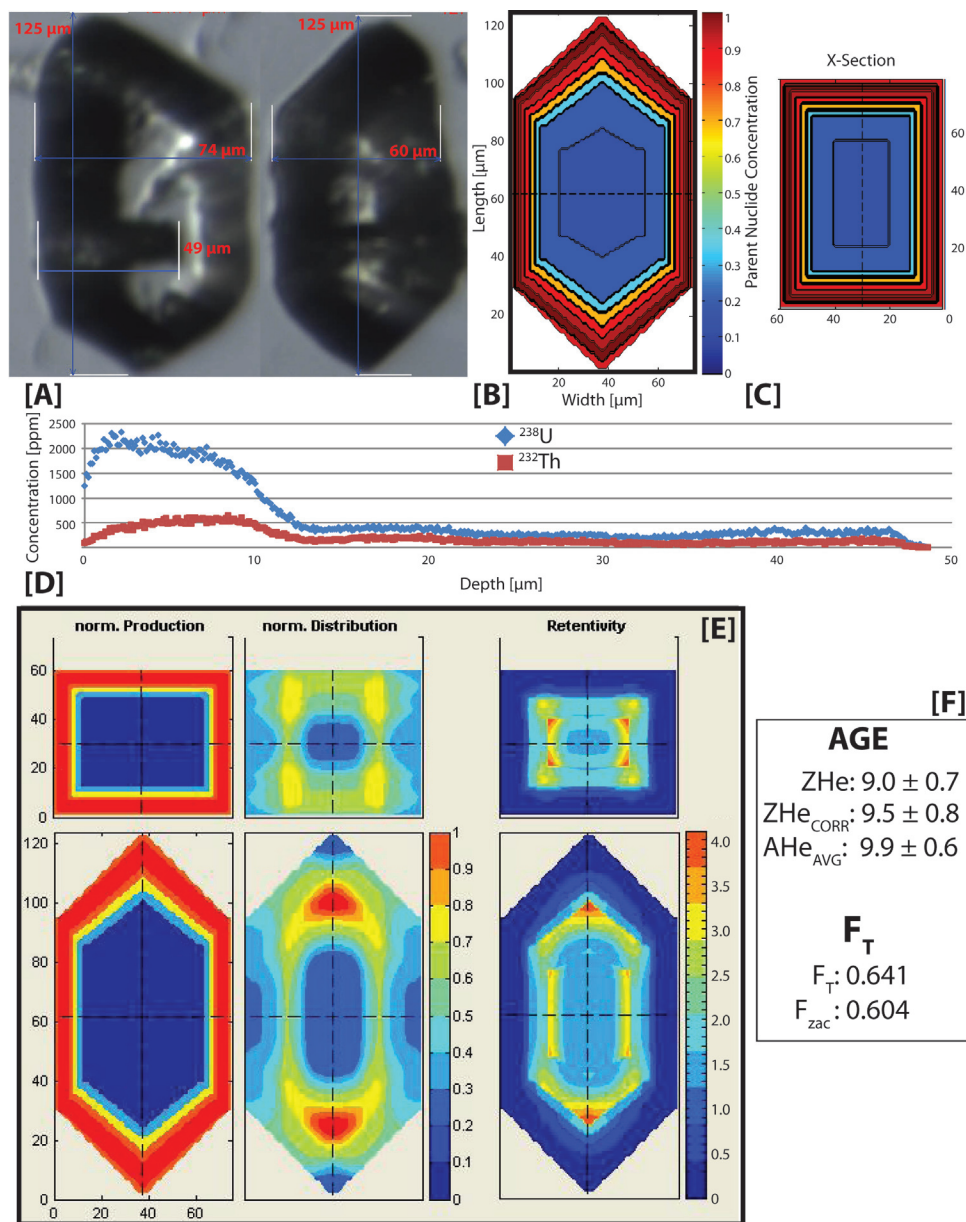


**Figure 11.** Aliquot 08PA01-13 shown here with photographs of [A] the grain and drill pit dimensions, [B] the modeled parent nuclide zonation scheme parallel to the c-axis, [C] orthogonal to the c-axis, [D] the depth-profile, [E] the results of modeling (see below) and [F] the impact on the alpha-ejection correction and age. Photographs were taken on a binocular microscope and show width<sub>1</sub> and width<sub>2</sub>. The modeled zonation scheme was created using HeMP with 2μm bins based on the concentration profile. The concentration profile is shown with ppm of <sup>238</sup>U and <sup>232</sup>Th vs. depth into the grain. A 10μm rim enriched ~4x from the very homogeneous core is observed. The results from the modeling show the normalized He production in the grain, normalized He distribution and relative He retentivity. The box on the right shows the effects of modeling on the age and alpha-ejection correction. This aliquot represents what is considered the “mean” case, where enriched rims are present, but the effect of modeling the alpha-ejection correction on the age is minimal.

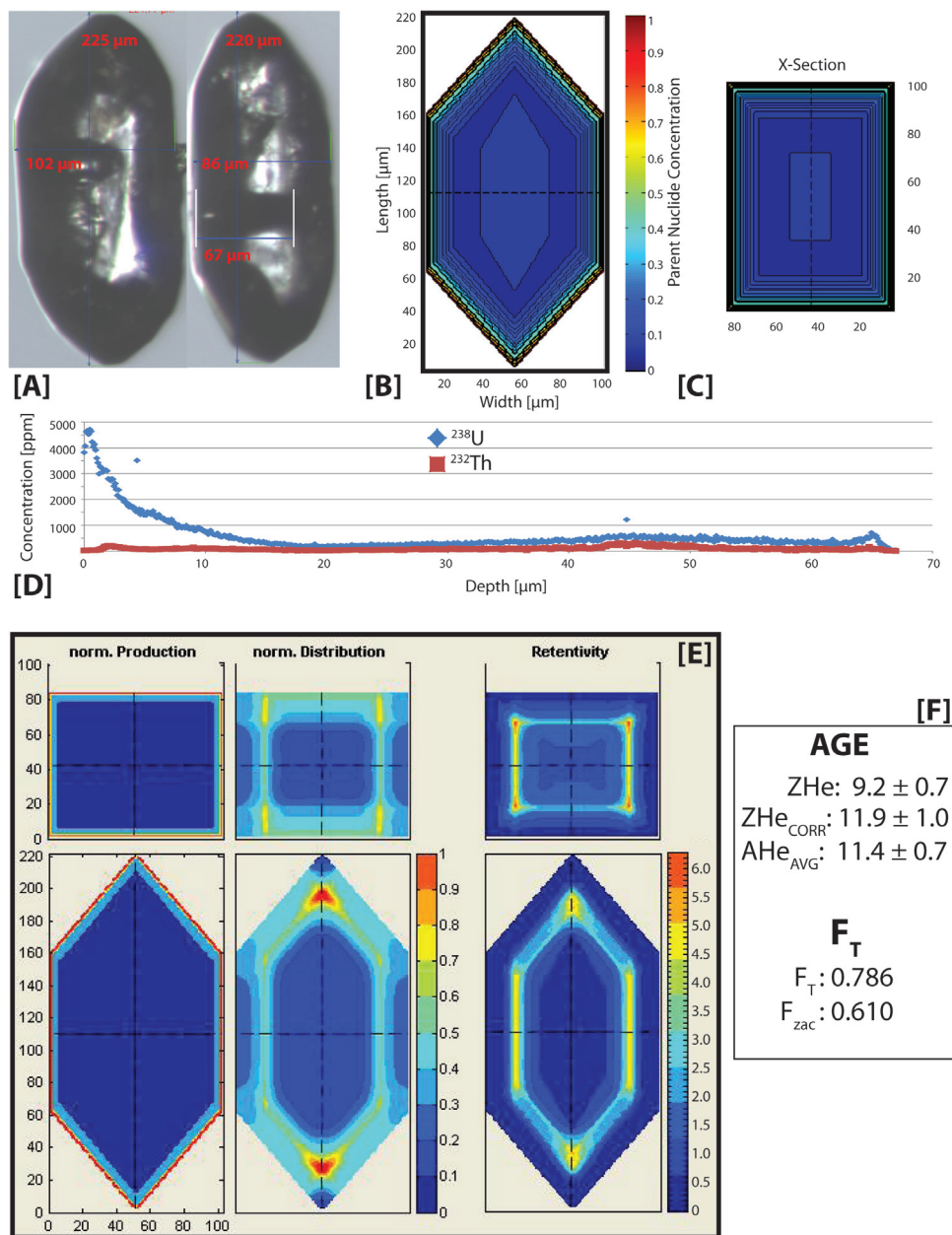


**Figure 12.** Aliquot 08PA71-16 shown here with photographs of [A] the grain and drill pit dimensions, [B] the modeled parent nuclide zonation scheme parallel to the c-axis, [C] orthogonal to the c-axis, [D] the depth-profile, [E] the results of modeling (see below) and [F] the impact on the alpha-ejection correction and age. Photographs were taken on a binocular microscope and show width<sub>1</sub> and width<sub>2</sub>. The modeled zonation scheme was created using HeMP with various sized bins based on the concentration profile. The concentration profile is shown with ppm of <sup>238</sup>U and <sup>232</sup>Th vs. depth into the grain. A 10µm rim with a linear decrease from 20x to 2x with respect to the homogeneous core is observed. The results from the modeling show the normalized He production in the grain, normalized He distribution and relative He retentivity. The box on the right shows the effects of modeling on the age and alpha-ejection correction. This is aliquot represents “too young” case, where strongly enriched rims are present and modeling the alpha-ejection correction increases the age dramatically, ~29% in this case.

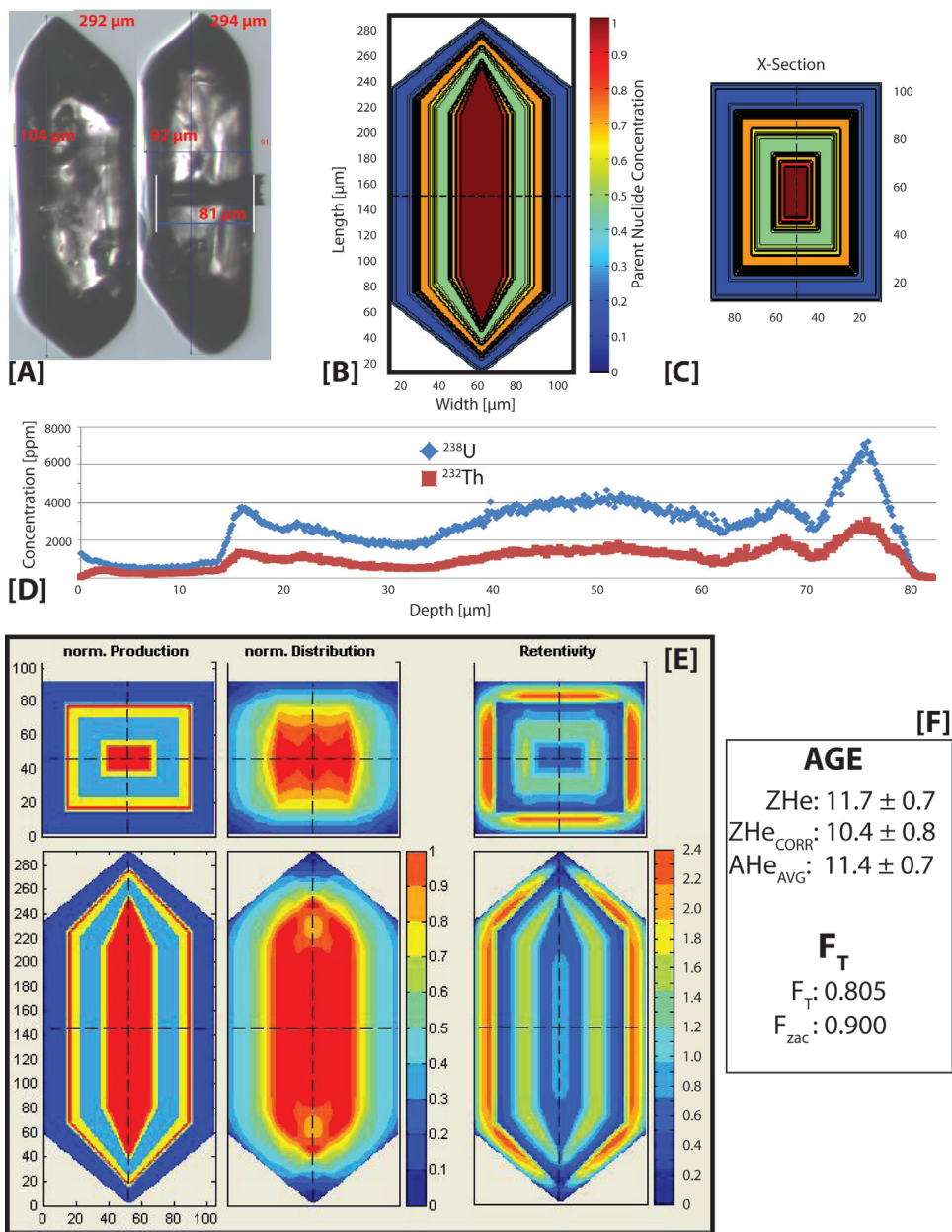




**Figure 13.** Aliquot 08PA71-20 shown here with photographs of [A] the grain and drill pit dimensions, [B] the modeled parent nuclide zonation scheme parallel to the c-axis, [C] orthogonal to the c-axis, [D] the depth-profile, [E] the results of modeling (see below) and [F] the impact on the alpha-ejection correction and age. Photographs were taken on a binocular microscope and show width<sub>1</sub> and width<sub>2</sub>. The modeled zonation scheme was created using HeMP with various sized bins based on the concentration profile. The concentration profile is shown with ppm of <sup>238</sup>U and <sup>232</sup>Th vs. depth into the grain. A 15μm rim depleted 4x with respect to a somewhat heterogeneous core is observed. The results from the modeling show the normalized He production in the grain, normalized He distribution and relative He retentivity. The box on the right shows the effects of modeling on the age and alpha-ejection correction. This aliquot represents the “too old” case, where strongly depleted rims are present and the age decreases; ~11% in this case.

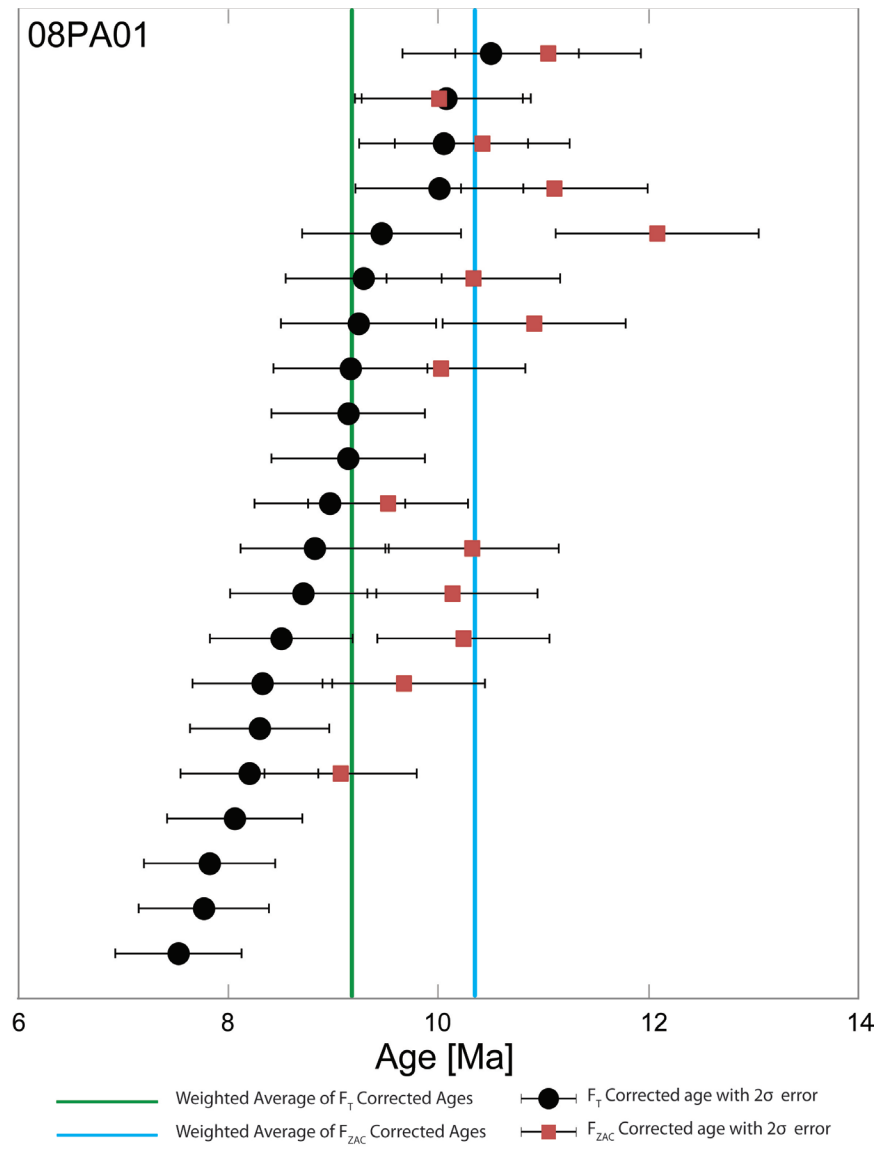


**Figure 14.** Results of the depth-profiled corrections for sample 08PA01. The plot shows the zircon aliquots with a normal alpha-ejection correction (black circles) and if possible, the same aliquot with a unique alpha-ejection correction (red squares). The green line shows the weighted mean age for the normally corrected ages and the blue line shows the weighted mean age for the uniquely corrected ages. The difference between weighted mean ages is about +13%. Note that corrected ages are typically older than uncorrected ages, indicating some degree of homogeneity among zonation types in the zircons of 08PA01.

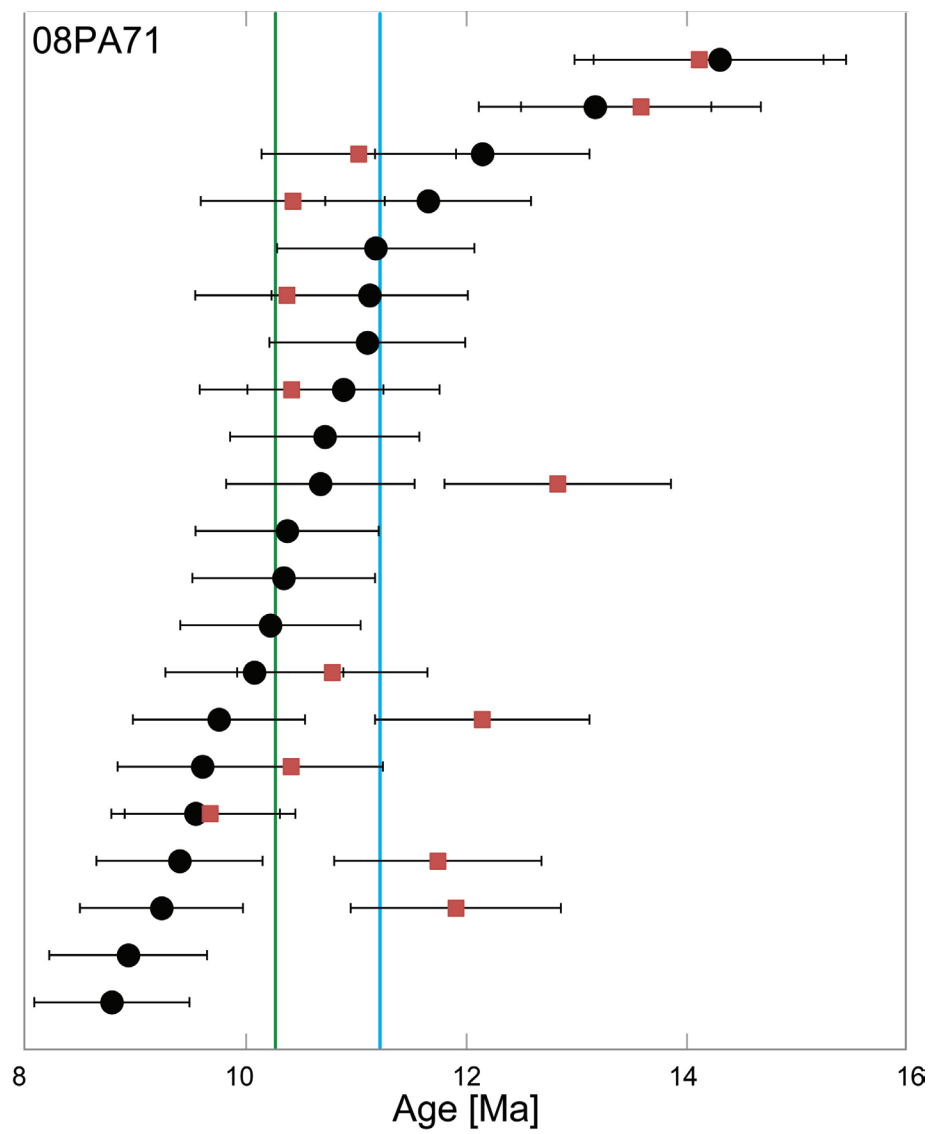
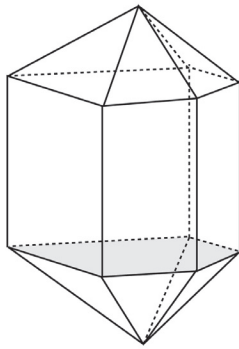
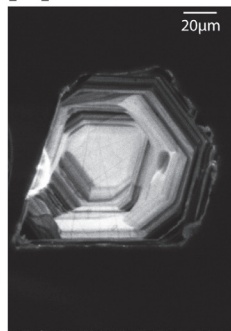
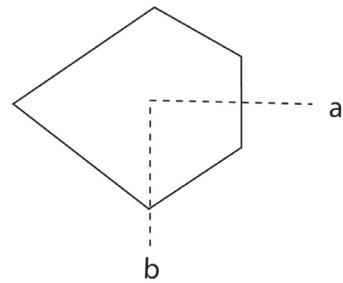


**Figure 15.** Results of the depth-profiled corrections for sample 08PA71. The plot shows the zircon aliquots with a normal alpha-ejection correction (black circles) and if possible, the same aliquot with a unique alpha-ejection correction (red squares). The green line shows the weighted mean age for the normally corrected ages and the blue line shows the weighted mean age for the uniquely corrected ages. The difference between weighted mean ages is about +7%. Note that corrected ages are sometimes older and sometimes younger uncorrected ages, indicating a high degree of heterogeneity among zonation types in the zircons of 08PA71.

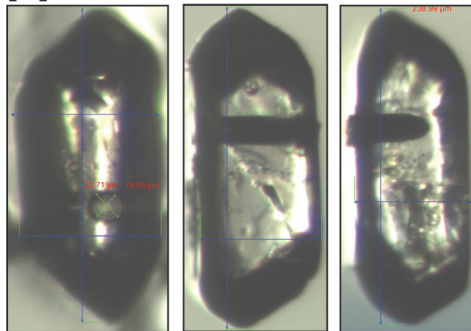
[A]



**Pentagonal Zircon, 08PA01**



[B]



**Oblique Pit Angle, 08PA71**

[C]

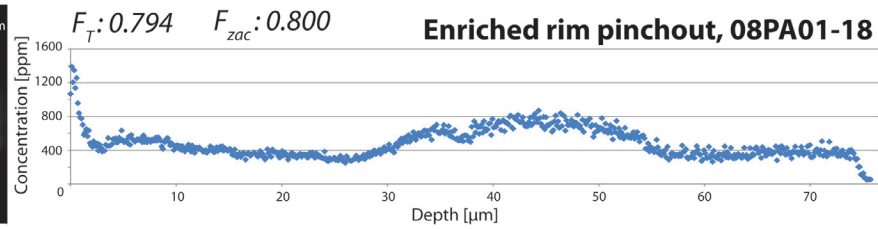
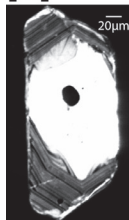


**Figure 16.** Potential complications of the LA-ICP-MS depth profiling technique. [A] Pentagonal-shaped zircon crystal. {010} faces are developed on one side but there is simply a vertex on the other. Odd geometries can influence the alpha-ejection correction, causing an over- or under-estimation of He retentivity. Another complication is related to finding the drill pit in this type of geometry. [B] Oblique angle drill pit. Photos show the drilled face and two parallel faces. The pit appears significantly deeper from one angle than from the other. This could cause a drastic over- or under-estimation of the drill rate, which would result in zone bins that are incorrect and thus an incorrect alpha-ejection correction, as well. [C] An actual depth profile and a representative CL image (image is not the from the same grain as the depth profile). In this case, it appears as if there is a narrow, U-Th enriched rim which does not greatly affect the alpha-ejection correction. However, CL imagery from this sample shows that enriched zones are often thicker at the tips and pinch out at the waist of the zircon. In this case, the alpha-ejection correction will be heavily overestimated, resulting in a “too young” age.

Sample	Age (Ma)	2 $\sigma$ (Ma)	Width1 ( $\mu$ m)	Min. Abrasion ( $\mu$ m)	Max. Abrasion ( $\mu$ m)	U (ppm)	Th (ppm)	<sup>147</sup> Sm (ppm)	[U]e (ppm)	Th/U	He (nmol/g)
z08PA01-9	15.7	1.25	56.53	34.00	67.70	161.8	45.1	0.8	172.2	0.28	14.6
z08PA01-11	12.2	0.98	56.36	34.20	67.90	95.6	27.6	0.7	101.9	0.29	6.7
z08PA01-10	9.8	0.78	42.50	48.00	81.80	205.8	124.0	0.0	234.4	0.60	12.4
z08PA01-31	8.3	0.66	40.83	59.17	86.55	519.53	195.2	0.9	564.5	0.4	25.3
z08PA01-32	8.8	0.70	43.12	56.88	84.26	128.27	52.2	0.7	140.3	0.4	6.7
z08PA01-33	11.5	0.92	52.75	47.25	74.63	297.32	68.3	0.4	313.1	0.2	19.4
z08PA01-34	13.3	1.06	39.91	60.09	87.47	268.92	106.4	0.6	293.4	0.4	21.1
z08PA01-35	8.8	0.71	61.93	38.07	65.45	101.12	30.8	0.4	108.2	0.3	5.2
z08PA01-36	11.7	0.94	50.92	49.08	76.46	165.93	56.0	1.3	178.8	0.3	11.3
z08PA01-37	16.2	1.29	75.23	24.77	52.15	77.49	31.9	0.5	84.8	0.4	7.4
z08PA01-39	15.1	1.21	68.35	31.65	59.03	66.74	29.9	0.6	73.6	0.4	6.0
z08PA01-40	15.0	1.20	86.24	13.76	41.14	123.71	20.1	0.3	128.4	0.2	10.4
z08PA01-41	8.3	0.67	63.30	36.70	64.08	58.42	26.0	0.5	64.4	0.4	2.9
z08PA01-42	9.0	0.72	46.33	53.67	81.05	222.84	93.9	0.6	244.5	0.4	11.8



**Table 1.** Results from mechanical abrasion of zircon from sample 08PA01. Abrasion was performed in two separate batches.

Sample	Age (Ma)	2 $\sigma$ (Ma)	F <sub>T</sub>	Age <sub>corrected</sub> (Ma)	2 $\sigma$ (Ma)	F <sub>znc</sub>	F <sub>T</sub> diff	Age Diff (%)	Drill Rate ( $\mu$ m/sec)	U (ppm)	Th (ppm)	<sup>147</sup> Sm (ppm)	[U]e (ppm)	Th/U	He (nmol/g)	mass ( $\mu$ g)	ESR
z08PA01-13	8.97	0.72	0.641	9.96	0.80	0.604	-0.04	11.08	0.590	416.5	133.3	0.8	447.2	0.32	13.9	2.22	30.84
z08PA01-14	10.05	0.80	0.782	10.42	0.83	0.754	-0.03	3.66	0.688	245.8	66.7	0.8	261.1	0.27	11.1	8.86	53.35
z08PA01-15	8.32	0.67	0.723	9.67	0.77	0.622	-0.10	16.20	0.840	731.2	74.1	0.5	748.3	0.10	24.3	3.66	40.50
z08PA01-16	8.71	0.70	0.738	10.13	0.81	0.634	-0.10	16.33	0.741	700.6	126.0	0.9	729.6	0.18	25.3	5.22	43.34
z08PA01-17	9.16	0.73	0.788	10.02	0.80	0.720	-0.07	9.41	1.005	285.9	61.2	0.4	300.0	0.21	11.7	8.66	54.78
z08PA01-18	10.07	0.81	0.794	10.00	0.80	0.800	0.01	-0.69	0.590	666.5	133.9	0.9	697.3	0.20	30.1	9.59	56.64
z08PA01-19	9.24	0.74	0.787	10.91	0.87	0.666	-0.12	18.12	0.849	472.8	55.0	0.9	485.5	0.12	19.0	8.69	54.01
z08PA01-20	8.20	0.66	0.779	9.07	0.73	0.704	-0.07	10.60	0.796	364.6	90.7	0.9	385.5	0.25	13.3	8.01	52.49
z08PA01-21	10.01	0.80	0.777	11.10	0.89	0.700	-0.08	10.94	0.806	193.1	59.4	0.7	206.8	0.31	8.7	8.04	52.18
z08PA01-22	9.46	0.76	0.801	12.08	0.97	0.627	-0.17	27.76	0.816	163.3	70.4	1.2	179.5	0.43	7.3	11.91	59.58
z08PA01-23	10.50	0.84	0.775	11.04	0.88	0.737	-0.04	5.21	0.826	240.1	109.8	5.6	265.4	0.46	11.7	9.09	52.37
z08PA01-24	8.50	0.68	0.748	10.24	0.82	0.621	-0.13	20.39	0.836	1082.4	152.1	1.7	1117.4	0.14	38.3	5.37	45.10
z08PA01-25	8.82	0.71	0.777	10.32	0.83	0.664	-0.11	17.00	0.846	219.8	59.7	0.7	233.6	0.27	8.6	8.29	52.12
z08PA01-26	9.29	0.74	0.806	10.33	0.83	0.724	-0.08	11.26	0.856	756.5	170.2	1.6	795.7	0.23	32.1	11.43	60.21
<b>Averages:</b>	<b>9.24</b>	<b>0.74</b>	<b>0.77</b>	<b>10.38</b>	<b>0.83</b>	<b>0.68</b>	<b>-0.08</b>	<b>12.66</b>	<b>0.79</b>								
z08PA71-9	9.6	0.77	0.813	10.42	0.83	0.750	-0.06	8.36	0.955	272.3	37.4	0.5	280.9	0.14	11.8	13.01	62.21
z08PA71-10	9.4	0.75	0.792	11.75	0.94	0.634	-0.16	24.91	0.965	217.8	49.4	0.6	229.1	0.23	9.2	9.31	56.02
z08PA71-11	10.9	0.87	0.786	10.43	0.83	0.822	0.04	-4.32	0.869	464.6	64.3	0.7	479.4	0.14	22.2	8.77	54.06
z08PA71-12	10.7	0.86	0.766	12.84	1.03	0.638	-0.13	20.14	0.842	1357.1	97.6	1.9	1379.6	0.07	60.9	6.17	48.76
z08PA71-14	12.2	0.97	0.684	11.04	0.88	0.754	0.07	-9.23	0.989	503.9	106.0	0.2	528.2	0.21	23.7	5.39	35.39
z08PA71-15	11.1	0.89	0.796	10.38	0.83	0.854	0.06	-6.76	0.846	458.8	73.2	1.1	475.6	0.16	22.7	10.43	56.98
z08PA71-16	9.2	0.74	0.786	11.92	0.95	0.610	-0.18	28.89	0.824	304.2	30.2	0.2	311.1	0.10	12.2	9.18	53.80
z08PA71-17	9.8	0.78	0.740	12.16	0.97	0.595	-0.15	24.45	0.864	475.4	104.8	0.8	499.5	0.22	19.5	7.09	44.04
z08PA71-18	14.3	1.14	0.814	14.12	1.13	0.825	0.01	-1.32	0.989	639.4	96.2	0.8	661.5	0.15	41.6	13.41	62.79

Sample	Age (Ma)	2 $\sigma$ (Ma)	F <sub>T</sub>	Age <sub>corrected</sub> (Ma)	2 $\sigma$ (Ma)	F <sub>zac</sub>	F <sub>T</sub> diff	Age Diff (%)	Drill Rate ( $\mu$ m/sec)	U (ppm)	Th (ppm)	<sup>147</sup> Sm (ppm)	[U]e (ppm)	Th/U	He (nmol/g)	mass ( $\mu$ g)	ESR
z08PA71-19	9.6	0.76	0.768	9.69	0.77	0.758	-0.01	1.37	0.893	521.9	38.8	1.6	530.8	0.07	21.0	6.54	49.22
z08PA71-20	11.7	0.93	0.805	10.44	0.83	0.900	0.09	-10.52	0.948	309.8	103.9	0.7	333.7	0.34	16.9	12.96	60.61
z08PA71-21	13.2	1.05	0.798	13.60	1.09	0.774	-0.02	3.16	0.909	773.9	74.0	3.2	791.0	0.10	44.9	10.55	57.30
z08PA71-22	10.1	0.81	0.807	10.79	0.86	0.754	-0.05	7.00	1.269	1255.8	149.9	1.8	1290.3	0.12	56.6	11.02	60.08
<b>Averages:</b>	<b>10.9</b>	<b>0.9</b>	<b>0.8</b>	<b>11.50</b>	<b>0.92</b>	<b>0.74</b>	<b>-0.04</b>	<b>6.62</b>	<b>0.94</b>								

**Table 2.** Results from unique alpha-ejection corrections on zircons from samples 08PA01 and 08PA71.

Sample	Age (Ma)	2 $\sigma$ (Ma)	F <sub>T</sub>	Drill Rate ( $\mu$ m/sec)	Age <sub>corrected</sub> (Ma)	2 $\sigma$ (Ma)	F <sub>T</sub>	Geometry	Grouping	Notes	F <sub>T</sub> diff (%)	Age diff (%)
z08PA01-13	9.0	0.72	0.641	1.670	8.90	0.71	0.646	2D Prism			-0.47	-0.72
							0.649	2D Prism		Broad Tips	-0.77	-1.18
							0.669	2D Pinacoid	2um zones		-2.77	-4.14
							0.657	2D Prism	2um zones		-1.57	-2.39
							0.621	2D Prism			2.03	3.27
							0.605	2D Prism		Broad Tips	3.63	6.00
							0.642	2D Pinacoid	2um zones		-0.07	-0.11
							0.621	2D Prism	2um zones		2.03	3.27
							0.618	3D Pinacoid	2um zones		2.33	3.77
							0.604	3D Prism	2um zones		3.73	6.18

**Table 3.** Results from varying model parameters for sample 08PA01.